Data Analytics Models and Methods for Fault Identification and Prognosis in Mechanical Structures and Manufacturing Processes

Yuhang Liu

A dissertation submitted in partial fulfillment of the requirements for the degree of

Doctor of Philosophy
(Industrial and Systems Engineering)

at the

UNIVERSITY OF WISCONSIN-MADISON
2018

Date of final oral examination: 02/11/2018

Committee Members:

Prof. Shiyu Zhou (Committee Chair, Department of Industrial and Systems Engineering)
Prof. Ananth Krishnamurthy (Department of Industrial and Systems Engineering)
Prof. Jingshan Li (Department of Industrial and Systems Engineering)
Prof. Kaibo Liu (Department of Industrial and Systems Engineering)
Prof. Xiaoping Qian (Department of Mechanical Engineering)

ACKNOWLEDGEMENTS

The research presented in this dissertation benefited from valuable insights and support of many people. It is my pleasure to express my sincere gratitude to all of them.

First and foremost, I would like to thank my PhD advisor, Prof. Shiyu Zhou for his outstanding guidance, mentorship and full support in my PhD studies. Words cannot express my heartfelt gratitude for his efforts towards my development as a good researcher and a future academic mentor. I have been so lucky to benefit from not only his expertise in academic research, but also his great personality in all other aspects.

I would also like to thank my doctoral committee members Prof. Ananth Krishnamurthy, Prof. Jingshan Li, Prof. Xiaoping Qian and Prof. Kaibo Liu for serving on my committee and providing helpful suggestions to improve my dissertation.

I would like to give my sincere gratitude to Prof. Jiong Tang from the University of Connecticut, one main collaborator of my research. Some of my research experiments have been conducted in his laboratory. Without his full support and guidance, my research study would not have been so smooth. I have benefited a lot from his insightful guidance and comments, which helped me a lot in my research.

My thanks also go to my friends in my lab: Devashish Das, Junbo Son, Jianguo Wu, Chao Wang and Raed Kontar. Thank you for being supportive and accompanying me in my PhD studies. You really make my life in Madison enjoyable and memorable.

Lastly and most importantly, I want to thank my parents for their unconditional love, support and encouragement. Without their support, I would not have made this achievement in my life. I am very lucky to have them as my parents, to have their full support on my education and to make them proud.

ABSTRACT

The accurate detection and efficient prognosis of faults in engineering systems are of great practical importance. The systems concerned encompass a broad spectrum of human-made structures and processes, including civil, mechanical and aerospace structures and various manufacturing processes. The precise detection of faults involved in the systems is critical in avoiding structure deterioration, performance degradation, productivity loss and even loss of lives. Prognosis is the ability to predict accurately the future condition of the systems, such as degradation status and remaining useful life. The prognosis helps to carry out the optimal maintenance scheduling for structures and smart operation management of manufacturing processes.

The rapid development of sensor techniques makes it possible for data collection in a quick and accurate manner. Quantitative analysis based on physical model or statistical model applying on the large amount of collected data provide great opportunities for achieving precise fault detection and prognosis. However, significant and fundamental challenges exist in fully exploiting the available data to achieve this goal. For example, the identifiability of a fault based on collected data is essential and should be addressed before any fault identification efforts. Specifically, the commonly used finite element model (FEM) has not been validated for its identifiability in the application of structural damage identification. The induced bias due to linearization is often ignored for damage estimation, which may lead wrong fault identification. Also, efficient methods to predict the progression of structural properties based on finite element models are lacking. Furthermore, various data types require specific data modelling and analysis techniques for fault detection beyond the traditional statistical monitoring methods in manufacturing processes. These issues are being studied in this dissertation.

Specific contributions of this thesis are made in fault identification and prognosis in mechanical structures and manufacturing processes.

In mechanical structures, the identifiability of FEM, the bias reduction by measurements selection and the prognosis of structural property degradation are addressed. In specific:

- A quantitative framework is proposed to address the identifiability of structural damage identification based on finite element models.
- A measurement selection algorithm is proposed for bias reduction in damage estimation.
- A hierarchical Bayesian degradation model is proposed to efficiently estimate the trend of damage growth in structures.

In manufacturing processes, two specific methods are proposed for fault identification of untraditional data type. Specifically,

- Defects with specific spatial patterns on semiconductor wafer are recognized by converting the original pattern recognition problem as point matching problem using Hough Transformation.
- Variations of acoustic attenuation curves are being quantified by linear mixed effect model and permutation tests to provide the guidelines on the quality inspection in nanocomposites manufacturing.

Besides the aforementioned challenges, there are other issues need to be addressed. For example, the integration of piezoelectric transducer circuitry network into mechanical structures enhances the performance of frequency-shift-based damage identification method. However, a quantitative analysis on the tuning variable of the network is lacking of studies. The quantitative study will not only enhance the understanding of such integrated network, but also provide

guidelines on tunings to achieve the optimal fault identification. Also, the location of the integrated network significantly influences the performance of the fault identification. Analysis on the optimal allocation of the transducers leads the most sensitive system response due to the structural damages, in which provides the most accurate fault detection.

TABLE OF CONTENTS

LIST OF FIGURES

LIST OF TABLES

1. Introduction

1.1 Background

Fault management in engineering systems is the integration of fault detection, fault identification and fault prediction. Fault detection monitors the engineering systems to identify the occurrence of faults. The simplest way is to calculate the significance of differences in monitoring signals before and after the damages. Fault identification is to further quantify any existed damages, e.g., type, location and severities. Physical models are often utilized for such tasks. Fault prediction is a natural extension of fault detection and identification. It attempts to forecast system performance by assessing the current condition of the system.

Fault management plays critical roles in both engineering structures and processes. Generally, fault management provides knowledge on conditions of engineering systems for smart decision making. In engineering structures, the early detection of damages ensures the safety of mechanical, aerospace and civil structures, which saves money and even lives. Accurate identification of damages leads precise fault correction for economical purposes. Most types of damage or structural weakness in structures cannot be observed directly and are caused by the changes in structural properties. Revealing such evolving path of structural damage is highly desirable in practice for prognosis and maintenances scheduling. In manufacturing process, the early detection of nonconforming parts or products with low qualities leads early corrective actions to ensure consistent delivery of a quality product and to avoid productivity loss. Forecasting the future conditions of manufacturing process provides guidelines for smart operation managements.

Due to the practical importance of fault management, huge amount of systematical studies has been done over decades. Comprehensive references on different methods for fault management can be found in [1-5]. These methods can be roughly categorized into either pure physical models or pure data-driven methods. Pure physical models describe the dynamics of the engineering systems using differential equations based on physical principles. System properties are quantified by the equations, where types of faults can be easily classified. For examples, analyses of fatigue damage and life prediction in structures are based on physical models in [3]. Paris' law is widely used for crack growth estimation [6,7]. The multistage manufacturing processes is being modeled and diagnosed using state space model [8]. State space model is also adopted for modelling variation propagation of assembly systems in [9]. However, physical models are highly specific and not compatible among different models, and are generally costly in computation. Pure data-driven methods reveal the natures of engineering systems by exploiting the sensing data measured from systems. The rapid development of sensor techniques makes it possible for data collection in a quick and accurate manner. Generic statistical models are applied to make the models applicable to various systems. For instances, a popular category of data driven methods is to model the sensing signal directly using stochastic process or degradation path model [10]. Hidden Markov models (HMM) have been adopted for damage prognosis of a pre-stressed concrete bridge [11] and is used for prediction of gear failures [12]. Root cause diagnosis of process variations is identified using Bayesian network [13]. Compared with physical models, most data-driven methods suffer from lacking support of physical principles, which may result in inaccurate or even misleading interpretation of data. Another drawback of data-driven methods is the inefficient utilization of data. For example, traditional statistical monitoring methods [14-15] are often adopted for monitoring manufacturing processes. Alarms are raised for abnormal changes. However, the

traditional monitoring techniques are not adequate for many data types, such as spatial patterns or functional data. Even if these data can be quantified into the framework of the traditional methods, valuable information contained in the original data (e.g., the pattern or the functional relationship) is missed. In this dissertation, a combined method which takes advantage from both physical model data-driven approach is proposed to fill the gap. Data are interpreted based on fundamental physical laws in statistical manners. Data are fully exploited to provide insight knowledge of the structures and lead better identification and prediction results. Besides, specific data analytics methods are proposed for fault detection in manufacturing processes to fully utilize specific data types. In the following, discussions fall into two categories, fault management in structures and fault detection in manufacturing processes.

1.2 Fault Identification and Prognosis in Structures

In this section, challenges together with proposed solutions are introduced for fault identification and prognosis in structures.

1.2.1 Identifiability issue in fault detection by FEM

Although FEM has made its success in damage identification over decades by formulating the complicated structures into small elements, very limited studies exist on analyzing the identifiability of the FEM used in such applications. Most existing works adopt some types of optimization algorithms to minimize the error function and expect the achieved result is a global optimal solution. However, the optimization procedure cannot always guarantee to converge to the global optimal values and in some cases, even a unique global optimal solution does not exist. Indeed, a non-unique model parametrization of FEM might result in an ill-posed identification problem. For example, if FEM returns the same system response for different damage locations in

a structure, then the damage locations cannot be uniquely identified no matter what method we are using. Thus, the identifiability study, i.e., the investigation of the existence of a one-to-one relation between the input-output behavior of the model and the parameters, is a critically important step before the actual parameter estimation procedure is carried out based on FEM.

To address the identifiability issue in fault detection by FEM, a quantitative framework is adopted. FEM of structures are formulated into a state space model representing linear time invariant (LTI) dynamic system, where the definitions of the identifiability of a dynamic system can be applied to address the problem.

1.2.2 Induced bias in damage estimation due to linearization

Linearization of the eigenvalue problem has been widely used in the damage detection based on the change of natural frequencies. However, the linearization method introduces bias in the estimation of damage parameters. Moreover, the commonly employed regularization method may cause the estimation different from the true underlying solution. These issues cause wrong estimation in the damage severities and even wrong damage locations. Limited work has been done on addressing these issues.

We find that particular combinations of natural frequencies will result in less biased estimation using linearization approach. Thus, a measurement selection algorithm to select an optimal set of natural frequencies for damage identification is proposed. The proposed algorithm adopts L_1- norm regularization with iterative matrix randomization for estimation of damage parameters. The selection is based on the estimated bias using the least square method. Numerical studies are conducted to validate the effectiveness of the method.

1.2.3 Efficient structural damage growth prediction

Both physic-based approach and data-based approach suffer from their inherent weakness in tackling damage prognosis issue in structures. Physical models are generally case specific, which limit their application to broad types of structures. Second, these methods assume that an accurate mathematical model is available and the model requires specific mechanistic knowledge and theories relevant to the systems under consideration. In practice, it is very difficult to build such a good physical model. Furthermore, physics based methods often ignore the uncertainties in the system structure and the measurements. Computational load is general heavy in physical models. Data-driven methods, on the other hand, limits attentions only on explaining data. Stochastic process is able to model the degradation signals well without revealing the change of structural properties. HMM and other state space models require tons of historical data for model training before usage. Also, since degradation status is classified into discrete states as an approximation of the underlying true continuous state, the prognosis in a long term could be unreliable. Thus, a method that integrates both the advantages of physical model and data-driven method is desired.

To fulfill an efficient structural damage growth prediction, a dynamic data-driven hierarchical Bayesian degradation model, which takes advantage of both the physical finite element model and the data driven Bayesian framework, is proposed.

1.3 Fault Detection in manufacturing processes

In this section, two specific data analysis methods are introduced for spatial point pattern and functional data in manufacturing processes, respectively.

1.3.1 Surface Defects in Semiconductor Manufacturing

Defects on semiconductor wafer usually distribute as spatial point patterns, which may contain the information of root cause. Traditional control charts monitor the total number of defects as a criteria of alarm. However, the information of specific spatial patterns is missing. A new method based on Hough transform is proposed, where point pattern detection problem is converted into a simple point matching problem. Thus, specific spatial patterns can be recognized to indicate the existence of defects.

1.3.2 Acoustic Attenuation Curves in Nanocomposite Manufacturing

The variation of ultrasonic attenuation curves are flexible indicators for the quality inspection of A206-Al2O3 Metal Matrix Nanocomposites (MMNCs) by ultrasonic testing. Most control charts are developed for monitoring point values. Even if multivariate control charts are designed for vector data, assumptions often cannot be validated in practice. Thus, new methods on dealing with functional data are desired. The new method is based on linear mixed effect (LME) model and permutation test. LME model is adopted to characterize the variation of ultrasonic attenuation curves. Further, permutation test is employed to classify the quality of samples, where no assumptions of distribution are needed.

1.4 Outline of the Dissertation

The remainder of the dissertation is organized as follows: Chapter 2 addresses the identifiability issue in fault detection by FEM. In this chapter, the detailed quantitative framework is introduced. The analysis of the transfer function in dynamic system is applied to a beam structure. It is theoretically proved that damage severity at a given location in a uniform beam is identifiable. A numerical algorithm is adopted for checking the identifiability issue of multiple damage locations. In Chapter 3, the hierarchical model which integrates the FEM and Bayesian

framework is introduced. The stiffness loss is the target damage progression being analyzed by the proposed model. The trend of the stiffness loss can be efficiently and accurately estimated by Gibbs sampling. Chapter 4 and 5 provides the specific data analysis method for spatial point pattern in semiconductor wafer and acoustic attenuation curves in MMNCs, respectively. In Chapter 4, the original point patter detection problem is converted into point matching problem by using Hough Transformation. Compared with the existing point pattern matching methods, the proposed method does not require training data and is relatively easy to implement and compute. Chapter 5 introduces the linear mixed effect model on quantifying the variation of ultrasonic attenuation curves by ultrasonic testing. Permutation test is further employed for quality inspection. In addition, a microstructure modelling and wave propagation simulation method to simulate ultrasonic attenuation characteristic for A206-Al2O3 MMNCs are proposed to enhance the understanding of the wave-microstructure interaction and also address the difficulty in fabricating nanocomposites of different microstructural features in practice. Chapter 6 summarizes the contributions of this dissertation and discusses the future work.

2. Identifiability Analysis of Finite Element Models for Vibration-Response Based Structural Damage Detection in Elastic Beams*

In this chapter, the identifiability of FEM-based structural damage detection is investigated for undamped elastic beams. We theoretically proved that damage severity at a given location in a uniform beam is identifiable by reformulating the FEM into a linear time invariant (LTI) system. A numerical algorithm is also proposed for checking the identifiability issue of multiple damage locations. Numerical case studies are provided to validate the effectiveness and usefulness of the proposed framework.

2.1 Literature Review

Structural health monitoring and damage detection to assure the structure safety and reliability is an important area in civil, mechanical and aerospace engineering fields. Structural vibration response has been used extensively in structural damage detection. The basic idea is that the occurrence of damage in a structure will lead to changes in its vibration characteristics (e.g., natural frequencies, mode shapes, modal curvatures, etc). By checking such changes we often can infer the location and severity of the damage. Finite element model (FEM) is a broadly used numerical tool in structural analysis to quantitatively check the changes and conduct the inference.

In the literature, many FEM-based damage detection methods have been proposed. Essentially, in these methods, the structure damages have been commonly modeled as element-wise property (e.g., mass density or stiffness) change in the finite element model. The damage severity parameters and damage location parameters are estimated by minimizing an error

*This chapter is based on the paper: **Liu, Yuhang**, Shiyu Zhou, and Jiong Tang. "Identifiability Analysis of Finite Element Models for Vibration Response-Based Structural Damage Detection in Elastic Beams." Journal of Dynamic Systems, Measurement, and Control 138.12 (2016): 121006.

function, which expresses the difference between experimental modal analysis data and the corresponding FEM model prediction. The error functions can be used to measure the changes in natural frequencies, the mode shape, the modal curvatures, or directly the parameters in FEM. It has been shown that the damage estimated based on the FEM are consistent with the experimental results. For example, damage detection methods are developed based on the natural frequency change computed using FEM [16-19]. Methods for model error localization based on the mode shape changes characterized by FEM have been proposed in [20,21]. Natural frequencies and mode shapes are jointly used for damage detection in [22-24]. Pandey, et. al [25] demonstrated that absolute changes in mode shape curvature can be a good indicator of damage for beam FEM structure. Chen and Garba [25,27] presented a method for minimizing the norm of the model property perturbations with a zero modal force error constraint on a truss FEM structure. Sanayei and Onipede [28,29] presented a technique for updating the stiffness parameters of a FEM using the results of a static load-displacement test.

Despite the large amount of works on FEM-based vibration response analysis for structural damage detection, very limited studies exist on analyzing the identifiability of the FEM used in such applications. Most existing works adopt some type of optimization algorithms to minimize the error function and expect the achieved result is a global optimal solution. However, the optimization procedure cannot always guarantee to converge to the global optimal values and in some cases, even a unique global optimal solution does not exist. Indeed, a non-unique model parametrization of FEM might result in an ill-posed identification problem. For example, if FEM returns the same system response for different damage locations in a structure, then the damage locations cannot be uniquely identified no matter what method we are using. Thus, the identifiability study, i.e., the investigation of the existence of a one-to-one relation between the

input-output behavior of the model and the parameters, is a critically important step before the actual parameter estimation procedure is carried out based on FEM.

The uniqueness of the relationship between structural parameters and the system response has been studied analytically for simple beam structures. Chang and Guo [37] prove that the density and the flexural rigidity of the Euler-Bernoulli beam in class C^4 can be uniquely determined from input and output functions. Frederick and Mehmet [38] show that the perturbations in individual modal frequencies are governed uniquely by the intensity of the damage and its location in a fracture structure, where the crack damages are modeled as hinged springs in the model. To our best knowledge, limited work has been done in investigating the identifiability issue in FEM. The most related work is [30]. It is shown that the solution of element properties (e.g., mass and stiffness) to minimize the error function related to the modal force of a truss structure is unique and globally minimal if sufficient modal data are available. However, the uniqueness is interpreted from the view point of optimizing a quadratic error function, not from the relationship between model parameter changes and the model responses. The relation between structural parameters and the system response in FEM is not yet investigated.

In this chapter, we present a quantitative framework to address the identifiability issue in FEM-based structural damage detection. We are trying to answer, whether the element property changes in the FEM based method can be uniquely identified through a given set of input and output measurements. In this study, we use a Euler-Bernoulli beam as the representative structure. The damage at certain location is modeled as a reduction in the stiffness of the element at the corresponding location in the FEM. This way of modeling damage has been commonly used in existing damage detection methods [31-37]. In this framework, FEM of a beam structure is re-formulated into a state space model representing Linear Time Invariant (LTI) dynamic system.

With this formulation, the definitions of the identifiability of a dynamic system [39] can be applied to our problem. Some existed work [40-44] related to the identifiability problem focus on finding sufficient measurements of system input and output such that all system parameters can be identified. However, the focus of this research is the damage parameters (e.g., severities and locations) identifiability based on a given set of measurements. Furthermore, the different mathematical formulation also distinguishes our study from these existed works. By using the properties of an inverse of a block diagonal matrix, we then analyzed the uniqueness of the system transfer function and proved that different severity level of damages at the same location of the structure will result in different system responses. Thus, those damages are theoretically identifiable in the FEM of a beam structure. Further, through checking the changes in structural natural frequencies, we established a sufficient condition for the identifiability of multiple damages at different locations. This sufficient condition can be numerically checked and validated for a given structural FEM. With this checking procedure, we showed that damages at two different locations will only result in the same transfer function under some very restrictive symmetric conditions. In other words, two damages at different locations will be differentiable in most cases. We also conducted several representative case studies to demonstrate the effectiveness and usefulness of the proposed framework of providing a theoretical guideline on the damage identifiability.

The rest of the chapter is organized as follows. In Section 2.2, formulations of FEM into LTI system is presented for a beam structure. The analysis of the relationship between damage at a given location and the structural response function is presented in Section 2.3. The sufficient condition and the numerical checking scheme for multiple damages are discussed in Section 2.4. Numerical case studies are presented in Section 2.5. Conclusions are summarized in Section 2.6.

2.2 Mathematical formulation of damage identifiability in FEM of beam structure

In this section, FEM of a beam structure is formulated into a LTI system and the damage identifiability is investigated under the theoretical framework of dynamic systems. For the sake of clarity, we shall briefly review the representation of a LTI system and the definition of parameter identifiability first.

2.2.1 Review of LTI system and parameter identifiability

Linear time invariant system in state space representation can be expressed as [39, 45]:

$$\frac{\mathrm{d}\mathbf{z}(t)}{\mathrm{dt}} = \mathbf{A}(\boldsymbol{\theta})\mathbf{z}(t) + \mathbf{B}(\boldsymbol{\theta})\mathbf{u}(t)$$

$$\mathbf{y}(t) = \mathbf{C}(\boldsymbol{\theta})\mathbf{z}(t) + \mathbf{D}(\boldsymbol{\theta})\mathbf{u}(t) \tag{2.1}$$

where $\mathbf{z} \in R^n$, $\mathbf{u} \in \mathrm{R}^{\mathrm{r}}$, $\mathbf{y} \in \mathrm{R}^{\mathrm{m}}$ and $\boldsymbol{\theta} \in \mathrm{R}^{\mathrm{q}}$, represent the state (e.g., displacement), the input (e.g., a force vector), the output measurement (e.g., displacement and velocity) and the parameters of the system respectively, and $\mathbf{A}$ is the system matrix, $\mathbf{B}$ is the input matrix, $\mathbf{C}$ is the output matrix and $\mathbf{D}$ is the feed-through matrix with size $\mathbf{A}: R^q \to R^{n\times n}$, $\mathbf{B}: R^q \to R^{n\times r}$, $\mathbf{C}: R^q \to R^{m\times n}$, $\mathbf{D}: R^q \to R^{m\times r}$.

The identifiability problem of a LTI system is that whether the damage parameter $\boldsymbol{\theta}$ can be uniquely estimated based on the input and output of the system. In order to deal with this problem, LTI system is expressed in the frequency domain for a more compact formulation by taking Laplace transformation, which leads to:

$$\mathbf{Y}(\boldsymbol{s}) = \mathbf{H}(\boldsymbol{s})\mathbf{U}(\boldsymbol{s})$$

where $\mathbf{Y}(\boldsymbol{s})$ and $\mathbf{U}(\boldsymbol{s})$ are the output and input in the frequency domain, respectively and $\mathbf{H}(\boldsymbol{s}) = \mathbf{C}(\mathbf{sI} - \mathbf{A})^{-1}\mathbf{B} + \mathbf{D}$ is the transfer function. Note that, if $m = 1$ and $r = 1$, i.e., $\mathbf{C, D}$ are row vectors and $\mathbf{B}$ is column vector, the transfer function is a single function, otherwise, it is a transfer function matrix. In the article, $\mathbf{H}(\boldsymbol{s})$ is used for a transfer function matrix, while $H(\boldsymbol{s})$ is reserved for a single transfer function.

A formal definition of parameter identifiability is given based on the transfer function [39].

Definition Let $(\mathbf{A}, \mathbf{B}, \mathbf{C}, \mathbf{D})(\boldsymbol{\theta})$ be a parametrization of the system matrices $(\mathbf{A}, \mathbf{B}, \mathbf{C}, \mathbf{D})$. This parametrization is said to be *parameter-identifiable* if

$$\mathbf{C}(\boldsymbol{\theta_1})\big(\mathbf{sI} - \mathbf{A}(\boldsymbol{\theta_1})\big)^{-1}\mathbf{B}(\boldsymbol{\theta_1}) + \mathbf{D}(\boldsymbol{\theta_1}) = \mathbf{C}(\boldsymbol{\theta_2})\big(\mathbf{sI} - \mathbf{A}(\boldsymbol{\theta_2})\big)^{-1}\mathbf{B}(\boldsymbol{\theta_2}) + \mathbf{D}(\boldsymbol{\theta_2})$$

for all $\boldsymbol{s} \in \mathbb{C}$, implying $\boldsymbol{\theta_1} = \boldsymbol{\theta_2}$.

The condition in the definition is equivalent to the statement: if $\boldsymbol{\theta_1} \neq \boldsymbol{\theta_2}$, then there exists a $s \in \mathbb{C}$, such that two transfer functions corresponding $\boldsymbol{\theta_1}$ and $\boldsymbol{\theta_2}$, respectively, are different. The parameter identifiability implies a unique relation between the transfer function $\mathbf{H}(s)$ and parameters $\boldsymbol{\theta}$, which provides a way to check the parameter identifiability of LTI system. It should be pointed out that the above definition guarantees the identifiability "in principles". In other words, if a system is deemed non-identifiable based on above definition, then no matter what methods we use, we will not be able to uniquely identify the parameter. On the other hand, if a system is identifiable, then it means in theory, the parameters can be estimated from system inputs and outputs. However, in practice, limited by the measurement system and noise contamination, the identification results may not be satisfactory. Nevertheless, the identifiability analysis provides us important insights to the system and should be conducted before the parameter estimation step.

2.2.2 Formulate FEM of a beam structure into LTI system

In the context of FEM, the vibration behavior of an undamped or lightly damped beam structure can be described by the equation

$$\mathbf{M}\ddot{\mathbf{x}}(t) + \mathbf{K}\mathbf{x}(t) = \mathbf{F}(t) \tag{2.2}$$

where $\mathbf{M} \succ \mathbf{0}$ and $\mathbf{K} \succcurlyeq \mathbf{0}$ are the global mass and stiffness matrices, respectively, $\mathbf{x}$ and $\mathbf{F}$ contain the nodal displacements and nodal forces, respectively. The assumption of undamped or lightly damped system is commonly used in structural analysis for simplicity. However, we would like to point out that the results in the work are also held for the commonly assumed proportional damping system, where the damping matrix $\mathbf{C_d}$ is a linear combination of $\mathbf{M}$ and $\mathbf{K}$.

For a one-dimensional Euler–Bernoulli beam discretized into n elements as shown in Fig.2-1, $\mathbf{x^T} = (d_1, \alpha_1, d_2, \alpha_2, \dots d_{n+1}, \alpha_{n+1})$, where d_i and α_i represent the translational displacement and the bending rotation of the i^{th} node respectively. $\mathbf{M}$ and $\mathbf{K}$ are symmetric block diagonal matrices with size $2(n+1)$ assembled by n element mass matrices $\mathbf{M_i}$ and element stiffness matrices $\mathbf{K_i}$ on the diagonal. A detailed assembling procedure from element wise matrices to global matrices $\mathbf{M}$ and $\mathbf{K}$ can be found in [46].

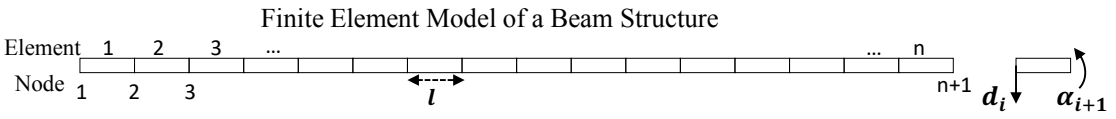

Fig 2-1 An example of finite element representation of a beam structure with n elements and $n+1$ nodes.

The occurrence of damage is assumed to cause the reduction of the stiffness of element. Thus, the global stiffness matrix $\mathbf{K}$ regarding the damages can be represented as $\mathbf{K}(\mathbf{p}, \boldsymbol{\gamma})$, where $\mathbf{p}$ and $\boldsymbol{\gamma}$ are the vectors with the same length representing the damage locations and damage severities in the elements respectively. The components of $\mathbf{p}$ take non-duplicated integer values from 1 to n and the components of $\boldsymbol{\gamma}$ range from 0 to 1. For example, if $\mathbf{p}$ and $\boldsymbol{\gamma}$ take scalar values $\mathbf{p} = p$ and $\boldsymbol{\gamma} = \gamma$, then the p^{th} element stiffness matrix has the form

$$\mathbf{K_p} = \gamma \times EI \begin{bmatrix} \frac{12}{l^3} & \frac{6}{l^2} & -\frac{12}{l^3} & \frac{6}{l^2} \\ & \frac{4}{l} & -\frac{6}{l^2} & \frac{2}{l} \\ & & \frac{12}{l^2} & -\frac{6}{l^2} \\ sym & & & \frac{4}{l} \end{bmatrix}, \gamma \in [0,1]$$

where E and I are the density, Young modulus of elasticity and second moment of inertia respectively.$\gamma = 0$ indicates a complete stiffness loss in the p^{th} element and $\gamma = 1$ indicates no stiffness loss in the element.

Define $\mathbf{z} = (\boldsymbol{x}^T, \dot{\boldsymbol{x}}^T)^T$, then an n-element beam described by Eq.(2.2) can be formulated into LTI system with matrices $\mathbf{A}, \boldsymbol{B}, \boldsymbol{C}$ and $\mathbf{D}$ explicitly expressed as:

$$\mathbf{A} = \begin{bmatrix} \mathbf{A_{11}} & \mathbf{A_{12}} \\ \mathbf{A_{21}} & \mathbf{A_{22}} \end{bmatrix} = \begin{bmatrix} \mathbf{0} & \mathbf{I} \\ -\mathbf{M^{-1}K(p,\gamma)} & \mathbf{0} \end{bmatrix} \tag{2.3a}$$

$$\mathbf{B} = \begin{bmatrix} \mathbf{B_{11}} \\ \mathbf{B_{21}} \end{bmatrix} = \begin{bmatrix} \mathbf{0} \\ \mathbf{M^{-1}E_B} \end{bmatrix} \tag{2.3b}$$

$$\mathbf{C} = [\mathbf{C_{11}}\ \mathbf{C_{12}}] = [\mathbf{E_C}, \mathbf{0^T}] \tag{2.3c}$$

$$\mathbf{D} = \mathbf{0} \tag{2.3d}$$

where $\mathbf{I}$ is the identity matrix with size $2(n+1)$. The undamped vibration leads $\mathbf{A_{22}} = \mathbf{0}$. Without loss of generality, we assume$\mathbf{D} = \mathbf{0}$. $\mathbf{E_B}$ and $\mathbf{E_C}$ are matrices that specify the input and output locations in $\mathbf{x^T} = (d_1, \alpha_1, d_2, \alpha_2, \ldots d_{n+1}, \alpha_{n+1})$. For example, if $\mathbf{E_B} = \mathbf{e_i}$ is a zero column vector of length $2(n+1)$ with its ith component equal to 1, then the input is excited through the ith component of $\mathbf{x}$. Similarly, if $\mathbf{E_C} = \mathbf{e_k^T}$, the output is measured from the kth component of $\mathbf{x}$. If two or more components of $\mathbf{x}$ are excited and measured at the same time, the matrices $\mathbf{E_B}$ and $\mathbf{E_C}$ can be formed accordingly using vector $\mathbf{e}$s. For instance, the translational displacement d and bending rotation α of a single node j are excited or measured simultaneously in most cases. Thus, $\mathbf{E_B} = [\mathbf{e_{2j-1}}; \mathbf{e_{2j}}]$ and $\mathbf{E_C} = \begin{bmatrix} \mathbf{e_{2j-1}^T} \\ \mathbf{e_{2j}^T} \end{bmatrix}$ for a single node j.

The parameters $\boldsymbol{\theta} = (\mathbf{p}, \boldsymbol{\gamma})$ in the LTI system are the damage locations $\mathbf{p}$ and the damage severities $\boldsymbol{\gamma}$. Note that the parameters only appear in the system matrix $\mathbf{A}$. In order to check the parameter identifiability of $\boldsymbol{\theta} = (\mathbf{p}, \boldsymbol{\gamma})$ in FEM by definition, the transfer function of the LTI system can be obtained as $\mathbf{H}(s) = \mathbf{C}\big(\mathbf{sI} - \mathbf{A}(\mathbf{p}, \boldsymbol{\gamma})\big)^{-1}\mathbf{B} = \mathbf{E_c}(-\mathbf{s^2M} + \mathbf{K})^{-1}\mathbf{E_B}$. In most cases, the matrices $\mathbf{E_C}$ and $E_\mathbf{B}$ are just selector matrices that select the components in the matrix $(-\mathbf{s^2M} + \mathbf{K})^{-1}$ that correspond to the input force and the measurement locations. Thus, $\mathbf{H}(s)$ is often either a submatrix of or include multiple components of $(-\mathbf{s^2M} + \mathbf{K})^{-1}$. Based on the definition of identifiability, the parameters $\boldsymbol{\theta} = (\mathbf{p}, \boldsymbol{\gamma})$ are identifiable if the transfer function $\mathbf{H}(s)$

is different for $(\mathbf{p_1}, \boldsymbol{\gamma_1}) \neq (\mathbf{p_2}, \boldsymbol{\gamma_2})$. In the next section, a FEM beam structure is discussed for its parameter identifiability.

2.3 Identifiability of the Severity of Damage at a Given Location

In this section, the damage severity identification is studied for a collocated structure in FEM, where the actuator and the sensor are placed at the same node. The actuator and the sensor are assumed to excite and measure both the translational displacement and bending rotation of the same node, respectively. Thus, the damage severity at a given element is identifiable if the following 2×2 transfer function matrix $\mathbf{H}_j(s)$ is different for different values of damage severity.

$$\mathbf{H}_j(s) = \begin{bmatrix} H_{2j-1,2j-1}(s) & H_{2j-1,2j}(s) \\ H_{2j,2j-1}(s) & H_{2j,2j}(s) \end{bmatrix} \tag{2.4}$$

where $H_{k,l}(s)$ represents the k,lth element of the matrix $(-\mathbf{s^2M + K})^{-1}$**.** In fact, $\mathbf{H}_j(s)$ is the j^{th} block matrix in the main diagonal of $(-\mathbf{s^2M + K})^{-1}$ for this system.

Through the following lemma, we can prove that the damage severity at a given element is identifiable for all collocated sensor and actuator locations in the FEM beam structure.

Lemma $\mathbf{H_j}|(p, \gamma_1) \neq \mathbf{H_j}|(p, \gamma_2)$ if $\gamma_1 \neq \gamma_2$ for $p = 1,2, \ldots n$ and $j = 1,2,, \ldots n+1$, where $\mathbf{H}_j|(p, \gamma_1)$ represents the matrix $\mathbf{H}_j$ given parameters (p, γ_1).

The proof of the lemma utilizes the following property of a block diagonal matrix, which has been studied in literature [47-51].

Define $\mathbf{V}$ as a symmetric block diagonal matrix which is specified as:

$$\mathbf{V}=\begin{bmatrix} \mathbf{R_1} & -\mathbf{Q_2^T} & & & \\ -\mathbf{Q_2} & \mathbf{R_2} & -\mathbf{Q_3^T} & & \\ & \ddots & \ddots & \ddots & \\ & & -\mathbf{Q_n} & \mathbf{R_n} & -\mathbf{Q_{n+1}^T} \\ & & & -\mathbf{Q_{n+1}} & \mathbf{R_{n+1}} \end{bmatrix}$$

where $\mathbf{R}_i$s and $\mathbf{Q}_j$ s are block. Define $\mathbf{\Delta_i}$ and $\mathbf{\Sigma_i}$ by the following recursive relationship:

$$\begin{cases} \mathbf{\Delta_1 = R_1}, \\ \mathbf{\Delta_i = R_i - Q_i \Delta_{i-1}^{-1} Q_i^T}, \end{cases} \qquad \begin{cases} \mathbf{\Sigma_{n+1} = R_{n+1}}, \\ \mathbf{\Sigma_i = R_i - Q_{i+1}^T \Sigma_{i+1}^{-1} Q_{i+1}}. \end{cases} \tag{2.5}$$

Note that, the direction of recursion is forward from $\mathbf{R_1}$ to $\mathbf{R_{n+1}}$ for $\mathbf{\Delta_i}s$, and backwards from $\mathbf{R_{n+1}}$ to $\mathbf{R_1}$ for $\mathbf{\Sigma}_i s$. Define $\mathbf{\Omega_j}$ using $\mathbf{\Delta_i}$ and $\mathbf{\Sigma_i}$ as

$$\begin{cases} \mathbf{\Omega_i = \Delta_i}, & \mathbf{i < j} \\ \mathbf{\Omega_i = \Sigma_i}, & \mathbf{i > j} \\ \mathbf{\Omega_j = \Delta_j + \Sigma_j - R_j} \end{cases}$$

One important property of the inverse of a block diagonal matrix $\mathbf{V}$ is given in [47] as

$$\begin{cases} \mathbf{V_j^{-1} = \Omega_j^{-1}} \\ \mathbf{V_{j-l}^{-1} = \Delta_{j-l}^{-1} Q_{j-l+1}^T \Delta_{j-l+1}^{-1} \cdots \Delta_{j-1}^{-1} Q_j^T \Omega_j^{-1}, l = 1 \ldots j-1} \\ \mathbf{V_{j+l}^{-1} = \Sigma_{j+l}^{-1} Q_{j+l} \Sigma_{j+l-1}^{-1} \cdots \Sigma_{j+1}^{-1} Q_{j+1} \Omega_j^{-1}, l = 1 \ldots n+1-j} \end{cases} \tag{2.6}$$

where j represents the j^{th} block column of the inverse of $\mathbf{V}$. Thus, $\mathbf{V_j^{-1}}$ is the j^{th} block matrix in the main diagonal of $\mathbf{V^{-1}}$.

For a FEM beam model, if we let $\mathbf{V(s)} = (-s^2\mathbf{M} + \mathbf{K(p,\gamma)})$, then $\mathbf{V^{-1}}(s)$ will be the complete system transfer function matrix. Since both $\mathbf{M}$ and $\mathbf{K}$ are symmetric block diagonal matrices, $\mathbf{V(s)}$ is also a symmetric block diagonal matrix. Thus, Eq.(2.6) can be utilized to calculate the transfer function matrix $\mathbf{H}_j(s)$ without directly inverting the entire matrix $\mathbf{V(s)}$.

Moreover, for a uniform beam structure, $\mathbf{R}_i$s and $\mathbf{Q}_j$ s are 2×2 block matrices satisfying the condition $\mathbf{Q_2} = \mathbf{Q_3} = \cdots = \mathbf{Q_{n+1}}$ and $\mathbf{R_2} = \mathbf{R_3} = \cdots = \mathbf{R_n}$, and both $\mathbf{R}_i s$ and $\mathbf{Q}_j s$ are non-singular matrices. The following proposition states one important property of $\mathbf{\Delta_i}$ and $\mathbf{\Sigma_i}$ based on the $\mathbf{R}_i$s and $\mathbf{Q}_j$ s.

Proposition The recursion of matrices $\mathbf{\Delta_i}$ in Eq.(2.5) of a uniform beam under the LTI expressed in Eq.(2.3) follows that $\mathbf{\Delta_i(p, \gamma_1)} = \mathbf{\Delta_i(p, \gamma_2)}$ for $i < p$ and $\mathbf{\Delta_i(p, \gamma_1)} \neq \mathbf{\Delta_i(p, \gamma_2)}$ for $i \geq p$ if $\boldsymbol{\gamma_1} \neq \boldsymbol{\gamma_2}$, where p is the damage location and γ is the damage severity.

A similar result holds for $\mathbf{\Sigma_i}$ in the backward recursion. For a uniform beam, $\mathbf{\Delta_i}$ and $\mathbf{\Sigma_i}$ are positive definite matrices [63,64] in the recursions. A direct calculation shows that $\mathbf{\Delta_i(p, \gamma_1)} = \mathbf{\Delta_i(p, \gamma_2)}$ for $i \geq p$ if and only if $\boldsymbol{\gamma_1} = \gamma_2$ following a general condition of $\mathbf{\Delta_{p-1}} \succ \mathbf{0}$. Based on the proposition, the outline of the proof is summarized as follows. Suppose the damage occurs at the p^{th} element with different damage parameters γ, which will lead to the changes in block matrices $\mathbf{R_p}, \mathbf{R_{p+1}}, \mathbf{Q_{p+1}}$ and $\mathbf{Q_{p+1}^T}$ in $\mathbf{V}$. Suppose the j^{th} node is collocated for excitation and measurement. Then we have the following cases:

(1) For $j > p + 1$, $\mathbf{\Delta_j(\gamma)}$ results in different values for different γs based on the proposition. $\mathbf{\Sigma_j}$ remains the same for different γs, since the backward recursions have not passed the p^{th} element with damage yet. Thus, $\mathbf{\Omega_j} = \mathbf{\Delta_j} + \mathbf{\Sigma_j} - \mathbf{R_j}$ will be different due to $\mathbf{\Delta_j}$. Similar results hold for $j \leq p - 1$ by interchanging $\mathbf{\Delta_j}$ and $\mathbf{\Sigma_j}$.

(2) For $j = p \; or \; p + 1$, the differences in $\mathbf{\Omega_j} = \mathbf{\Delta_j} + \mathbf{\Sigma_j} - \mathbf{R_j}$ come from all three terms and a direct calculation shows that $\mathbf{\Omega_j}$ is different for different γs. The details of the tedious symbolic

calculations are omitted here. As a result, $\mathbf{\Omega_j}$ will be different in all three cases regardless of the collocated position j, and $\mathbf{H}_j = \mathbf{\Omega_j^{-1}}$ will be different, which proves the lemma.

The lemma states that different severities at the same location are identifiable for all collocated sensor and actuator locations. That is, at least one component in the matrix $\mathbf{H}_j$ will differ for different γs. Once the location of damage is known, the system response provides a unique mapping to the damage severity which can be used to monitor the health condition.

2.4 Identifiability of Damage Location

In previous section, the damage severity is shown to be always identifiable at a fixed element for all collocated excitation and measurement locations in FEM. In this section, a more general identifiability problem, i.e., the identifiability of damage location, is investigated. The problem we want to address is that: assume we have a damaged element in the FEM, can we uniquely identify its location? Mathematically, this problem can be formulated as:

Given a FEM based uniform beam under the LTI expressed in Eq.(2.3), will there be two pairs of parameters $(\mathbf{p_1}, \boldsymbol{\gamma_1})$ and $(\mathbf{p_2}, \boldsymbol{\gamma_2})$, such that $\mathbf{H_j}|(\mathbf{p_1}, \boldsymbol{\gamma_1}) = \mathbf{H_j}|(\mathbf{p_2}, \boldsymbol{\gamma_2})$ for some j?

Intuitively, we can guess that for the perfect symmetric situation, i.e., we have the same boundary condition at both ends of a uniform beam, the collocated sensor and excitation input location is in the middle at the beam, and the two elements are symmetric according to the collocated location, we will not be able to distinguish the two elements. Mathematically, this situation can be stated as: for a FEM based uniform beam with the same boundary condition on two ends under the LTI expressed in Eq.(2.3), $\mathbf{H_{n/2}}|(p, \gamma) = \mathbf{H_{n/2}}|(n + 1 - p, \gamma)$ for an even

number of elements n. In Fig.2-2, examples of the same boundary condition and different boundary conditions on two ends of a beam are presented.

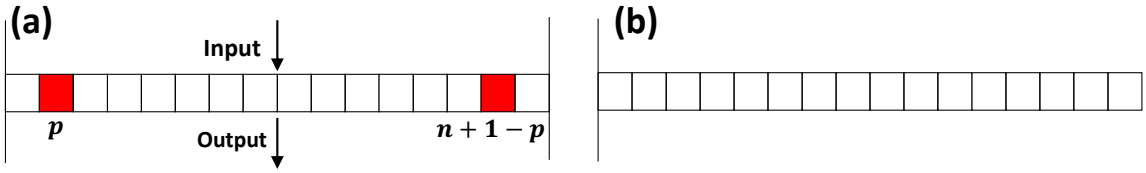

Fig 2-2 Two different experimental beam setups. (a) Fixed-fixed: both ends of the beam are fixed such that the ends can no longer move or rotate. (b) Fixed-free: one end is fixed and the other one is free to move and rotate. In (a), the collocated node for excitation and measurement is at the middle of the beam and the symmetric damage locations are shaded.

Indeed, this intuitive guess can be formally proven to be true utilizing the property of the inverse of block diagonal matrix as shown in Section 2.2.3. If the collocated sensor and excitation location is at the middle of the beam, then the transfer function matrix can be expressed as $\mathbf{H_{n/2}|(p,\gamma)} = \mathbf{\Omega_{n/2}^{-1}} = \left(\mathbf{\Delta_{n/2}(p,\gamma)} + \mathbf{\Sigma_{n/2}} - \mathbf{R_{n/2}}\right)^{-1}$ for a damage at the p^{th} element on the left of the center and $\mathbf{H_{n/2}|(n+1-p,\gamma)} = \mathbf{\Omega_{n/2}^{-1}} = \left(\mathbf{\Delta_{n/2}} + \mathbf{\Sigma_{n/2}(n+1-p,\gamma)} - \mathbf{R_{n/2}}\right)^{-1}$ for a damage at the symmetric $(n+1-p)^{th}$ element on the right of the center. The forward recursion in Eq.(2.5) passes the p^{th} element with damage, so that $\mathbf{\Delta_{n/2}(p,\gamma)}$ is influenced by parameters $\mathbf{(p,\gamma)}$. A similar process holds for $\mathbf{\Sigma_{n/2}(n+1-p,\gamma)}$. Since both ends of the beam have the same boundary condition, $\mathbf{R_1} = \mathbf{R_2} = \cdots = \mathbf{R_{n-1}}$, for all the $n-1$ blocks. Clearly the recursion calculation in Eq.(2.2) of $\mathbf{\Delta_i}$ and $\mathbf{\Sigma_i}$ lead $\mathbf{\Delta_i} = \mathbf{\Sigma_{n-i}}$. Thus, $\mathbf{\Sigma_{n/2}} = \mathbf{\Delta_{n/2}}$ and $\mathbf{\Delta_{n/2}(p,\gamma)} = \mathbf{\Sigma_{n/2}(n+1-p,\gamma)}$, which leads to identical transfer functions and thus proves this intuitive result.

It is easy to track the changes in the recursive functions in Eq.(2.5) for the calculation of the transfer function for symmetric cases. However, if any of the symmetric conditions do not hold, the comparison of recursive functions and hence the analytical transfer function matrix can be messy and untraceable. As a result, the location identifiability cannot be analytically checked in a general setting. To overcome the difficulty, we propose a numerical method to check a sufficient condition of location identifiability for general settings.

The inverse of a large scale block diagonal matrix $(-s^2\mathbf{M} + \mathbf{K}(\mathbf{p}, \boldsymbol{\gamma}))^{-1}$ involving frequency variable s and parameters $(\mathbf{p}, \boldsymbol{\gamma})$ is difficult to be calculated analytically in practice. In order to check the differences of the transfer function for different values of $(\mathbf{p}, \boldsymbol{\gamma})$, we utilize the following property of a scalar transfer function $H(s)$. A transfer function $H(s)$ can be written as

$$H(s) = \frac{c_1}{c_2} \frac{(\lambda - z_1)(\lambda - z_2)(\lambda - z_3) \cdots (\lambda - z_{m-1})(\lambda - z_m)}{(\lambda - \lambda_1)(\lambda - \lambda_2)(\lambda - \lambda_3) \cdots (\lambda - \lambda_{n-1})(\lambda - \lambda_n)}$$

where $\lambda = s^2$, $c_1$and c_2 are constant values, z_is and λ_is are the zeros and poles of the transfer function, respectively. It is known that $c_2 \prod_i (\lambda - \lambda_i) = \det(-\lambda\mathbf{M} + \mathbf{K}(\mathbf{p}, \boldsymbol{\gamma}))$ [52]. Thus, λ_is are also the eigenvalues of the matrix product $\mathbf{M}^{-1}\mathbf{K}(\mathbf{p}, \boldsymbol{\gamma})$ for the generalized eigenvalue problem $\det(-\lambda\mathbf{M} + \mathbf{K}(\mathbf{p}, \boldsymbol{\gamma})) = 0$. Moreover, the natural frequencies f_is of the beam given $\mathbf{M}$ and $\mathbf{K}(\mathbf{p}, \boldsymbol{\gamma})$ are the square roots of λ_is, i.e., $f_i = \sqrt{\lambda_i}$ [52].

Based on the above property, a sufficient condition to check the damage location identifiability is to examine the change of natural frequencies. As long as f_is are different for different $(\mathbf{p}, \boldsymbol{\gamma})$, then the denominators of the transfer functions are different and hence the transfer functions are different. A numerical procedure can be established to check if a FEM beam structure satisfies this sufficient condition or not. The basic idea of the checking is straightforward: we try

to check if multiple elements (more than one) with certain amount of damage will lead to the same set of natural frequencies. If no, then it is sufficient to say that the damage location is identifiable. If yes, then the damage location is not identifiable from the natural frequency point of view. However, we cannot claim it is not identifiable in general because we cannot conclude the transfer functions are the same if only their denominators are the same. Further analysis of other criteria such as the mode shapes can be utilized to fulfill the identifiability checking besides natural frequencies. The rational we use natural frequencies is that natural frequencies depend on the global properties of the system and are easy to be measured in practice while enjoying a higher accuracy compared with mode shapes [53,54]. Define $f_i^{(\mathbf{p},\boldsymbol{\gamma})}$ the i^{th} natural frequency (sorted from smallest to largest) for parameters $(\mathbf{p},\boldsymbol{\gamma})$ and $S_k = \min_{\boldsymbol{\gamma}} \sum_{i\in\mathcal{L}} \left| \frac{f_i^{(\mathbf{p}_*,\boldsymbol{\gamma}_*)} - f_i^{(\mathbf{p_k},\boldsymbol{\gamma})}}{f_i^{(\mathbf{p}_*,\boldsymbol{\gamma}_*)}} \right|$ is the minimum sum of relative frequency difference between the given parameter $(\mathbf{p}_*,\boldsymbol{\gamma}_*)$ and the k^{th} selection of damage locations $\mathbf{p_k}$ by adjusting $\boldsymbol{\gamma}$. $\mathcal{L}$ is the set of the index of natural frequencies being used in the calculation. For example, if only the first five natural frequencies are used, $\mathcal{L} = \{1,2,3,4,5\}$. Further define $S_k^{(j)}$ is the j^{th} smallest value among all $S_k s$. The numerical algorithm for scalar valued p and γ is presented in Table 2-1 for an n-element FEM based beam structure with global mass matrix **M** and stiffness matrix **K**.

Table 2-1. Numerical Algorithm of Location Identifiability of Scalar Valued p and γ

1 Input (p_*,γ_*), and update $\mathbf{K}(p_*,\gamma_*)$,
2 Compute $f_i^{(p_*,\gamma_*)}$, by taking the square root the eigenvalues of $\mathbf{M^{-1}K}(p_*,\gamma_*)$,
3 Define the set $\mathcal{L}$ and a threshold t
4 **For** $k = 1{:}n$
$p_k = k$ and compute S_k
End
5 Sort S_k in the ascending order as $S_k^{(j)}$, i.e., $S^{(1)} \le S^{(2)} \le \cdots \le S^{(n)}$
6 If $S^{(2)} - S^{(1)} > t$, claim the parameter (p_*,γ_*) is identifiable,
otherwise (p_*,γ_*) is not identifiable in the sense of natural frequency.

We'd like to mention that: First, the calculation of eigenvalues of matrices product is important in the algorithm. In this research, a beam structure is utilized as an example for identifiability issue in FEM. Any classical eigenvalue solver [55-58] provides accurate and stable results. For a complicated structure which requires high degree of freedom, there exists many efficient and accurate methods for such computation [59-62]. Second, step 6 is critical to examine the identifiability of parameters (p_*, γ_*). The (p_*, γ_*) is said to be identifiable if and only if the difference between $S^{(2)}$ and $S^{(1)}$ is greater than the threshold t. Note that, $S_{p_*}^{(1)} = 0$ should be the smallest S_k for $k = p_*$ theoretically. The set $\mathcal{L}$ can either be the full set, i.e., $\mathcal{L} = \{1 \text{ to } 2n + 1\}$ or some selected natural frequencies. In practice, only a few natural frequencies can be measured. The threshold t is chosen based on the noise level and the range of the measured natural frequencies. Intuitively, a large t should be assigned for a high noise level, which will reduce the ability of identifying the parameters (p_*, γ_*). For a fixed threshold t, the identifiability increases if a large range of natural frequencies are measured. Also note, the proposed algorithm is capable for both uniform and non-uniform beams.

For multiple damage locations, i.e., $\mathbf{p}_*$ and $\boldsymbol{\gamma}_*$ are vectors, the algorithm is extended by modifying its step 4. For example, if $\mathbf{p}_*$ has two components, a search of all combinations for two damage locations leads a modified step 4 as:

---

4 **For** $k = 1{:}\,\mathrm{C}_2^n$
  $\mathbf{p}_k =$ non-repeated combination of two locations, and compute S_k
End

---

where $\mathrm{C}_2^n = \frac{n!}{2!(n-2)!}$ is the binomial coefficient expressing the total number of non-repeated combination of any two locations from 1 to n.

Note that, step 4 searches all possible locations in order to uniquely identify $\boldsymbol{p}_*$ in a complete space. However, in practice, based on the engineering experience of experts, only limited candidate places can cause the similar changes in observations due to damages, such that, the work load to examine all possible locations can be reduced.

2.5 Numerical case studies

In this section, numerical examples are presented to illustrate the identifiability analysis procedure. The uniform beam used in the simulation has $E = 2.1 \times 10^8$ kPa, $L = 2.54$m, $I = 3.47 \times 10^{-8}$ m^4, $A = 6.45 \times 10^{-4}$ m^2 and $\rho = 0.013$ kg s^2/m. The non-uniform beam case is also studied in this section. The non-uniform beam assumes to have an increasing EI values from $0.5EI$ to $1.5EI$ across the 60 elements, while other parameters are the same as the uniform beam. Two different experimental setups are considered, fixed-fixed beam (Fig 2-2a) and fixed-free beam (Fig 2-2b). Total 60 elements are used in the finite element model to approximate the beam structure. The comparisons of the first three modes (natural frequencies) between analytical results and finite element model of non-damaged beam for both setups are presented in Table 2-2. The comparisons show a good agreement between the analytical model and finite element model. To further reduce the error, the increasing of the number of elements will lead a convergence to the true natural frequencies. However, as a tradeoff, this will incur a high computational cost. In our experience, the number of elements in the order of hundreds promises good results for a structure with simple geometry (e.g., the beam structure).

Table 2-2. Comparisons of the first three modes between analytical results and finite element model of the non-damaged uniform beam in different setups. Units are in circular frequencies.

	Fixed-fixed Beam			Fixed-free Beam		
	Mode1	Mode2	Mode3	Mode1	Mode2	Mode3
Analytical	131.0599	360.9997	707.9573	20.5951	128.7195	360.9997
FEM	130.9033	360.8279	707.3383	20.5717	128.9180	360.9615
Error%	0.12	0.05	0.09	0.11	-0.15	0.01

2.5.1 Damage severity identifiability at a given location

Based on the property of the transfer function $H(s)$ described in Section 2.4, as long as the eigenvalues of the matrix product $\mathbf{M^{-1}K}(p,\gamma)$ for a fixed location p are different for various γs, the transfer function $H(s)$ is severity identifiable.

We investigate the change of natural frequencies f_is (square root of eigenvalues) as a function γ for a fixed location $p = 23$ in Fig 2-3 for two different beam setups. The curves in the plots represent different normalized natural frequencies, i.e. $f_i(\gamma)/\max\big(f_i(\gamma)\big)$. The horizontal axis is the values of γ ranging from 0.1 to 1. Each natural frequency is observed as a monotonic increasing function of γ in both setups for uniform and non-uniform beams. One critical feature is that the natural frequencies increase as a function γ. This observation is consistent with the experimental results reported in [65-69]. The damage of the structure will lead the downward shifting of all natural frequencies.

This feature can be explained by the eigenvalue perturbation analysis. The generalized eigenvalue problem of the beam structure is governed by the relation:

$$(\mathbf{K} - \lambda_i \mathbf{M})\boldsymbol{\phi}_i = 0$$

where $\lambda_i = s_i^2$ is the i^{th} eigenvalue and $\boldsymbol{\phi}_\mathbf{i}$ is the corresponding eigenvector. The eigenvalues λ_i can be solved by an iterative method in solving the minimization problem of a Rayleigh quotient

[70]. However, the trend of change in eigenvalues is not directly obtained. Instead, a simple derivation through perturbation analysis reveals the insight of the changes. Small changes $\mathbf{\Delta K}$ (due to stiffness loss) in $\mathbf{K}$ produce small changes in λ_i and $\boldsymbol{\phi}_i$, for this perturbed system, we have:

$$[(\mathbf{K}+\mathbf{\Delta K})-(\lambda_i+\Delta\lambda_i)\mathbf{M}](\boldsymbol{\phi}_\mathbf{i}+\mathbf{\Delta}\boldsymbol{\phi}_\mathbf{i})=0$$

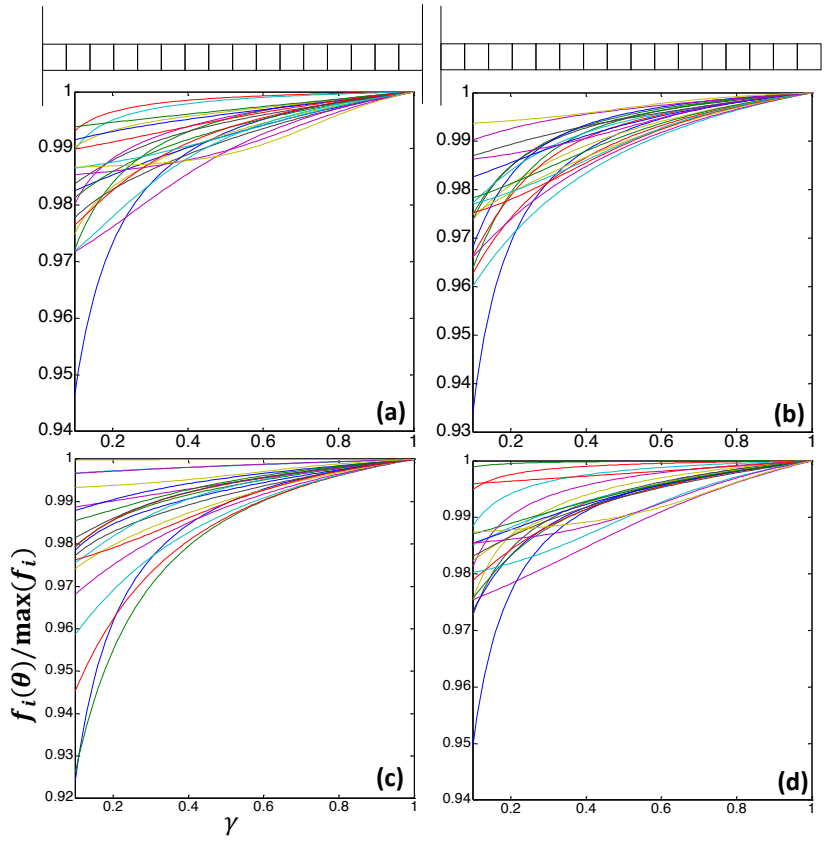

Fig 2-3 Normalized natural frequencies computed from matrix product $\mathbf{M^{-1}K}(p,\gamma)$ for a fixed location $p=23$ vs damage parameter γ in two different beam setups. (a) fixed-fixed uniform beam, (b) fixed-free uniform beam, (c) fixed-fixed non-uniform beam, (d) fixed-free non-uniform beam.

by expanding this equation and neglecting second-order terms [71], we have:

$$\Delta\lambda_i=\frac{\boldsymbol{\phi}_\mathbf{i}^\mathbf{T}\mathbf{\Delta K}\boldsymbol{\phi}_\mathbf{i}}{\boldsymbol{\phi}_\mathbf{i}^\mathbf{T}\mathbf{M}\boldsymbol{\phi}_\mathbf{i}}=(\gamma-1)EI\times\frac{\boldsymbol{\phi}_\mathbf{i}^\mathbf{T}\mathbf{G}\boldsymbol{\phi}_\mathbf{i}}{\boldsymbol{\phi}_\mathbf{i}^\mathbf{T}\mathbf{M}\boldsymbol{\phi}_\mathbf{i}}$$

where **G** is a zero matrix except the pth block matrix in the main diagonal has structure

$$\mathbf{G}_p = \begin{bmatrix} \frac{12}{l^3} & \frac{6}{l^2} & -\frac{12}{l^3} & \frac{6}{l^2} \\ & \frac{4}{l} & -\frac{6}{l^2} & \frac{2}{l} \\ & & \frac{12}{l^2} & -\frac{6}{l^2} \\ sym & & & \frac{4}{l} \end{bmatrix} \succcurlyeq 0$$

which is a positive semidefinite matrix. Since the global mass matrix **M** is a positive definite matrix and $\gamma \in [0,1]$, $\Delta\lambda_i$ is always non-positive, i.e. $\Delta\lambda_i \leq 0$, which means the eigenvalues will not increase for the existence of damage. Several notes from the eigenvalue perturbation analysis are:

1) The change of natural frequencies Δf_i is also non-increasing, since $f_i = \sqrt{\lambda_i}$.
2) In practice, the term $\boldsymbol{\phi}_\mathbf{i}^\mathbf{T}\mathbf{G}\boldsymbol{\phi}_\mathbf{i}$ rarely goes to zero, which leads a decrease in all eigenvalues.
3) The derivation is for a non-damaged beam with stiffness matrix **K**. A similar derivation for a damaged beam $\mathbf{K}(p, \gamma_1)$ has a similar result. Assume a further stiffness loss at element p with $\gamma_2 < \gamma_1$, the change of eigenvalues will be $\Delta\lambda_i = (\gamma_2 - \gamma_1)EI \times \frac{\boldsymbol{\phi}_\mathbf{i}^\mathbf{T}\mathbf{G}\boldsymbol{\phi}_\mathbf{i}}{\boldsymbol{\phi}_\mathbf{i}^\mathbf{T}\mathbf{M}\boldsymbol{\phi}_\mathbf{i}} < 0$ in practice. From this analysis, all eigenvalues will decrease as long as γ is decreasing for a fixed location p, which is consistent with the observation in Fig 2-3.

2.5.2 Location identifiability

The location identifiability is based on the difference between $S^{(2)}$ and $S^{(1)}$. The ability to uniquely identify $(\boldsymbol{p}^*, \boldsymbol{\gamma}^*)$ increases for a large difference. The following two examples validate the effectiveness of the proposed numerical checking algorithm.

In the first example, a single element with damage is considered. The natural frequencies $f_i^{(p_*,\gamma_*)}$ are calculated for the beam with $(p_*, \gamma_*) = (23,0.4)$. The uniform beam is used for the illustration. In Fig 2-4, the horizontal axis is the location parameter p and the vertical axis is S_k obtained at each corresponding location. $S_{p_*}^{(1)} = 0$ in this noise-free situation. Thus, the difference $S^{(2)} - S^{(1)} = S^{(2)}$. Three different $\mathcal{L}$s are used in the calculation of S_k. (1) $\mathcal{L} = \{1\}$, only the smallest natural frequency is used, (2) $\mathcal{L} = \{1,2,3,4,5\}$, the first five natural frequencies are used, and (3) $\mathcal{L} = \{1 \text{ to the } 2n + 1\}$, all the natural frequencies are used.

Due to the symmetry in the fixed-fixed beam setup, $S_{38} = S_{p_*} = 0$ in all three cases. It means $(p_*, \gamma_*) = (23,0.4)$ can not be uniquely identified only based on the natural frequencies $f_i^{(p_*,\gamma_*)}$ in the symmetric beam setup. In other words, parameters (p_*, γ_*) can only be identified in pairs in the perfect symmetric situation. For case (1) in the fixed-fixed setup, since many locations (besides $p = 38$) have $S_k < 0.002$, the (p_*, γ_*) is not location identifiable if the threshold t takes value larger than 0.002 For case (2) in the fixed-fixed setup, since more natural frequencies are utilized, $S^{(2)} = 0.013$. For case (3), the value of $S^{(2)}$ takes value up to 0.4, when all natural frequencies are used, which makes (p_*, γ_*) easier to be identified. Similar results can be obtained for the fixed-free beam setup, except that $S_{38} \neq S_{p_*} = 0$, which leads a unique location identification of (p_*, γ_*) once $S^{(2)} > t$.

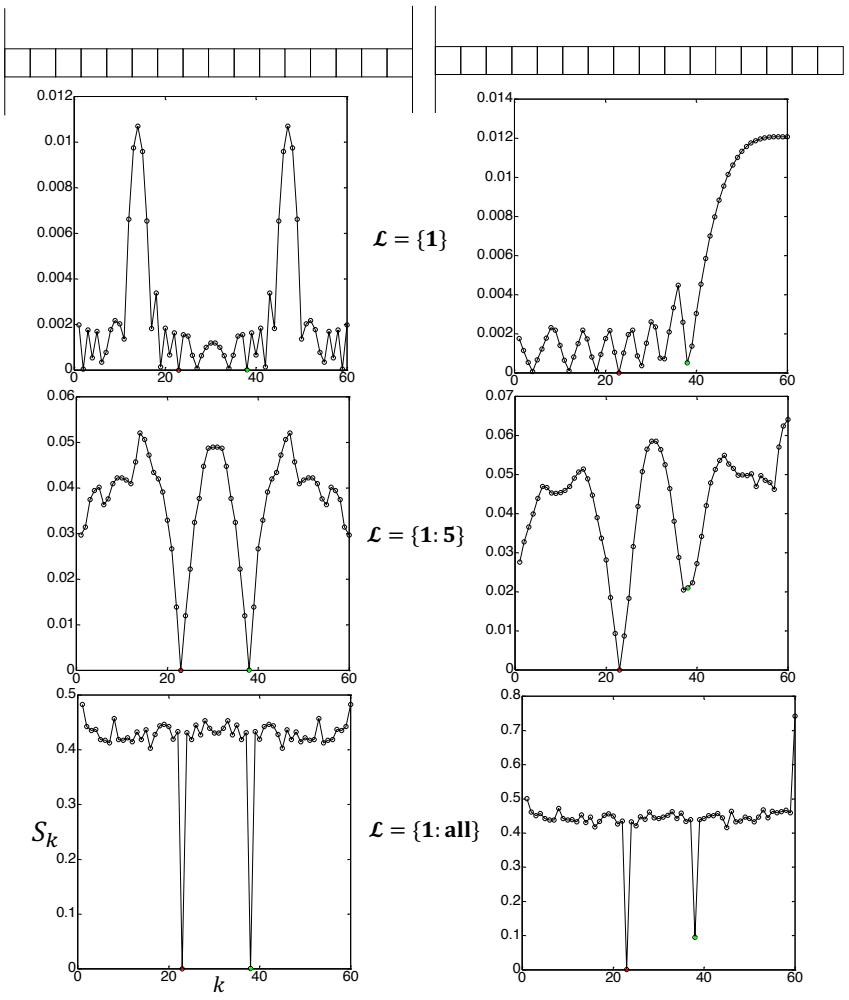

Fig 2-4 The plot S_k as a function of damage locations in different boundary conditions of a uniform beam. Three different $\mathcal{L}$s are used in the calculation of S_k.

Similarly, the plot S_k of a non-uniform beam is presented in Fig.2-5. Note that, since the beam has various EI values across the elements, the perfect symmetric situation does not hold. Thus, the plot S_k in the fixed-fixed beam setup is not symmetric.

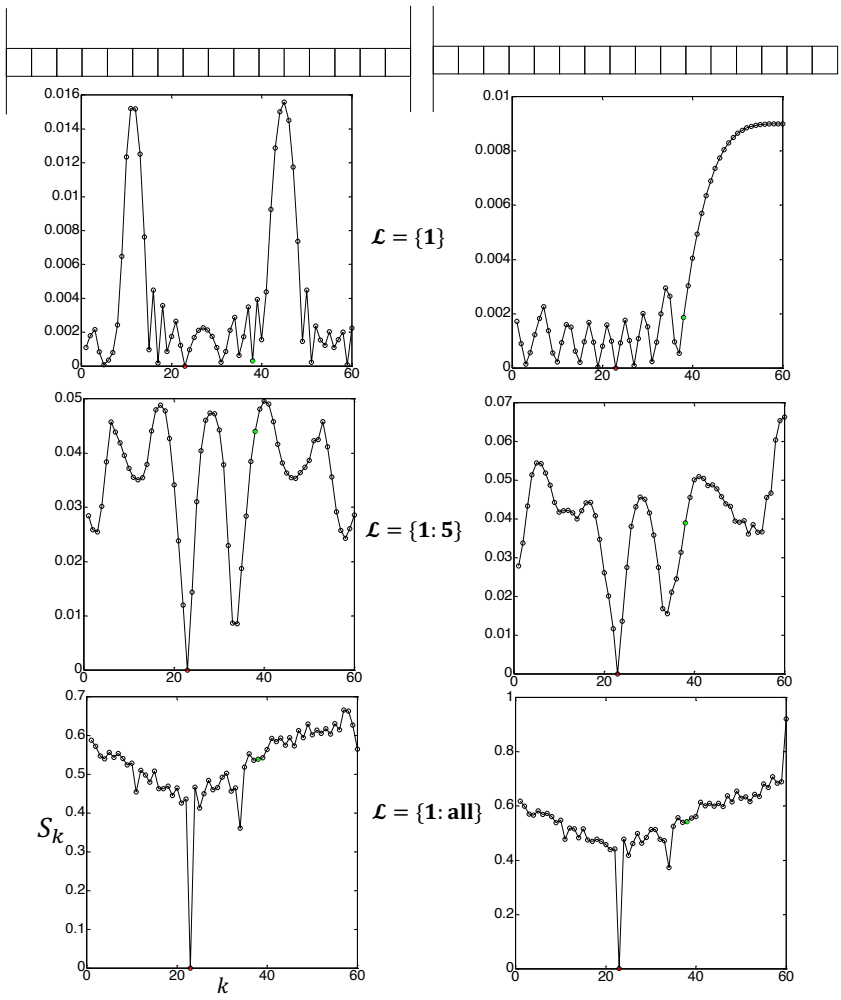

Fig 2-5 The plot S_k as a function of damage locations in different boundary conditions of a non-uniform beam. Three different $\mathcal{L}$s are used in the calculation of S_k.

In the second example, two elements with damages are considered. The natural frequencies $f_i^{(p_*,\gamma_*)}$ are calculated for the beam with $\boldsymbol{p}_* = (7,23), \boldsymbol{\gamma}_* = (0.1,0.4)$. The plots of $S_{k_2|k_1}$ for uniform and non-uniform beam are presented in Figure 2-6 and Figure 2-7, respectively. $S_{k_2|k_1}$ is the minimum sum of relative frequency difference by adjusting the second element location k_2 for a fixed damage location k_1. For example, if $k_1 = 7$, then $S_{k_2|k_1} = 0$ for $k_2 = 23$. Similarly, if $k_1 = 23$, then $S_{k_2|k_1} = 0$ for $k_2 = 7$. In other words, in the plot $S_{k_2|k_1}$ as a function k_1, $S_{k_2|k_1}$ takes value 0 exactly at $k_1 = 7$ and $k_1 = 23$. In the symmetric case of a uniform beam, two additional

locations have $S_{k_2|k_1} = 0$, 1) $k_1 = 54$ which is the symmetry of $k_1 = 7$, 2) $k_1 = 38$ which is the symmetry of $k_1 = 23$. The phenomenon has been shown in Figure 2-7, in which four locations reach 0 in the fixed-fixed beam. As a result, $\boldsymbol{p}_* = (7,23)$ can not be uniquely identified due to its symmetric pair $\boldsymbol{p} = (54,38)$.

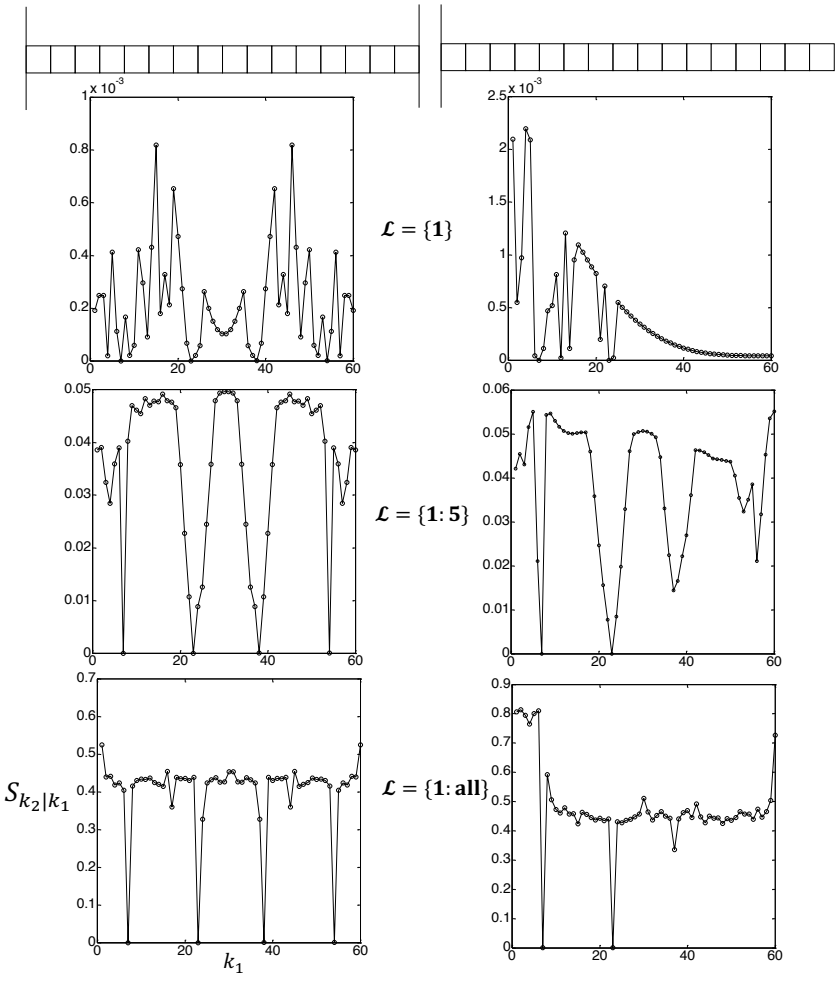

Fig 2-6 The plot $S_{k_2|k_1}$ as a function of damage location k_1 in different boundary conditions of a uniform beam. Three different $\mathcal{L}$s are used in the calculation of S_k.

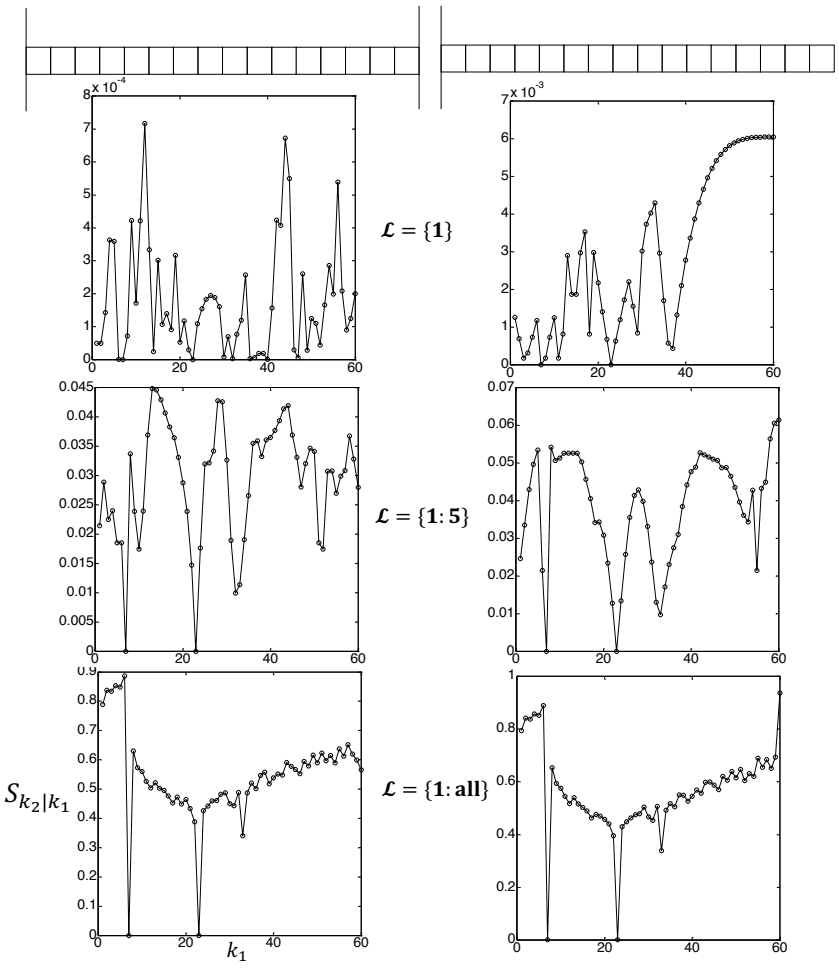

Fig 2-7 The plot $S_{k_2|k_1}$ as a function of damage location k_1 in different boundary conditions of a non-uniform beam. Three different $\mathcal{L}$s are used in the calculation of S_k.

From the above numerical studies, the ability to uniquely identify the damage location (or in pairs in the fixed-fixed uniform beam setup) enhances when the number of nature frequencies in the calculation of S_k increases. Even if only a small range of natural frequencies can be measured in practice, the use of the first five smallest natural frequencies can lead an easy location identifiability due to a large $S^{(2)}$.

2.6 Conclusion

In this chapter, a quantitative framework to address the identifiability issue in FEM-based beam structure is presented. FEM of a beam structure is re-formulated into a state space model representing LTI dynamic system in Eq.(2.3). By using the properties of an inverse of a block diagonal matrix, the uniqueness of the system transfer function is proven for different severity level of damages at the same location. That is, the damages are theoretically identifiable in the FEM for a given damage location of a beam structure. Moreover, a sufficient condition for the identifiability of multiple damages at different locations is established based on the natural frequencies. A numerical algorithm is proposed to numerically check and validate the location identifiability of scalar valued damage location. With this checking procedure, we showed that damages at two different locations will only result in the same transfer function under the symmetric conditions. In other words, two damages at different locations will be differentiable in most cases. The algorithm can be extended for vector valued damage. Several representative case studies are conducted to demonstrate the effectiveness and usefulness of the proposed framework for providing a theoretical guideline on the damage identifiability by using FEM-based vibration analysis.

3. Measurements Selection for Bias Reduction in Structural Damage Identification*

In this chapter, we propose a measurement selection algorithm to select an optimal set of natural frequencies for damage identification. The proposed algorithm adopts L_1- norm regularization with iterative matrix randomization for estimation of damage parameters. The selection is based on the estimated bias using the least square method. Numerical studies are conducted to validate the effectiveness of the method.

3.1 Introduction

The timely and accurate identification of damage conditions in structures using real-time, online sensor measurements plays a critical role in ensuring the secure and sustainable operations of various structural systems in aerospace, marine, transportation and infrastructure, and energy and power industries. Among different structural damage identification techniques, the vibration-based methods [175] have been widely used. The basic idea of vibration-based methods is that the structural properties (e.g., mass, stiffness, etc.) will change due to damages in structures and such changes will result in the vibration properties including natural frequencies [176], mode shapes [177] and their variants such as curvature [178], flexibility [179]. Typically, natural frequencies can be measured directly with high accuracy and thus are broadly used in practice [180].

In natural frequencies based damage detection methods, damages are identified by solving the eigenvalue problem with linear approximation [181]. The linearization provides the simplicity and efficiency in the problem solving process. With the linearization, the unknown damage parameters $\Delta\boldsymbol{\alpha}$ can be estimated by the linear equation $\Delta\boldsymbol{\lambda} = \mathbf{S}\Delta\boldsymbol{\alpha}$, where $\mathbf{S}$ is the first order sensitivity matrix

*This chapter is based on the paper: **Liu, Yuhang**, Shiyu Zhou, Yong Chen and Jiong Tang. " Measurements Selection for Bias Reduction in Structural Damage Identification." Journal of Dynamic Systems, Measurement, and Control (to be submitted)

and $\Delta\boldsymbol{\lambda}$ is the measured difference of the eigenvalues between healthy and damaged structures. In practice, the linear equation provides the foundation for damage identification. Based on the finite element model of the structure, the sensitivity matrix $\mathbf{S}$ and the baseline natural frequencies of the structure can be obtained. Then with the real measurement of the natural frequencies and comparing it with the baseline natural frequencies, we can obtain $\Delta\boldsymbol{\lambda}$. And finally, we can solve for $\Delta\boldsymbol{\alpha}$ from the linear relationship.

However, there are generally two major challenges in damage identification based on the linearized relationship between $\Delta\boldsymbol{\lambda}$ and $\Delta\boldsymbol{\alpha}$. First, $\mathbf{S}$ is usually a "fat" matrix, i.e., the number of possible damaged elements are much larger than the number of available natural frequencies, i.e., the number of columns of $\mathbf{S}$ is much larger than the number of rows. Thus, the linear system is a highly underdetermined system. Second, the linear relationship is just an approximation of the true underlying relationship between $\Delta\boldsymbol{\lambda}$ and $\Delta\boldsymbol{\alpha}$. Thus, there will be bias in the solution obtained based on the linear relationship.

In the literatures, research works are available trying to address these two challenges in structural damage identification. To relieve the impact caused by the system underdetermination, one approach is to enlarge the number of the measurements in the system. Typically, natural frequencies are only guaranteed to be measured accurately for the low order ones due to the limitation of sensors. Thus, the number of available natural frequencies are often enlarged through physical modification of structures. For examples, a mass addition technique is explored in [176] to enrich the modal measurements. In this approach, the known masses are added to the structure and thus new modal data is achieved. Similar ideas on adding mass or stiffness to extract additional natural frequencies can be found in [177]. One disadvantage of this type of physical modification is the difficulty to implement in practice due to many physical restrictions. Another type of

physical modification adopts piezoelectric transducers integration onto the structure. The integrated structure is an electro-mechanical system with tunable piezoelectric circuits. The tunable inductance can introduce additional natural frequencies. Examples on such type of electro-mechanical system can be found in [178]. The limitation of physical modification approach is that the number of unknown possible damage elements are often still much larger than the available number of measurements even with physical modification.

Another approach addressing the underdetermination issue is to work with the underdetermined system and try to obtain a sparse solution. The rationale of this strategy is that structural faults typically occur only at a limited number of locations simultaneously. In [182], the authors propose a pre-screening strategy to address the underdetermination issue. The fault locations are ranked according to the likelihoods and the locations with small likelihoods are discarded in order to reduce the fault parameter space. There are two limitations of such approach. The first is the underlying assumption of the distribution in the likelihood function. The independent and identically distributed (i.i.d.) assumption of errors is not generally true in the structural damages. The simplification of the error terms may lead the ranking results unreliable. Also, the cut-off threshold in the ranking procedure is ad hoc and may vary in different systems. Another technique in obtaining the sparse solution is by regularization. In regularization, the L_1 norm of the solution is often added to the objective function as a penalty and it often returns solution with sparsity, i.e., estimates most of the unknown variables to be 0. L_1 regularization is the most commonly used penalty method in the structural damage identification. For example, the authors apply the L_1 norm on the number of the damage locations in [175]. The results are sparse with the true damage locations are recovered. However, it is found that applying L_1 regularization directly often cannot guarantee the solution quality in the sense of solution uniqueness and

consistency. Moreover, the bias induced by the linear approximation may further reduce the accuracy of damage estimation.

In the literature, discussions on the bias in damage estimation caused by the linearization error is limited. The linearization between the structural parameters and the system response is introduced in [183]. The higher order terms in the Taylor's expansion are ignored to achieve the simplification in the equation. The latter research and application follow the similar routine for fault identification in various structural systems. However, there are no thorough discussions on how to address the bias issue, where such bias may lead to large errors in damage identification. In available studies, adding nonlinear higher order terms has been proposed to reduce the impact of bias in the analysis [178]. It should be pointed out that such approach is not recommended in general due to the loss of the linear property in the equation, where we will have serious issue with the resulting underdetermined nonlinear system. Also, the improvements in the solution quality may not be worth the loss of the simplicity and the efficiency in the solution process. In recent studies of structural damage identification, applying deep neural network (DNN) to the problem becomes a new trend [184]. DNN generates reasonable results with high quality training data and well designed network structures, e.g., the choice of activation functions and the layer of the network. It is expected that the bias can be reduced by applying multiple layers of linear functions. However, the DNN is a black box approach and may be ad hoc when selecting the network structure.

From the above review, we can see that the underdetermination issue and the identification bias issue are addressed separately in the existing literature. In this work, we propose a systematic scheme that can reduce the bias in damage identification through a measurement selection method. We find that particular combinations of available natural frequencies can significantly reduce the

estimation bias compared with using all available ones. The proposed algorithm contains three sub-algorithms. In the first algorithm, L_1- norm regularization is adopted with iterative random matrix multiplication and majority voting. The idea of matrix randomization is to multiply random Gaussian matrix to the linear system to achieve 1) matching of correlation structures of error terms and 2) unique solution of L_1 minimization. The majority voting process helps to estimate the damage severities from multiple iterations. In the second algorithm, the estimated damage locations are updated by removing locations with negligible damage severities. The estimated errors of natural frequencies are derived based on the estimated damage parameters, and are further adopted for natural frequency selection by a least squares method in the third algorithm. There are several advantages of the proposed the algorithm. First, the regular L_1- norm regularization is modified to enhance the quality of damage estimation for measurement selection. Second, since the algorithm requires no additional physical modification (e.g., added mass or integrated piezoelectric circuits) of the structures, it can be used in many practical scenarios. It is worth mentioning that the proposed algorithm can also be extended for natural frequencies selection in the physical modified structures for better damage estimation. Third, the proposed algorithm is easy to implement without deriving high order terms in the approximation. Thus, it is computationally friendly for practical uses.

The rest of the chapter is organized as follows. Section 3.2 introduces the linear approximation of the eigenvalue problem. Section 3.3 introduces the L_1- norm regularization with iterative random matrix multiplication and majority voting. Section 3.4 introduces the proposed algorithm for bias reduction through measurement selection. Section 3.5 presents the numerical study to validate the proposed method. Section 3.6 further discusses the factors that influence the performance of the algorithm.

3.2 Problem Formulation

For the sake of clarity, we shall first introduce the linear approximation of the eigenvalue problem in the damage identification. Without the loss of generality, in this research, we are concerned with the structural damages that induces the change of structural stiffness [185]. Also, it is assumed that only a very small number of damages occur in the structure simultaneously to meet the most of damage scenarios in practice.

The dynamics of an un-damped structural system can be described by the linear equation

$$\mathbf{M}\ddot{\mathbf{x}}(t) + \mathbf{K}\mathbf{x}(t) = \mathbf{F}(t) \tag{3.1}$$

where **M** and **K** are the global mass and stiffness matrices, respectively, **x** and **F** contain the nodal displacements and nodal forces, respectively. The eigenvalue problems associated with the healthy structure and damaged structure are in Eq. (3.2) and (3.3), respectively:

$$(\mathbf{K} - \lambda_i \mathbf{M})\boldsymbol{\phi}_i = 0 \tag{3.2}$$

$$\left(\mathbf{K}^d - \lambda_i^d \mathbf{M}\right)\boldsymbol{\phi}_i^d = 0, \tag{3.3}$$

where λ_i and $\boldsymbol{\phi}_i$ are the ith eigenvalue (squared of the ith natural frequency) and eigenvector of the healthy structure, and λ_i^d and $\boldsymbol{\phi}_i^d$ are the ith eigenvalue and eigenvector of the damaged structure, respectively. The damages are only induced by the loss of stiffness, so the mass matrix **M** is the same for both structures. The stiffness matrix $\mathbf{K}^d$ of the damaged structure can be expressed as the increment $\Delta\mathbf{K}$ from **K** in the healthy structure:

$$\mathbf{K}^d = \mathbf{K} + \Delta\mathbf{K} \tag{3.4}$$

Similarly, the change in eigenvalues and eigenvectors can be expressed as:

$$\lambda_i^d = \lambda_i + \Delta\lambda_i \tag{3.5}$$

$$\boldsymbol{\phi}_i^d = \boldsymbol{\phi}_i + \Delta\boldsymbol{\phi}_i \tag{3.6}$$

Substituting Eq. (3.4)-(3.6) in to Eq. (3.3) and neglecting the high order terms, the first order (linear) approximation of the mapping from stiffness to natural frequencies is:

$$\Delta\lambda_i \approx \frac{\boldsymbol{\phi}_i^T \Delta\mathbf{K} \boldsymbol{\phi}_i}{\boldsymbol{\phi}_i^T \mathbf{M} \boldsymbol{\phi}_i} \tag{3.7}$$

In most cases, the eigenvectors are mass normalized, thus, $\boldsymbol{\phi}_i^T \mathbf{M} \boldsymbol{\phi}_i = 1$.

The increment $\Delta\mathbf{K}$ is expressed as the summation of elemental stiffness matrix change:

$$\Delta\mathbf{K} = \sum_{j=1}^{n} \Delta\alpha_j \, \mathbf{K}_j^{(\mathrm{e})}, \tag{3.8}$$

where $\mathbf{K}_j^{(\mathrm{e})}$ is the jth elemental stiffness matrix, and $\Delta\alpha_j$ is the damage parameter ranging in $[-1, 0]$ indicating the percentage change of stiffness of the jth element, where zero means no stiffness loss and -1 means the complete stiffness loss at the element, respectively. n is the number of elements in the finite element model.

Combining Eq. (3.7) and (3.8), the matrix formulation of the linear approximation can be expressed as:

$$\Delta\boldsymbol{\lambda} \approx \mathbf{S}\Delta\boldsymbol{\alpha} \tag{3.9}$$

where $\Delta\boldsymbol{\lambda} = [\Delta\lambda_1, \Delta\lambda_2, \ldots \Delta\lambda_m]^T$ is the set of eigenvalue difference between the damaged structure and the healthy structure. The number m indicates the number of available natural frequencies in the measurement. $\Delta\boldsymbol{\alpha} = [\Delta\alpha_1, \Delta\alpha_2, \ldots \Delta\alpha_n]^T$ is the set of n damage parameters. $\mathbf{S}$ is the sensitivity matrix representing the sensitivity of eigenvalues to the changes in stiffness loss. The components in $\mathbf{S}$ are:

$$\mathbf{S}(i,j) = \frac{\boldsymbol{\phi}_i^T \mathbf{K}_j^{(\mathrm{e})} \boldsymbol{\phi}_i}{\boldsymbol{\phi}_i^T \mathbf{M} \boldsymbol{\phi}_i}$$

In general, the number of columns, n, is much larger than the number of rows, m, i.e., $n \gg m$.

In practice, Eq. (3.9) provides the foundation for damage identification. However, as mentioned in the introduction section, there are two major challenges in damage identification based on (3.9). First, $\mathbf{S}$ is a "fat" matrix so that Eq. (3.9) is an underdetermined system. Second, Eq. (3.9) is just a linear approximation of the true underlying relationship

$$\Delta\boldsymbol{\lambda} = \mathbf{S}\Delta\boldsymbol{\alpha} + \mathbf{e}(\Delta\boldsymbol{\alpha}) \tag{3.10}$$

where $\mathbf{e}(\Delta\boldsymbol{\alpha})$ is the error in the linearization. Please note that $\mathbf{e}$ is generally a function of the current structural damage. As a result, there will be bias in the solution obtained using Eq. (3.9). We propose two techniques to addresses these challenges, which are described in Section 3.3 and 3.4, respectively.

3.3 L_1 Penalty with Iterative Random Matrix Multiplication and Majority Voting Process

We follow the common idea in the literature to address the underdetermined system, i.e., apply a penalty of L_1 norm of $\Delta\boldsymbol{\alpha}$ to the solution. Instead of directly solving Eq. (3.9), we focus on the following optimization problem:

$$\min\|\Delta\boldsymbol{\lambda} - \mathbf{S}\Delta\boldsymbol{\alpha}\|_2 + \beta\|\Delta\boldsymbol{\alpha}\|_1 \tag{3.11}$$

where β is the regularization parameter controlling the weight of the penalty. In practice, Eq. (3.11) is often solved by the following equivalent expression [12]:

$$\min\|\Delta\boldsymbol{\alpha}\|_1, \text{s.t.} \|\Delta\boldsymbol{\lambda} - \mathbf{S}\Delta\boldsymbol{\alpha}\|_2 \leq \epsilon \tag{3.12}$$

where ϵ indicates the error tolerance and plays the equivalent role of β.

There are many algorithms to solve the optimization problem in Eq. (3.12) efficiently. However, solutions to Eq. (3.12) may not be unique [188] or sparse enough [189] to recover the true non-zero damage locations. The uniqueness of the solution to Eq. (3.12) is of critical

importance for damage identification. By the findings in [188], there is either a unique or infinite many solutions to Eq. (3.12). Unfortunately, the uniqueness is not guaranteed when $n > m$, which will lead to unreliable estimation of the damages. In other words, even if adding L_1 penalty results in sparse solution, the solution may be still "abundant" compared to the underlying truth. In practice, an iterative reweighed L_1 minimization algorithm [189] is often adopted to enhance the sparsity. For reader's convenience, we quote the algorithm from [189] in Table 3A-1 in the appendix. There are several remarks of the algorithm: (1) Instead of minimizing Eq. (3.12), the algorithm adopts the weighted objective function**.** The hope is by properly adjusting the weights, the algorithm can recover the underlying sparsity correctly. And (2) The weights are updated iteratively in step 3. The update equation can adopt different forms as discussed in [189]. The general idea of this algorithm is to increase the weights for variables estimated with small absolute values in order to push these variables to be 0 in future iterations. In this paper, we adopt the similar scheme of this idea but with different approaches as described in Algorithms 1 and 2 below.

Instead of Eq. (3.12), we solve the following problem iteratively in our proposed algorithm:

$$\min\|\Delta\boldsymbol{\alpha}\|_1, \text{s.t.} \left\|\widetilde{\Delta\boldsymbol{\lambda}} - \tilde{\mathbf{S}}\Delta\boldsymbol{\alpha}\right\|_2 \leq \epsilon \tag{3.13}$$

where $\widetilde{\Delta\boldsymbol{\lambda}} = \boldsymbol{\Phi}\,\Delta\boldsymbol{\lambda}$ and $\tilde{\mathbf{S}} = \boldsymbol{\Phi}\mathbf{S}$ and $\boldsymbol{\Phi}$ is an $m \times m$ random matrix, whose components are independent and identically distributed samples from a Gaussian distribution. There are two benefits in solving (3.13) instead of solving (3.12) directly.

(1) The correlated structure of the error terms in the linear relationship is addressed.

It is known that the optimization problems in Eq. (3.12) and Eq. (3.11) are equivalent. If we ignore the penalty term in Eq. (3.11), then the objective function of Eq. (3.11) is identical to the objective function for a regular least squares problem. In other words, if we ignore the penalty term in Eq.

(3.11), then the solution to (3.11) will be the regular least squares solution. One important assumption on regular least squares method is that the error term in the model is homogeneous, i.e., the covariance of the term $\mathbf{e}$ is a diagonal matrix and the diagonal elements are the same. This is certainly an unrealistic assumption because the term $\mathbf{e}(\Delta\boldsymbol{\alpha})$ includes both measurement error and the systematical error in the linear approximation. It is known that regular least squares method will lead to systematic bias in the solution for a system with heterogeneous errors [187]. In the proposed algorithm, the objective function Eq. (3.13) ignoring the penalty term is equivalent to $\left(\widetilde{\Delta\boldsymbol{\lambda}} - \tilde{\mathbf{S}}\Delta\boldsymbol{\alpha}\right)^{\mathbf{T}}\left(\widetilde{\Delta\boldsymbol{\lambda}} - \tilde{\mathbf{S}}\Delta\boldsymbol{\alpha}\right)=(\boldsymbol{\Delta\lambda} - \mathbf{S}\Delta\boldsymbol{\alpha})^{\mathbf{T}}(\boldsymbol{\Phi}^{\mathbf{T}}\boldsymbol{\Phi})(\boldsymbol{\Delta\lambda} - \mathbf{S}\Delta\boldsymbol{\alpha})$, which is in the form of the objective function of a generalized least square (GLS) problem [190] assuming the covariance matrix of $\mathbf{e}$ is $(\boldsymbol{\Phi}^{\mathbf{T}}\boldsymbol{\Phi})^{-\mathbf{1}}$. GLS is an effective way to adjust the solution of linear systems to reduce the bias when we have heterogeneous errors. In practice, $(\boldsymbol{\Phi}^{\mathbf{T}}\boldsymbol{\Phi})^{-\mathbf{1}}$ will not be exactly the true covariance of $\mathbf{e}$ and further, the solution of Eq. (3.13) is not obtained through GLS method, but rather through the optimization with the penalty term. However, the above intuitive understanding can provide some justification on the proposed algorithm, i.e., iteratively solving Eq. (3.13) with different random matrices $\boldsymbol{\Phi}$s followed by the majority voting process. The underlying intuition is that when $(\boldsymbol{\Phi}^{\mathbf{T}}\boldsymbol{\Phi})^{-\mathbf{1}}$ is close to the true covariance structure of the error term, then the solution of Eq. (13) will be consistent and close to the true underlying value. On the other hand, when $(\boldsymbol{\Phi}^{\mathbf{T}}\boldsymbol{\Phi})^{-\mathbf{1}}$ is far from the true covariance structure of the error term, the solution will be scattered around. As a result, if we repeatedly try different $\boldsymbol{\Phi}$s, then the solutions that are close to the true underlying value will stand out in the followed majority voting process. Indeed, similar idea has been reported in the literature when solving a sparse system [175].

(2) The uniqueness of the solution can be largely improved.

For $n > m$, the uniqueness of Eq. (3.12) is not guaranteed unless several non-trivial conditions are satisfied [14]. However, it is found that if $\mathbf{S}$ has entries drawn from a continuous probability, the solution to Eq. (3.12) has very high probability to be unique regardless of n and m [188]. $\tilde{\mathbf{S}}$ in Eq. (3.13) is close to a random matrix with Gaussian entries, such that Eq. (3.13) is more likely to generate the unique solution compared to Eq. (3.12). Through multiple iterations, the unique solution will likely stand out as the majority solution in the multiple voting process.

Note that, the reweighed L_1 minimization algorithm in Table 3A-1 still applies the standard L_2 norm, and thus the solution to the reweighed L_1 minimization may be less reliable due to the heterogeneous errors. We summarize the ideas of iterative random matrix multiplication and the majority voting procedure in Algorithm 1 in Table 3-1. The iterative random matrix multiplication step returns an estimated matrix $\left[\widetilde{\Delta\boldsymbol{\alpha}}\right]_{n\times L}$, whose column (i.e., $\widetilde{\Delta\boldsymbol{\alpha}}_{.,l}$) is the estimated damage under each random matrix $\boldsymbol{\Phi}_l$. The row of $\left[\widetilde{\Delta\boldsymbol{\alpha}}\right]_{n\times L}$ (i.e., $\widetilde{\Delta\boldsymbol{\alpha}}_{i,.}$) records the estimations for each element through L iterations. Based on our experiences, a L of several hundreds is sufficient to achieve good results while balancing the computational time.

In the majority voting step, $P\left(\widetilde{\Delta\boldsymbol{\alpha}}_{i,.} \geq -0.05\right)$ is the probability that the estimated damage of the ith element is no less than -0.05 (i.e., a light damage). The "if" condition states that if 95% of the estimated damage severity $\widetilde{\Delta\alpha}_{i,l}$ is larger than -0.05 among L iterations, the ith element is treated as a healthy element and is then set to be 0 (i.e., $\widehat{\Delta\alpha}_i = 0$). In practice, only the stiffness loss larger than 5% (i.e., $\Delta\alpha_i < -0.05$) is treated as damage [177]. The threshold 95% is the confidence to reject the hypothesis that the element has stiffness loss larger than 5% at level 0.05, which is a commonly used criterion in practices [191]. Damaged elements have the majority of

$\widetilde{\Delta\boldsymbol{\alpha}}_{i,.}$ significantly differ from 0 and the distribution of $\widetilde{\Delta\boldsymbol{\alpha}}_{i,.}$ often forms a unimodal shape. The mean value of all iterations are used as the estimation of damage severity.

Table 3-1. Algorithm 1: Iterative Random Matrix Multiplication and Majority Voting

Iterative Random Matrix Multiplication

For $l = 1,2,\dots,L$

Generate random matrix $\boldsymbol{\Phi}_l$ and compute $\widetilde{\Delta\boldsymbol{\lambda}} = \boldsymbol{\Phi}_l\Delta\boldsymbol{\lambda}$ and $\tilde{\mathbf{S}} = \boldsymbol{\Phi}_l\mathbf{S}$

Solve Eq. (13) and record the estimation $\widetilde{\Delta\boldsymbol{\alpha}}_{.,l} = \left[\widetilde{\Delta\alpha}_{1,l}, \widetilde{\Delta\alpha}_{2,l}, \dots \widetilde{\Delta\alpha}_{n,l}\right]^T$

End

Majority Voting

Define $\widetilde{\Delta\boldsymbol{\alpha}}_{i,.} = \left[\widetilde{\Delta\alpha}_{i,1}, \widetilde{\Delta\alpha}_{i,2}, \dots \widetilde{\Delta\alpha}_{i,L}\right]$ and $\widehat{\Delta\boldsymbol{\alpha}} = [\widehat{\Delta\alpha}_1, \widehat{\Delta\alpha}_2, \dots, \widehat{\Delta\alpha}_n]$

For $i = 1,2,\dots,n$

if $P\left(\widetilde{\Delta\boldsymbol{\alpha}}_{i,.} \geq -0.05\right) \geq 95\%$

$\widehat{\Delta\alpha}_i = 0$

else

$\widehat{\Delta\alpha}_i = \text{mean}(\widetilde{\Delta\boldsymbol{\alpha}}_{i,.})$

end

End

Return $\widehat{\Delta\boldsymbol{\alpha}}$ and the locations $\mathbf{L}(\widehat{\Delta\boldsymbol{\alpha}})$ for $\widehat{\Delta\alpha}_i = 0$

Besides the estimation $\widehat{\Delta\boldsymbol{\alpha}}$, Algorithm 1 also returns the locations of zero elements in $\widehat{\Delta\boldsymbol{\alpha}}$, represented by $\mathbf{L}(\widehat{\Delta\boldsymbol{\alpha}})$. In order to recover the damage locations accurately, an iterative procedure is proposed as Algorithm 2 in Table 3-2.

Table 3-2. Algorithm 2: Damage Location Identification Algorithm

1. Set the iteration count $q = 0$, $\mathbf{L}^{(q)} = \mathbf{L}\left(\widehat{\Delta\boldsymbol{\alpha}}^{(q)}\right)$ and $\mathbf{L}^{(\mathbf{0})} = \phi$
2. Run Algorithm 1with constrains $\Delta\alpha_{\mathbf{L}^{(q)}} = \mathbf{0}$ in Eq. (13), return $\widehat{\Delta\boldsymbol{\alpha}}^{(q+1)}$
3. Update the sparsity
$$\mathbf{L}^{(q+1)} = \mathbf{L}\left(\widehat{\Delta\boldsymbol{\alpha}}^{(q+1)}\right)$$
4. Terminate if $\mathbf{L}^{(q+1)} = \mathbf{L}^{(q)}$ or q attains the maximum number. Otherwise, increment q and go to step 2.
5. Return $\widehat{\Delta\boldsymbol{\alpha}}$ and $\mathbf{L}\left(\widehat{\Delta\boldsymbol{\alpha}}\right)$ from the last iteration

In most cases, it takes $q = 2$ or 3 to terminate the algorithm. The $\widehat{\Delta\boldsymbol{\alpha}}$ of the last iteration is used as the final estimation of the damage parameters with the sparsity shown in $\mathbf{L}\left(\widehat{\Delta\boldsymbol{\alpha}}\right)$**.** We name such

estimation $\widehat{\Delta\boldsymbol{\alpha}}$ as L_1-IMR (iteratively matrix randomization). In general, the L_1-IMR estimation achieves better solution quality compared with the pure L_1 regularization by Eq. (12). We use the L_1-IMR estimation for natural frequency selection in the next section.

It is interesting to compare Algorithm 2 with the reweighed L_1 minimization algorithm in Table 3A-1 in the appendix to see the analogy. In fact, by adding constrains $\Delta\alpha_{\mathbf{L}^{(q)}} = \mathbf{0}$ in Eq. (3.13) when run Algorithm 1 is equivalent to have the weight update equation in the reweighed L_1 minimization algorithm as:

$$w_i^{(q+1)} = \begin{cases} 1, & \widehat{\Delta\alpha}_i^{(q)} \neq 0 \\ \infty, & \widehat{\Delta\alpha}_i^{(q)} = 0 \end{cases}$$

In this updating step, all zero valued elements will retain as 0 in the following iterations, while all non-zero valued elements will be estimated with equal weight of 1. The condition $w_i^{(q+1)} = \infty$, for $\widehat{\Delta\alpha}_i^{(q)} = 0$ is equivalent to set $\delta = 0$ in the original weight update equation in Table 3A-1. The key difference between Algorithm 2 and the reweighed L_1 minimization algorithm is in step 2. Instead of solving the L_1 minimization problem once, Algorithm 1 solve the problem multiple times with different random matrices. The benefits of such approach are discussed above.

3.4 Measurement Selection for Bias Reduction

Even if Algorithms 1 and 2 enhance the solution quality for damage identification, the bias introduced by the linear approximation in Eq. (3.9) is not addressed. We find that some subsets of available natural frequencies can return less biased estimation compared with that using all available natural frequencies. Thus, a natural frequencies selection is desired to reduce the bias in the damage estimation.

Mathematically, we want to find a subgroup of natural frequencies that minimize the following L_2- norm

$$d^{(k)} = \left\| \widehat{\Delta\boldsymbol{\alpha}}^{(k)} - \Delta\boldsymbol{\alpha}^{\text{truth}} \right\|_2 \tag{3.14}$$

where $\Delta\boldsymbol{\alpha}^{\text{truth}}$ is the underlying truth of the damage and $\widehat{\Delta\boldsymbol{\alpha}}^{(k)}$ is the damage estimation based on the kth combination of selected natural frequencies by solving $\min\|\Delta\boldsymbol{\alpha}\|_1, \text{s.t.} \left\|\Delta\boldsymbol{\lambda}^{(\mathbf{k})} - \mathbf{S}^{(\mathbf{k})}\Delta\boldsymbol{\alpha}\right\|_2 \leq \epsilon$. $\Delta\boldsymbol{\lambda}^{(k)}$ and $\mathbf{S}^{(k)}$ are the eigenvalue difference and sensitivity matrix corresponding to the kth combination of selected natural frequencies, respectively. In other words, $\Delta\boldsymbol{\lambda}^{(k)}$ and $\mathbf{S}^{(k)}$ are the sub-vector and sub-matrix of $\Delta\boldsymbol{\lambda}$ and $\mathbf{S}$ by retaining the rows corresponding to the kth combination of selected natural frequencies. For example, if $\mathbf{S}$ has dimension 7×20 (i.e., 7 measurements and 20 elements), the submatrix $\mathbf{S}^{(k)}$ may have less rows but the same number of columns, say 4×20. Please note for m available natural frequencies, there are total $2^m - 1$ different combinations.

The challenges in this problem are from the following aspects. First, the underlying truth $\Delta\boldsymbol{\alpha}^{\text{truth}}$ is unknown. Thus, Eq. (3.14) cannot be used directly for bias comparison. Second, since the sensitivity matrix $\mathbf{S}$ is obtained from the linear approximation, the following optimization problems are not equivalent,

$$\arg_k \min\left\|\Delta\boldsymbol{\lambda}^{(k)} - \mathbf{S}^{(k)}\Delta\boldsymbol{\alpha}\right\|_2 \nLeftrightarrow \arg_k \min\left\|\widehat{\Delta\boldsymbol{\alpha}}^{(k)} - \Delta\boldsymbol{\alpha}^{\text{truth}}\right\|_2$$

A reasonable approach is to derive an estimation of the incomputable quantity $d^{(k)}$. Such estimation is named as $b^{(k)}$ and derived as follows.

First note, the eigenvalue difference $\Delta\boldsymbol{\lambda}$ can be expressed with the underlying damages $\Delta\boldsymbol{\alpha}^{\text{truth}}$ and the error term $\mathbf{e}$:

$$\Delta\boldsymbol{\lambda} = \mathbf{S}\Delta\boldsymbol{\alpha}^{\text{truth}} + \mathbf{e} \tag{3.15}$$

Similarly, the eigenvalue difference for the kth combination is:

$$\Delta\boldsymbol{\lambda}^{(k)} = \mathbf{S}^{(k)}\Delta\boldsymbol{\alpha}^{\text{truth}} + \mathbf{e}^{(k)} \tag{3.16}$$

where $\mathbf{e}^{(k)}$ measures the error in the eigenvalue difference corresponding to the kth combination. Please note Eq. (3.15) and (3.16) are exact without approximations.

Intuitively, if $\mathbf{e}^{(k)} \to \mathbf{0}$, solving $\Delta\boldsymbol{\lambda}^{(k)} = \mathbf{S}^{(k)}\Delta\boldsymbol{\alpha}$ returns the unbiased estimation of $\Delta\boldsymbol{\alpha}^{\text{truth}}$**.** Thus, it is reasonable to select the natural frequencies with small magnitudes in $\mathbf{e}$ to form the combination. However, such approach does not take the structure of the sensitivity matrix into consideration. An ill-conditioned sensitivity matrix may result in large estimation errors. In fact, the sensitivity matrix $\mathbf{S}$ can be simplified with less columns $\underline{\mathbf{S}}$ by Algorithm 2, where $\underline{\mathbf{S}}$ is the submatrix of $\mathbf{S}$ by removing columns corresponding to the zero elements in $\widehat{\Delta\boldsymbol{\alpha}}$, represented by $\mathbf{L}\left(\widehat{\Delta\boldsymbol{\alpha}}\right)$. For example, if $\mathbf{S}$ has dimension 7×20, the submatrix $\underline{\mathbf{S}}$ can be 7×2 by removing all columns that correspond to the healthy elements. Eq. (3.15) and (3.16) can be re-written as:

$$\Delta\boldsymbol{\lambda} = \underline{\mathbf{S}}\Delta\underline{\boldsymbol{\alpha}}^{\text{truth}} + \mathbf{e} \tag{3.17}$$

and

$$\Delta\boldsymbol{\lambda}^{(k)} = \underline{\mathbf{S}}^{(k)}\Delta\underline{\boldsymbol{\alpha}}^{\text{truth}} + \mathbf{e}^{(k)} \tag{3.18}$$

where $\Delta\underline{\boldsymbol{\alpha}}^{\text{truth}}$ is the subset of $\Delta\boldsymbol{\alpha}^{\text{truth}}$ with non-zero valued components and $\underline{\mathbf{S}}^{(k)}$ is the submatrix of $\mathbf{S}^{(k)}$ by removing the columns corresponding to zero elements in $\Delta\boldsymbol{\alpha}^{\text{truth}}$. Following the previous examples, if $\mathbf{S}^{(k)}$ has dimension 4×20, then $\underline{\mathbf{S}}^{(k)}$ is 4×2. We would like to point out that the number of selected natural frequencies should be larger than the number of nonzero

elements in $\Delta\underline{\boldsymbol{\alpha}}^{\text{truth}}$ so that $\underline{\mathbf{S}}^{(k)}$ will be a square or tall matrix. In this way, Eq. (3.18) will not be an underdetermined system.

According to Eq. (3.18) and the least squares method, the closed form solution of $\Delta\underline{\boldsymbol{\alpha}}^{\text{truth}}$ is:

$$\Delta\underline{\boldsymbol{\alpha}}^{\text{truth}} = \left(\underline{\mathbf{S}}^{(k)\mathbf{T}}\underline{\mathbf{S}}^{(k)}\right)^{-1}\underline{\mathbf{S}}^{(k)\mathbf{T}}(\Delta\boldsymbol{\lambda}^{(k)} - \mathbf{e}^{(k)}) \tag{3.19}$$

Similarly, the estimation of the damages upon the kth combination of natural frequencies can be solved from $\Delta\boldsymbol{\lambda}^{(k)} = \underline{\mathbf{S}}^{(k)}\Delta\boldsymbol{\alpha}$ (i.e., the approximation of Eq. (3.18)) by the least square method as:

$$\widehat{\Delta\underline{\boldsymbol{\alpha}}}^{(k)} = \left(\underline{\mathbf{S}}^{(k)\mathbf{T}}\underline{\mathbf{S}}^{(k)}\right)^{-1}\underline{\mathbf{S}}^{(k)\mathbf{T}}(\Delta\boldsymbol{\lambda}^{(k)}) \tag{3.20}$$

Considering Eqs. (3.19) and (3.20), we have

$$\left\|\widehat{\Delta\underline{\boldsymbol{\alpha}}}^{(k)} - \Delta\underline{\boldsymbol{\alpha}}^{\text{truth}}\right\|_2 = \left\|\left(\underline{\mathbf{S}}^{(k)\mathbf{T}}\underline{\mathbf{S}}^{(k)}\right)^{-1}\underline{\mathbf{S}}^{(k)\mathbf{T}}\mathbf{e}^{(k)}\right\|_2 \tag{3.21}$$

This derivation inspires us to use $\left\|\left(\underline{\mathbf{S}}^{(k)\mathbf{T}}\underline{\mathbf{S}}^{(k)}\right)^{-1}\underline{\mathbf{S}}^{(k)\mathbf{T}}\mathbf{e}^{(k)}\right\|_2$ as the criteria for natural frequency selection. Specifically, we define $\left\|\left(\underline{\mathbf{S}}^{(k)\mathbf{T}}\underline{\mathbf{S}}^{(k)}\right)^{-1}\underline{\mathbf{S}}^{(k)\mathbf{T}}\mathbf{e}^{(k)}\right\|_2$ as $b^{(k)}$ and the optimal combination of natural frequencies can be chosen as $k^* = \arg_{\mathrm{k}}\min b^{(k)}$. We would like to point out that $b^{(k)}$ is just an approximation of $d^{(k)}$ in Eq. (3.14) because $\widehat{\Delta\boldsymbol{\alpha}}^{(k)}$ in Eq. (3.14) is often different from $\widehat{\Delta\underline{\boldsymbol{\alpha}}}^{(k)}$ obtained in Eq. (3.20). In fact, the accuracy of $\widehat{\Delta\underline{\boldsymbol{\alpha}}}^{(k)}$ is often higher than $\widehat{\Delta\boldsymbol{\alpha}}^{(k)}$ and the above derivation Eqs. (3.19-21) are only used to obtain an approximation of $d^{(k)}$.

To compute $b^{(k)}$, we also need the value of the error term $\mathbf{e}$. The value of $\mathbf{e}$ can be estimated by $\hat{\mathbf{e}} = \Delta\boldsymbol{\lambda} - \mathbf{S}\widehat{\Delta\boldsymbol{\alpha}}$, where $\widehat{\Delta\boldsymbol{\alpha}}$ is the output from Algorithm 2. To summarize, the proposed natural frequency selection algorithm is shown as Algorithm 3 in Table 3-3.

Table 3-3. Algorithm 3: Natural Frequency Selection Algorithm for Bias Reduction

RUN Algorithm 2
CALCULATE the estimated error $\hat{\mathbf{e}} = \Delta\boldsymbol{\lambda} - \mathbf{S}\widehat{\Delta\boldsymbol{\alpha}}$
For $k = 1,2, \dots, 2^m - 1$
  CALCULATE the estimated bias $\hat{b}^{(k)}$
End
Return $k^* = \arg_k \min \hat{b}^{(k)}$ as the final combination

There are several remarks on Algorithm 3. First, $\widehat{\Delta\boldsymbol{\alpha}}$ is pre-computed in Algorithm 2, so that the computational load does not explode for exhausting all possible measurement combinations. In fact, as we mentioned earlier, the number of the selected natural frequency needs to be larger than the number of non-zero elements in $\widehat{\Delta\boldsymbol{\alpha}}$. Thus, the actual number of combinations is further reduced. For example, if $\underline{\mathbf{S}}$ has dimension 7×2, the combination should contain at least 2 natural frequencies. Second, the proposed algorithm will not guarantee the selected combination k^* is the optimal one that minimize Eq. (3.14) because the criteria used $b^{(k)}$ is just an approximation of $d^{(k)}$. Detailed numerical studies and discussions will be conducted to illustrate the performance of the proposed algorithms in Section 3.5 and 3.6.

3.5 Numerical Study and Illustration

In this section, the proposed algorithm is validated using a fixed-free beam setup. The system parameters are summarized in Table 3-4.

Table 3-4. Parameters of the Beam Structure

Material	Young's Modulus	Density	Length	Width	Thickness	m	n
Aluminum	7.1×10^{10} N/m^2	$2700\text{kg}/m^3$	0.4184m	0.0381m	3.175mm	7	20

The beam consists 20 elements and the first 7 modes are available for measurements. Thus, there are total 127 different combinations of natural frequencies. In the first example, we are considering the beam with two faulty elements, where the stiffness loss occurs at elements 8 and 17 with $\Delta\alpha_8 = -0.3$ and $\Delta\alpha_{17} = -0.1$, respectively.

Figure 3-1 presents the bias $d^{(k)} = \left\|\widehat{\Delta\boldsymbol{\alpha}}^{(k)} - \Delta\boldsymbol{\alpha}^{\text{truth}}\right\|_2$ in Eq. (3.14) as a function of the combination index $k = 1,2,3,\ldots,127$. The combination is ordered from the single natural frequency to all seven natural frequencies, i.e., $\{1,2,3,\ldots,(1,2),(1,3),\ldots,(1,2,3),(1,2,4),\ldots,(1,2,3,4,5,6,7)\}$. $\widehat{\Delta\boldsymbol{\alpha}}^{(k)}$ is calculated by $\min\|\Delta\boldsymbol{\alpha}\|_1$, s.t. $\left\|\Delta\boldsymbol{\lambda}^{(\mathbf{k})} - \mathbf{S}^{(\mathbf{k})}\Delta\boldsymbol{\alpha}\right\|_2 \leq \epsilon$ with $\epsilon = 10^{-9}$.

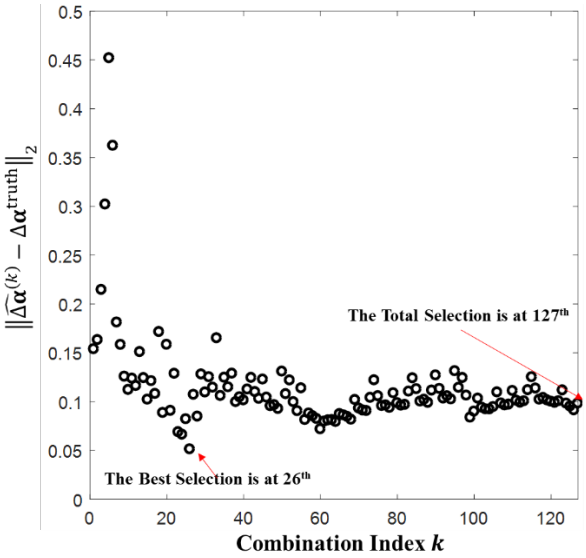

Figure 3-1. The bias of the estimated damages for different combinations of natural frequencies

It is clearly shown in Figure 3-1 that the combination of all seven natural frequencies (the 127th combination) does not result in the smallest bias. In this damage scenario, the smallest bias is obtained by the 26th combination of the fifth and sixth natural frequencies, i.e., (5, 6). From Figure 3-1, it can be seen that the bias has relatively large values for the first seven combinations. Since

the first seven combinations are all single natural frequencies, the linear system is underdetermined with two faulty elements. Also, there is a jump at $k = 18$, (the combination of the second and the seventh natural frequencies), which is due to the correlated structure of the second and the seventh rows in **S**. As discussed in section 3.4, the ill-posed sensitivity matrix may result in large errors even with regularization.

Figure 3-2 presents the results of the histogram of the severity estimation of 20 elements from Algorithm 1.

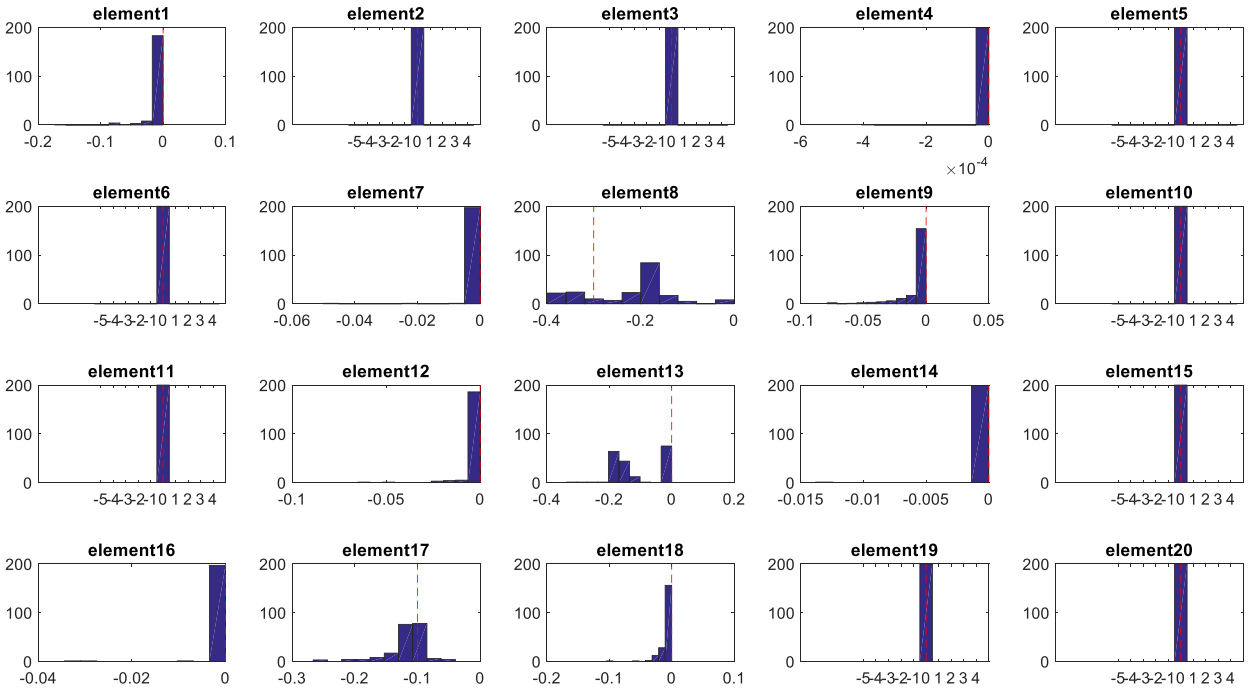

Figure 3-2. Damage parameter histogram of 20 elements with Algorithm 1. True damages of each element are labeled using dash lines.

In Figure 3-2, the true damage locations, i.e., elements 8 and 17, have histograms around the underlying true damages -0.3 and -0.1. Most of other elements have density concentrate exactly at 0 as expected, e.g., elements 2, 6 and 10. Elements 1, 4, 9 and 18 have the majority of the density concentrate at 0 with a light tail spreading to negative values. Element 13 has density concentrate

both at 0 and -0.2. It can be seen that true damage locations have densities apparently differ from 0, while non-damaged locations tend to have most density distributed at 0. These locations are set to $\Delta\hat{\alpha} = 0$ in the majority voting process.

Results after Algorithm 2 are shown in Figure 3-3. In Figure 3-3, the only two non-zero distributed elements are the element 8 and 17 with density concentrated around the true damage magnitudes. The estimated damage parameters are $\widehat{\Delta\alpha}_8 = -0.33$ and $\widehat{\Delta\alpha}_{17} = -0.11$ with all other $\widehat{\Delta\alpha}_{i\neq 8 \text{ or } 17} = 0$.

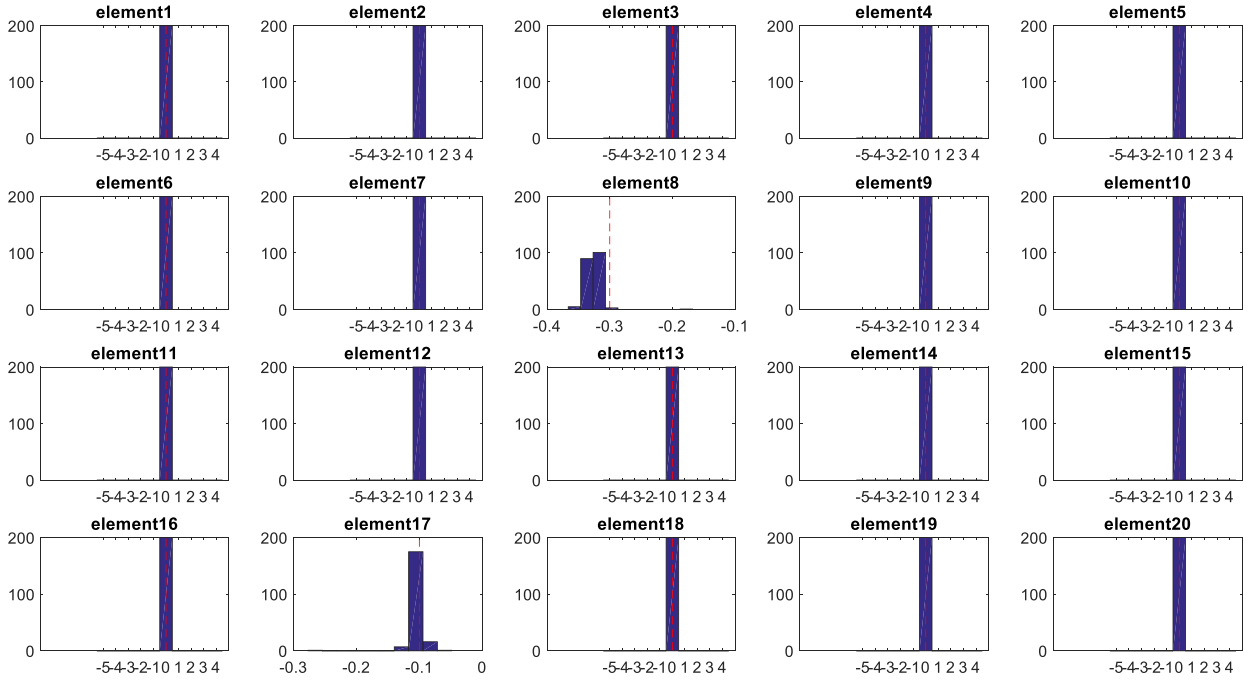

Figure 3-3. Damage parameter histogram of 20 elements after Algorithm 2. True damages of each element are labeled using dashed lines

The estimated bias $\hat{b}^{(k)}$ for $k = 8, 9, \ldots, 127$ are presented in Figure 3-4. It can be seen that $\hat{b}^{(k)}$ has very similar trend compared to $\left\|\widehat{\Delta\boldsymbol{\alpha}}^{(k)} - \Delta\boldsymbol{\alpha}^{\text{truth}}\right\|_2$. By Algorithm 3, we get $k^* = 26$ and the result is consistent with the smallest bias combination as shown in Figure 3-1. Thus, only the

fifth and sixth natural frequencies are suggested to be included in the estimation of damage parameters to reduce the estimation bias. Please note that the comparison between the estimated bias $\hat{b}^{(k)}$ and the $\left\|\widehat{\Delta\boldsymbol{\alpha}}^{(k)} - \Delta\boldsymbol{\alpha}^{\text{truth}}\right\|_2$ is only shown for $k \geq 8$. Two elements are identified as stiffness loss by Algorithm 2. In order to apply the least square method in Eq. (3.19), $\underline{\mathbf{S}}^{(k)}$ should consist at least two rows, i.e., combination of at least two natural frequencies. Thus, $k \geq 8$ because the first 7 combinations only contain one natural frequency.

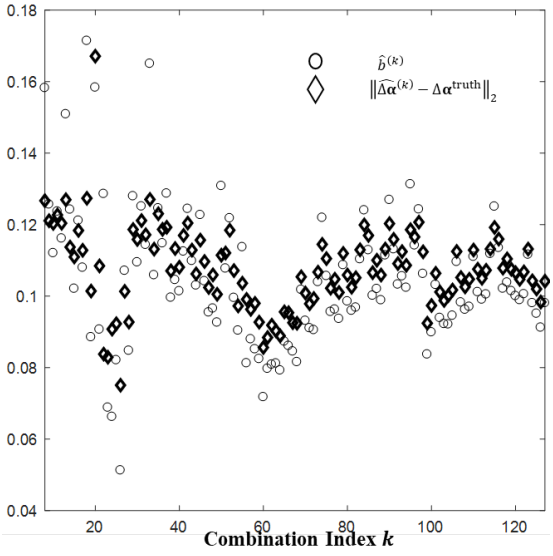

Figure 3-4. Plots of $\hat{b}^{(k)}$ and $d^{(k)}$ for $k = 8, 9, \ldots, 127$.

Figure 3-5 presents the comparison results of the damage parameter estimation using different methods.

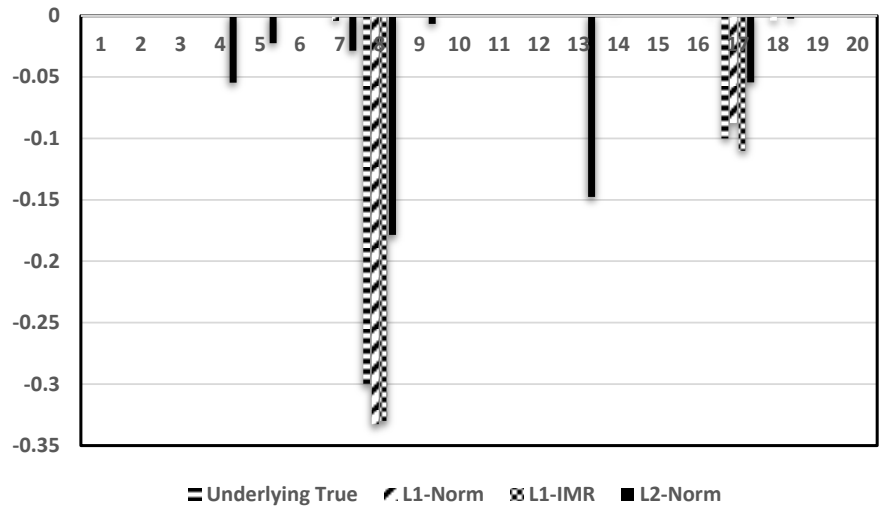

Figure 3-5. Comparison of damage parameter estimation using different approaches.

The L_1- Norm method adopts Eq. (3.12), and the L_1-IMR adopts the proposed method with iterative matrix randomization, i.e., $\widehat{\boldsymbol{\Delta\alpha}}$ by Algorithm 2. The L_2- Norm adopts Eq. (3.12) but without L_2 penalty. It can be seen from the comparison, the L_1-IMR returns the most accurate estimation both for the damage locations and damage severities. The L_1- norm method returns comparable results at the true damage locations, but also has estimation with small magnitudes on a few healthy elements. The L_2- norm performs the worst among all three methods with distributed estimation along elements.

In the following, the proposed algorithm is adopted for a scenario with three faulty elements, where $\Delta\alpha_3 = -0.1$, $\Delta\alpha_{10} = -0.2$ and $\Delta\alpha_{18} = -0.2$. The histogram of elements after Algorithm 2 is presented in Figure 3-6. Similar to the case with two faulty elements, the true damage locations are identified correctly.

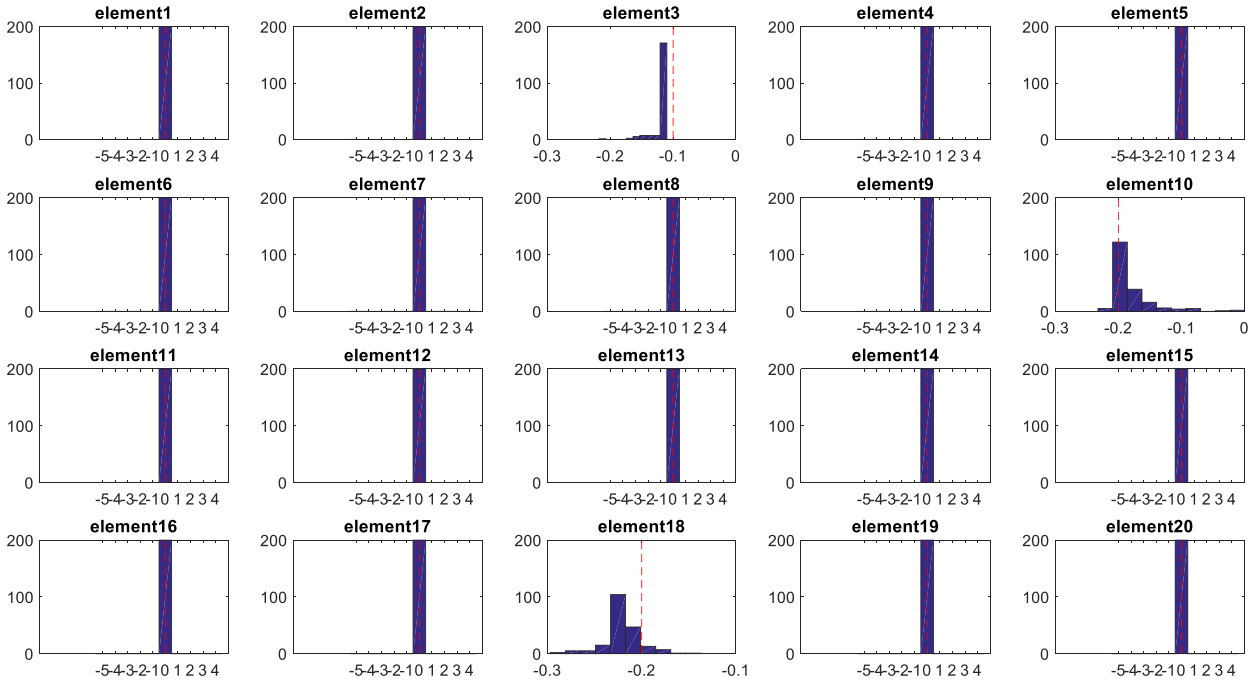

Figure 3-6. Damage parameter histogram of 20 elements after Algorithm 2. True damages of each element are labeled using dash lines

The comparison between $\hat{b}^{(k)}$ and the $\left\|\widehat{\Delta\boldsymbol{\alpha}}^{(k)} - \Delta\boldsymbol{\alpha}^{\text{truth}}\right\|_2$ is presented in Figure 3-7. Since three damage locations are identified, at least three natural frequencies are needed, i.e., $k \geq 29$. By Algorithm 3, $k^* = 43$ with the first, the sixth and the seventh natural frequencies is the combination with the smallest bias in the estimation. The jumpy peaks for some $\hat{b}^{(k)}$s are due to the correlated structure of $\underline{\mathbf{S}}^{(\mathrm{k})}$**.** In Figure 3-8, the comparison of damage parameter estimation is presented. The proposed L_1-IMR has the best estimation.

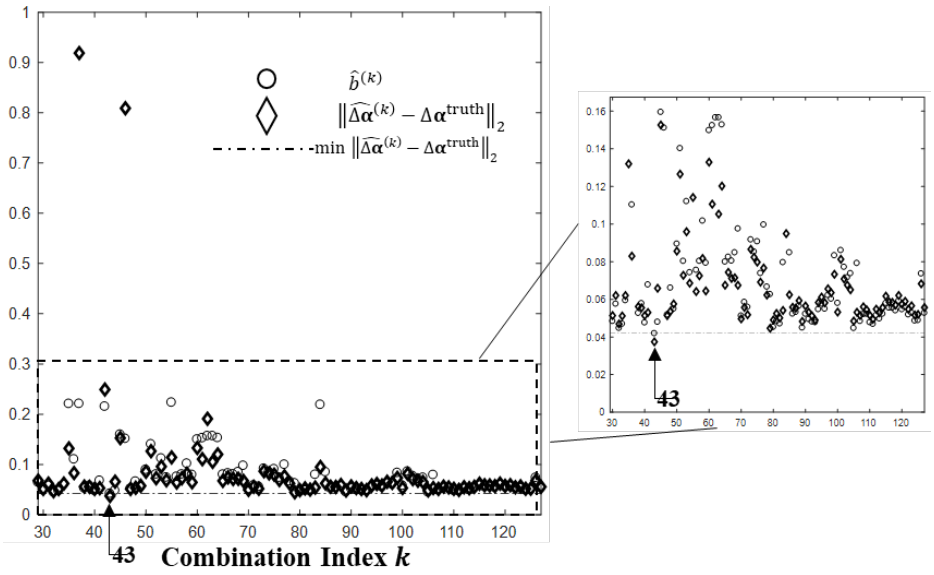

Figure 3-7. Plots of $\hat{b}^{(k)}$ and the $\left\|\widehat{\Delta\boldsymbol{\alpha}}^{(k)} - \Delta\boldsymbol{\alpha}^{\text{truth}}\right\|_2$ for $k = 29, 30, \ldots, 127$.

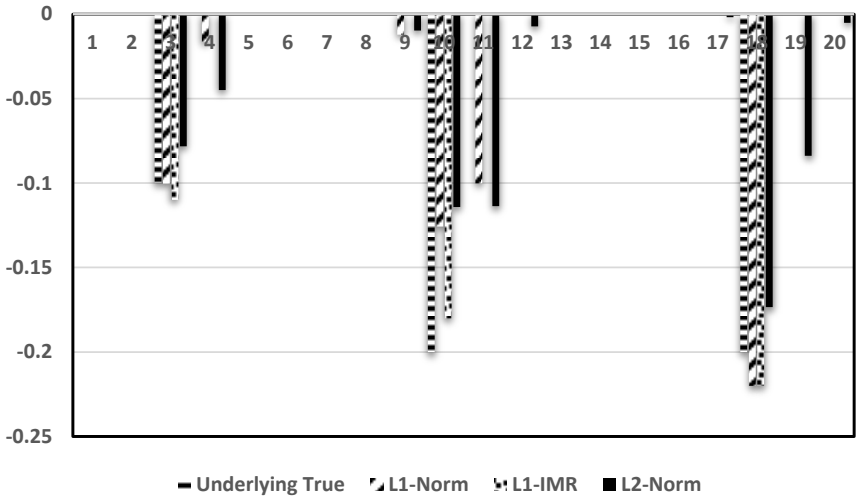

Figure 3-8. Comparison of damage parameter estimation using different approaches

In Table 3-5 we present the overall performance of the proposed algorithm in a comprehensive study. The study adopts the same beam structure in previous two examples (i.e., Table 3-2) and exhausts all possible combinations between damage locations and damage severities for $-0.4 \leq \Delta\alpha \leq -0.05$ with increment 0.05. In most cases, 5% decrease in natural frequencies can be referred to a severe damage in the structure [192-193]. According to the finite element model, the 5% reduction in natural frequencies is roughly equivalent to $\Delta\alpha = -0.4$.

Table 3-5. Performance of the Proposed Algorithm in Different Damage Scenarios

	Single Fault	Two Faults	Three Faults
$k^* = \arg_k \min d^{(k)}$	94.3%	83.5%	80.2%
$d^{(k^*)} \leq d^{(127)}$	97.1%	94.7%	91.5%
# simulations	160	12160	583680

In the simulation study, we consider three fault scenarios, single fault, two faults and three faults. The performance is measured in two ways. 1) $k^* = \arg_k \min d^{(k)}$ indicates the selected combination k^* by Algorithm 3 is the optimal combination that minimizes the bias. It can be seen the proposed algorithm can detect the optimal combination above 80 percentage in all three damage scenarios. 2) $d^{(k^*)} \leq d^{(127)}$ indicates that the selected combination k^* has smaller bias compared with the case when all natural frequencies are used. It can be seen that the selected combination by the proposed algorithm can achieve smaller bias than using all seven natural frequencies over 90 percentage in all three damage scenarios. It is not surprising to see the single fault scenario has the best performance, in which case the Eq. (3.19) is reduced to the scalar calculation without any matrix inversion.

3.6 Factors that Influence the Estimation Performance

In this section, we discuss the factors that influence the performance of the proposed algorithm. The proposed algorithm is effective on selection of natural frequencies to reduce the estimation bias. However, it does not eliminate the bias. In Figure 3-9, we present the accuracy of linear approximation of natural frequency compared with the underlying truth. The beam is set up as that in Table 3-4 with stiffness loss only at element 8.

Figure 3-9(a) presents the linear approximation of the first order natural frequency. The solid line is the underlying truth and the dashed line is the linear approximation. Since Taylor's expansion is conducted at the healthy condition, the difference between the linear approximation

and the underlying truth is getting larger as $\Delta\alpha \to -1$. Figure 3-9(b) summarizes the accuracy of the linear approximation of the first seven modes in terms of the difference in percentage, i.e., $\frac{\Delta\lambda - \mathbf{S}^{(k)}\Delta\boldsymbol{\alpha}^{\text{truth}}}{\Delta\lambda}$.

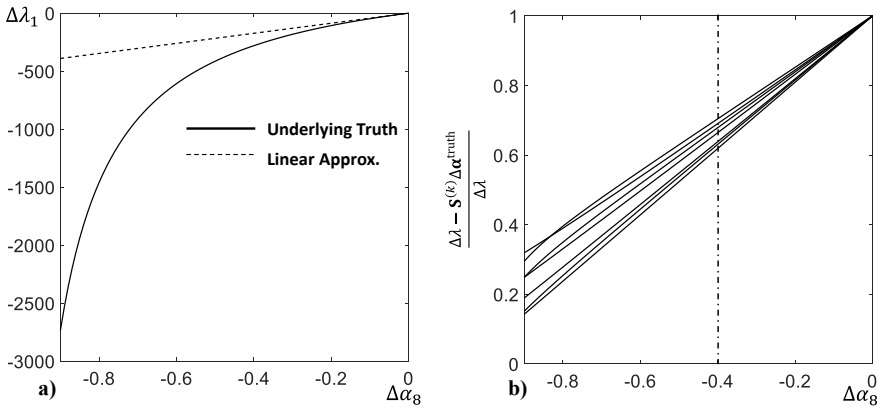

Figure 3-9. Accuracy of linear approximation in natural frequencies

It can be seen that the accuracy is about 60% for $\Delta\alpha = -0.4$. As the comprehensive simulation study indicated in Section 3.4, the proposed algorithm performs well at such accuracy level. It is worth noting that the performance of the algorithm gets worse for severe stiffness loss. Under mild damage conditions, the histogram of $\Delta\alpha$s are close to the underlying truth but with small differences (e.g., Figure 3-3 and 3-5). For severe damage loss, such differences can be large or even the identified damage locations can be wrong. In Figure 3-10, we present an example of the histogram of $\Delta\alpha$s after Algorithm 2 for a severe damage case $\Delta\alpha_3 = -0.9$, $\Delta\alpha_{10} = -0.9$ and $\Delta\alpha_{18} = -0.2$.

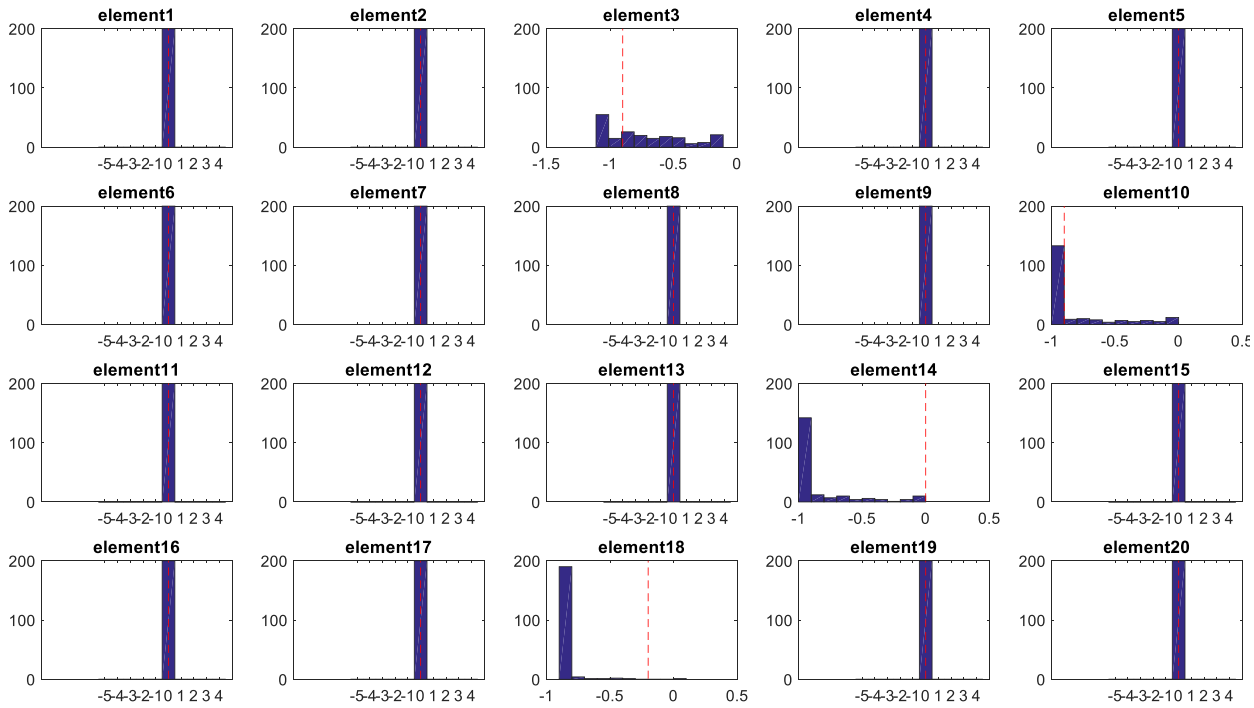

Figure 3-10. Damage parameter histogram of 20 elements after Algorithm 2. True damages of each element are labeled using dashed lines

All three true damage locations are identified but with an additional element 14 wrongly identified. The magnitude of stiffness loss at element 18 is estimated much smaller than the truth due to the additional element. Thus, the results of the proposed algorithm will not be informative on the selection of natural frequencies as shown in Figure 3-11.

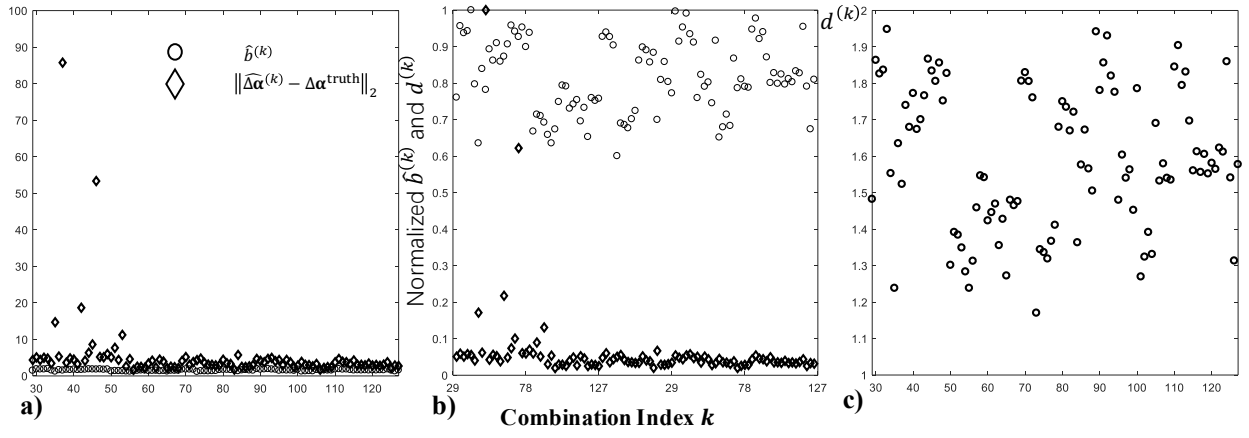

Figure 3-11. Plots of $\hat{b}^{(k)}$ with $\left\|\widehat{\Delta\boldsymbol{\alpha}}^{(k)} - \Delta\boldsymbol{\alpha}^{\text{truth}}\right\|_2$ for $k = 29, 30, \ldots, 127$ with severe damage

Figure 3-11(a) is similar to Figure 3-4 or 3-7 showing the comparison between $\hat{b}^{(k)}$ and $\left\|\widehat{\Delta\boldsymbol{\alpha}}^{(k)} - \Delta\boldsymbol{\alpha}^{\text{truth}}\right\|_2$. Since they have quite difference scales, the normalized comparison is shown in Figure 3-11(b). As expected, the two trends are different. For such severe damage scenario, the inaccuracy of the linear approximation causes the overall estimated damage parameters biased from the underlying truth as shown in Figure 3-11(c). Figure 3-11(c) presents the bias $d^{(k)}$. It can be seen the average bias for this severe damage case is around 1.7, which is roughly 17 times large than the bias shown in Figure 3-1.

In practice, it is more important to estimate mild damage conditions. Severe damages not only reduce natural frequencies significantly, but also cause visible changes in structures. However, mild damages can be hidden from simple visual inspection. Thus, it is more important to identify mild damages accurately for preventive repair or correction.

3.7 Conclusion

In this paper, we propose a natural frequency selection algorithm to reduce the bias in the estimation of damage parameters using linear approximation under mild damage scenarios. The selected combination of natural frequency has high probability to be the optimal combination which leads to the smallest bias in the estimation among all the possible combinations. The algorithm consists three sub-algorithms. In the first algorithm, the L_1- norm regularization with iterative matrix randomization is adopted for estimation of damage parameters followed by a majority voting process. In the second algorithm, the damage locations are identified by sequential updating. The improved estimation L_1- IMR helps to choose the best combination of

measurements in the third algorithm. The effectiveness of the proposed method is validated through numerical studies. Factors that influence the performance of the method are also discussed.

The proposed algorithm is flexible in dealing with natural frequencies, thus has potential to be extended to the structures with physical modification, e.g., modification through mass addition or tunable sensing systems. The proposed algorithm can be applied to select measurements among different setups of the structure (i.e., different mass additions or tunable inductances), which may provide a better estimation than combining all available modes from all setups. We will investigate along this direction and report our findings in the near future.

3.8 Appendix

Table 3A-1 Iterative Reweighted L_1 Minimization Algorithm [15]

1. Set the iteration count $l = 0$ and $w_i^{(o)} = 1, i = 1,2, \dots n$
2. Solve the weighted L_1 minimization problem:
   $\mathbf{x}^{(l)} = \arg\min \left\| \mathbf{W}^{(l)} \mathbf{x} \right\|_1$, subject to $\|\mathbf{y} - \mathbf{A}\mathbf{x}\|_2 \leq \epsilon$
3. Update the weights for $i = 1,2, \dots n$
   $$w_i^{(l+1)} = \frac{1}{\left| x_i^{(l)} + \delta \right|}$$
4. Terminate on convergence or l attains the maximum number. Otherwise, increment l and go to step 2.

4. Prognosis of Structural Damage Growth Via Integration of Physical Model Prediction and Bayesian Estimation*

In this chapter, we propose a dynamic data-driven hierarchical Bayesian degradation model, which takes advantage of both the physical finite element model and the data driven Bayesian framework, to tackle the structural damage growth prediction. The damage growth trend can be efficiently and accurately estimated by Gibbs sampling. Systematic case analyses are performed to validate and demonstrate the effectiveness of the proposed method.

4.1 Introduction

Damage diagnosis and prognosis play an important role in ensuring the safety of mechanical, aerospace, and civil structures. Most types of damage or structural weakness cannot be observed directly. Rather, damage will cause the change in structural properties (e.g., local stiffness, damping ratio) and then in turn impact on the dynamic responses of the structure. Studies on inversely estimating the structural properties using observed response signals are mostly limited to detection in a static sense, in which only a snap-shot of data within a short time window are used to get a point value estimate of the damage [72,73]. However, revealing the evolving path of structural damage is highly desirable in practice, because the damage future evolving path can provide more accurate information regarding the remaining useful life (RUL) of the structure.

Physic-based approach is a popular way to predict the structural damage evolving over time. Such methods are mostly based on deterministic differential equations for the damage growth rate

*This chapter is based on the paper: **Liu, Yuhang**, Qi Shuai, Shiyu Zhou, and Jiong Tang. "Prognosis of Structural Damage Growth Via Integration of Physical Model Prediction and Bayesian Estimation." IEEE Transactions on Reliability 66, no. 3 (2017): 700-711.

[74]. In these methods, the model is tuned for prognosis by minimizing residuals which are the difference between the real measurements and the outputs of a mathematical model. For instance, an integrated prognostic process based on data collected from model-based simulations under nominal and degraded conditions is proposed in [75]. A defect propagation model by mechanistic modeling approach for RUL estimation of bearings is introduced in [76]. Paris' law is widely used for crack growth estimation [6,7]. There are some inherent drawbacks of the physical models. First, the physical models are generally case specific, which limit their application to broad types of structures. Second, these methods assume that an accurate mathematical model is available and the model requires specific mechanistic knowledge and theories relevant to the systems under consideration. In practice, it is very difficult to build such a good physical model. Furthermore, physics based methods often ignore the uncertainties in the system structure and the measurements. Most recent research along the physic-based approach introduces the randomness by adding random disturbances [77], random parameters [78] to the differential equation, or directly making the growth rate a random process [14,79-81]. As a trade-off for such modification, modelling incurs heavy computational load.

Different from physic-based approach, data-based or data-driven methods adopt generic statistical models to describe the damage progression. Temporal and spatial data recorded by sensors inherently carries the physical information of the system and such information can be utilized to elucidate the relationship between system status and the observed data. In data-driven approaches, the statistical analysis can be less dependent on physical principles and easily applied to different systems with relatively low computational cost. A popular category of data driven methods is to model the sensing signal directly using stochastic process or degradation path model [82]. The prognosis is based on the prediction of the future trend of the signals conditioned on the

existing data. For example, Wiener process is adopted for degradation data analysis with measurement errors in [83]. A good review on degradation path models with simulation comparisons can be found in [82]. These approaches leave the prognosis on the data level without further revealing the change in structural properties. State space model is a type of method capable of characterizing the underlying status of structure as different states. Hidden Markov model (HMM) is one of the state space approaches, where the unobservable degradation status is defined as hidden states. HMM have been adopted for damage prognosis of a pre-stressed concrete bridge [11] and is used for prediction of gear failures [12]. Typically, a large amount of historical data is needed for training HMM and the assumptions in HMM are often not realistic in many cases. Also, since degradation status is classified into discrete states as an approximation of the underlying true continuous state, the prognosis in a long term could be unreliable. One major disadvantage of pure data-driven based methods is that although they can provide a trend estimate for the observed data, they often cannot reveal the root cause or the structural damage that causes the data trend directly. As a result, currently available data-driven method often performs poorly when trying to classify the type of changes in the structural properties compared to the physical models.

In this chapter, we propose a dynamic data-driven hierarchical Bayesian degradation model, which takes advantage of both the physical finite element model (FEM) for response prediction and the data driven Bayesian framework. This hierarchical model is capable to recover the evolving path of the structural damages over time or load cycles efficiently based on temporal sensing data. FEM is an effective numerical tool for modelling structural dynamics [84]. In our model, FEM is adopted to approximate the mapping from the structural properties to the observed data, i.e., natural frequencies. Bayesian framework or Bayesian updating provides a powerful parameter estimation method from noisy data by assigning appropriate prior distributions and

likelihood functions [85,86]. Our proposed model is a hierarchical Bayesian model consisting of two levels. In the first level, the observed data is assumed to follow a Gaussian distribution with a mean function related to structural properties. In the second level, the evolving path of the structural properties is described using polynomials with uncertainties. Conjugate prior distributions are assigned for each unknown parameter for the sake of simplifying the derivation in posteriors distribution. All the unknown parameters are estimated using Markov Chain Monte Carlo (MCMC) sampling technique. Akaike's Information Criterion is adopted for choosing the most appropriate degree of polynomial in fitting the underlying trend of the damage evolving path. This work provides an efficient damage growth estimation framework by combining physics-based and data-driven based methods. Note that, the work focuses on the estimation and prediction of the evolving trend of structural properties instead of the traditional RUL prediction [87].

The rest of the chapter is organized as follows. Section 4.2 introduces the mathematical formulation of the dynamic data-driven hierarchical Bayesian degradation model followed by parameter estimation and model selection. Systematic case analyses are performed to validate the effectiveness of the proposed method in Sections 4.3 and 4.4. Finally, the chapter ends with conclusion in Section 4.5.

4.2 Dynamic Data-Driven Hierarchical Bayesian Degradation Model

In this section, the mathematical formulation of the dynamic data-driven hierarchical Bayesian degradation model is presented followed by parameter estimation procedure and model selection process.

4.2.1 Model Formulation

In the context of the finite element model (FEM), the dynamics of an undamped structural system can be described by the linear equation

$$\boldsymbol{M}\ddot{\boldsymbol{z}}(t) + \boldsymbol{K}\boldsymbol{z}(t) = \boldsymbol{G}(t) \tag{4.1}$$

where $\boldsymbol{M}$ and $\boldsymbol{K}$ are the global mass and stiffness matrices, respectively, $\boldsymbol{z}$ and $\boldsymbol{G}$ contain the nodal displacements and nodal forces, respectively. The characteristic features of the system are the circular natural frequencies ω_i (rad/s) and mode shapes $\boldsymbol{\phi_i}$, which can be calculated from the eigenvalue problem $(\boldsymbol{K} - \omega_i^2\boldsymbol{M})\boldsymbol{\phi_i} = 0$ with eigenvalue $\lambda_i = \omega_i^2$. Therefore, the changes of material properties in $\boldsymbol{M}$ or $\boldsymbol{K}$ lead to the changes of system features ω_i and $\boldsymbol{\phi_i}$. In practice, the damage of a structure is often characterized as the stiffness loss in elements [88-90], i.e., the values change in $\boldsymbol{K}$, and causes the reduction in natural frequencies $f = \frac{\omega}{2\pi}$ (Hz), which is commonly used for assessing system stiffness loss for its high accuracy and easiness in measurements. Damage assessment based on natural frequencies can be found in a large amount of literatures (e.g., [91]).

In this chapter, θ_t is used to describe the percentage of stiffness left at an element in the structural system along time t, thus θ_t ranges from 1 to 0. Without loss of generality, we assume the location of the damaged element has been determined and we will focus on estimating the evolution of the magnitude of the damage along time. For a system under regular load cycles, we assume the parameter θ_t follows a degradation path which cannot be observed directly. The proposed model takes natural frequencies f_{ti} as the observed data to estimate such degradation path, where f_{ti} denotes the i^{th} natural frequency measured at time t. Even if f_{ti} can be measured accurately, small perturbations can be involved in the measurements. To accommodate such uncertainties in f_{ti}, it is assumed that f_{ti} follows a normal distribution with mean $\eta_i(\theta_t)$ and variance σ_f^2, that is $f_{ti} \sim \mathcal{N}\left(\eta_i(\theta_t), \sigma_f^2\right)$, where $\eta_i(\theta_t)$ defines the mean value of f_{ti} for given

parameter θ_t. Variance σ_f^2 can be chosen to be small to reflect the high accuracy in natural frequency measurements.

In the proposed model, the mean function $\eta_i(\theta_t)$ is specified as a linear function $\eta_i(\theta_t) = u_i + v_i\theta_t$ with coefficients u_i and v_i for $\theta_t \in [l_\theta, u_\theta]$, where l_θ and u_θ are the boundaries of θ. Please note that in theory, the mean values of f_{ti} does not follow an exact linear function of θ_t. However, linear approximation can be used to describe the relationship in some regions of θ_t. This can be shown as follows. By eigenvalue perturbation theory [92],

$$\Delta\lambda_i \approx \frac{\boldsymbol{\phi_i^T \Delta K \phi_i}}{\boldsymbol{\phi_i^T \mathrm{M} \phi_i}} = \Delta\theta \times EI \times \frac{\boldsymbol{\phi_i^T G \phi_i}}{\boldsymbol{\phi_i^T M \phi_i}}$$

where E and I are the Young modulus of elasticity and second moment of inertia, respectively. $\Delta\theta = \theta_1 - \theta_2$ is the difference of the percentage of stiffness. $\boldsymbol{G}$ is a constant matrix containing the information of the given damage location. Note that $\Delta\lambda = f^2(\theta_1) - f^2(\theta_2)$, we can see that the change in natural frequencies can be approximated by

$$\Delta f = f(\theta_1) - f(\theta_2) = \frac{\Delta\theta \times const}{f(\theta_1) + f(\theta_2)} \approx \frac{\Delta\theta \times const}{f(\theta_1) + f(\theta_1) + f'(\theta_1) \times (\theta_2 - \theta_1)}$$

where $f(\theta_2)$ is expanded around θ_1 using Taylor's theorem neglecting higher order terms. Applying Taylor series expansion of Δf around $\Delta\theta = 0$, we have $\Delta f \approx \frac{\Delta\theta \times const}{2f(\theta_1)}$. Thus, the natural frequency is approximately linear with respect to the change in the system stiffness if the change is in a relatively small region.

In the proposed approach, we further model the evolving path of the damage θ_t by a polynomial function $\gamma(t) = \boldsymbol{\beta^T x_t}$, where $\boldsymbol{\beta}$ is the coefficient vector of the polynomial terms $\boldsymbol{x_t} = [1, t, t^2, \ldots]^T$. The underlying growth of damage could follow different function form [93], so it is infeasible to describe θ_t using a fixed function structure. Polynomial approximation is a robust

and flexible curve fitting technique so we adopt a polynomial function structure for the evolving path of θ_t. However, θ_t cannot be assumed to follow $\gamma(t)$ exactly because there are always modeling errors. Instead, a normal distribution is assigned to θ_t, that is $\theta_t \sim \mathcal{N}(\gamma(t), \sigma_\theta^2)$, where σ_θ^2 is the variance to capture modelling errors.

The proposed model is summarized as a 2-level hierarchical model as follows.

Level 1

$$f_{ti} \sim \mathcal{N}(\eta_i(\theta_t), \sigma_f^2), \quad i = 1,2 \ldots, N_f, t = 1,2,\ldots,T \tag{4.2}$$

$$\eta_i(\theta_t) = u_i + v_i\theta_t, \text{ with } u_i + v_i = f_{0i}$$

Level 2

$$\theta_t \sim \mathcal{N}(\gamma(t), \sigma_\theta^2) \tag{4.3}$$

$$\gamma(t) = \boldsymbol{\beta}^T \boldsymbol{x_t}, \text{ with } \boldsymbol{x_t} = [1, t, t^2, \ldots]^T$$

In Level 1, the measurement of natural frequencies f_{ti}s are assumed following a normal distribution with mean structure $\eta_i(\theta_t) = u_i + v_i\theta_t$ and variance σ_f^2. u_i and v_i are further relaxed to be unknown parameters except that their summation equals to f_{0i}, which is the natural frequencies under health condition. In Level 2, the weakness growth θ_t is assumed to follow a normal distribution with mean structure $\gamma(t)$ in polynomial form with variance σ_θ^2. In this model, we have unknown parameters $\boldsymbol{\beta}$, u_i, σ_f^2 and σ_θ^2 to be estimated in order to recover the evolving path of θ_t based on the observed temporal data f_{ti}.

4.2.2 Model parameter estimation

In order to utilize Bayesian framework for estimation, prior distributions need to be assigned to the unknown parameters to represent the initial guess of these parameters. Here, we set the prior

distributions as $\boldsymbol{\beta}\sim\mathcal{MN}\left(\boldsymbol{b},\sigma_\beta^2\boldsymbol{I}\right)$, $u_i\sim\mathcal{N}(\tau_i,\sigma_u^2)$, $\sigma_f^2\sim\mathcal{IG}\left(a_f,b_f\right)$ and $\sigma_\theta^2\sim\mathcal{IG}(a_\theta,b_\theta)$,where $\boldsymbol{\beta}$ follows multivariate distribution with mean vector $\boldsymbol{b}$ and covariance matrix $\sigma_\beta^2\boldsymbol{I}$. u_is are independently follow normal distribution with different mean values τ_is and a common variance σ_u^2. σ_f^2 and σ_θ^2 has Gamma distribution as priors. All the prior distributions are chosen as the conjugate priors, such that the posterior distributions are in the same distribution family of the prior distribution. The conjugate priors offer great computational convenience. Prior distributions play an important role in the Bayesian framework [94]. The prior distributions should reflect the available prior knowledge on the distribution parameters. However, when no prior knowledge is available, non-informative priors should be assigned in order to reduce the impact of the chosen priors on the parameters updating. For example, we could set σ_β^2 to be a very large value so that the multivariate prior normal distribution of $\boldsymbol{\beta}$ will be like a flat hyper-plane to reflect the non-preference in pre-choosing $\boldsymbol{\beta}$ in its support. In this chapter, we consider the general case where no specific prior information is available to us. As a result, proper values of σ_β^2, σ_u^2, (a_f,b_f) and (a_θ,b_θ) need to be assigned to achieve non-informative priors.

In the Bayesian framework, the estimation of a parameter is often the mean of its marginal posterior distribution, which can be calculated by integrating out other parameters in the joint posterior distribution given by Bayes' Theorem [95]. In the research, the joint posterior distribution of all the unknown model parameters is:

$$p\left(\boldsymbol{\Theta},\boldsymbol{\beta},\sigma_f^2,\sigma_\theta^2,\boldsymbol{U}\middle|\boldsymbol{\mathcal{F}}\right)\propto p\left(\boldsymbol{\mathcal{F}}\middle|\boldsymbol{\Theta},\sigma_f^2,\boldsymbol{U}\right)\times p\left(\boldsymbol{\Theta}\middle|\boldsymbol{\beta},\sigma_\theta^2\right)\times p(\boldsymbol{\beta}|\boldsymbol{b},\sigma_\beta^2)\times p(\sigma_f^2)\times p(\sigma_\theta^2)\times p(\boldsymbol{U}) \quad (4.4)$$

where $\boldsymbol{\mathcal{F}}_{\mathrm{TxN_f}}=[\mathbf{F}_1';\mathbf{F}_2';\ldots;\mathbf{F}_\mathrm{T}']$, and $\mathbf{F_t}=\left[f_{t1},f_{t2},..f_{tN_f}\right]'$, $\boldsymbol{\Theta}=[\theta_1,\theta_2,\ldots\theta_T]'$ $\boldsymbol{\eta}=\left[\eta_1,\ldots\eta_{N_f}\right]'$, and $\boldsymbol{U}=\left[u_1,u_2,..u_{N_f}\right]$. The explicit formulations of each term in the posterior distribution are:

$$
\begin{aligned}
&p\left(\boldsymbol{\mathcal{F}}\middle|\boldsymbol{\Theta},\sigma_f^2,\boldsymbol{U}\right)=\prod_{t=1}^{T}p\left(\mathbf{F_t}\middle|\theta_t,\sigma_f^2\right)\propto\prod_{t=1}^{T}\exp\left[\frac{\left(\mathbf{F_t}-\boldsymbol{\eta}(\theta_t)\right)'\left(\mathbf{F_t}-\boldsymbol{\eta}(\theta_t)\right)}{-2\sigma_f^2}\right]\\
&p\left(\boldsymbol{\Theta}\middle|\boldsymbol{\beta},\sigma_\theta^2\right)\propto\prod_{t=1}^{T}\exp\left[\frac{\left(\theta_t-\boldsymbol{\beta}^T\boldsymbol{x_t}\right)^2}{-2\sigma_\theta^2}\right]\\
&p(\boldsymbol{\beta}|\boldsymbol{b},\sigma_\beta^2)\propto\ \exp\left[\frac{(\boldsymbol{\beta}-\boldsymbol{b})'(\boldsymbol{\beta}-\boldsymbol{b})}{-2\sigma_\beta^2}\right]\\
&p(\sigma_f^2)\propto\left(\sigma_f^2\right)^{-a_f+1}\exp\left(\frac{-b_f}{\sigma_f^2}\right)\\
&p(\sigma_\theta^2)\propto\left(\sigma_\theta^2\right)^{-a_\theta+1}\exp\left(\frac{-b_\theta}{\sigma_\theta^2}\right)\\
&p(\boldsymbol{U}|\tau_i,\sigma_u^2)\propto\prod_{i=1}^{N_f}\exp\left[\frac{(u_i-\tau_i)^2}{-2\ \sigma_u^2}\right]
\end{aligned}
\tag{4.5}
$$

To estimate parameter $\boldsymbol{\beta}$, the marginal posterior distribution of $\boldsymbol{\beta}$, $p(\boldsymbol{\beta}|\boldsymbol{\mathcal{F}})$, can be evaluated by integrating as follows:

$$p(\boldsymbol{\beta}|\boldsymbol{\mathcal{F}})=\iiiint p\left(\boldsymbol{\Theta},\boldsymbol{\beta},\sigma_f^2,\sigma_\theta^2,\boldsymbol{U}\middle|\boldsymbol{\mathcal{F}}\right)d\boldsymbol{\Theta}d\sigma_f^2d\sigma_\theta^2d\boldsymbol{U}$$

With the marginal posterior distribution, we can further compute the mean value of the parameters as follows as an estimate of the parameter values.

$$E(\boldsymbol{\beta}|\boldsymbol{\mathcal{F}})=\int p(\boldsymbol{\beta}|\boldsymbol{\mathcal{F}})d\boldsymbol{\beta}$$

The concept is simple but in practice the multiple integrals can be very difficult to compute for high dimensional variables. To avoid such computational issue in finding $p(\boldsymbol{\beta}|\boldsymbol{\mathcal{F}})$, a Gibbs sampling technique is adopted. Gibbs sampling, a Markov Chain Monte Carlo algorithm, is an effective method for high dimensional parameters estimation [96]. The algorithm is summarized in Table 4-1.

Table 4-1. Illustration of Gibbs Sampling Algorithm

Initialize $\theta_t^{(0)}, \boldsymbol{\beta}^{(\mathbf{0})}, {\sigma_f^2}^{(0)}, \sigma_\theta^{2(0)}, u_i^{(\mathbf{0})}$

For k in **iteration** $1{:}\,K$

$$\theta_t^{(k)} \sim p\left(\theta_t \middle| \boldsymbol{\Theta}_{-\mathrm{t}}^{(\boldsymbol{k-1})}, \boldsymbol{\beta}^{(\boldsymbol{k-1})}, \sigma_\theta^{2(k-1)}, {\sigma_f^2}^{(k-1)}, \boldsymbol{U}^{(\boldsymbol{k-1})}, \boldsymbol{\mathcal{F}}\right)$$

$$\boldsymbol{\beta}^{(\boldsymbol{k})} \sim p\left(\boldsymbol{\beta} \middle| \boldsymbol{\Theta}^{(\mathbf{k})}, \sigma_\theta^{2(k-1)}, {\sigma_f^2}^{(k-1)}, \boldsymbol{U}^{(\boldsymbol{k-1})}, \boldsymbol{\mathcal{F}}\right)$$

$${\sigma_f^2}^{(k)} \sim p\left(\sigma_f^2 \middle| \boldsymbol{\Theta}^{(\mathbf{k})}, \sigma_\theta^{2(k-1)}, \boldsymbol{\beta}^{(\boldsymbol{k})}, \boldsymbol{U}^{(\boldsymbol{k-1})}, \boldsymbol{\mathcal{F}}\right)$$

$$\sigma_\theta^{2(k)} \sim p\left(\sigma_\theta^2 \middle| \boldsymbol{\Theta}^{(\mathbf{k})}, {\sigma_f^2}^{(k)}, \boldsymbol{\beta}^{(\boldsymbol{k})}, \boldsymbol{U}^{(\boldsymbol{k-1})}, \boldsymbol{\mathcal{F}}\right)$$

$$u_i^{(\boldsymbol{k})} \sim p\left(u_i \middle| \boldsymbol{\Theta}^{(\mathbf{k})}, \sigma_\theta^{2(k)}, {\sigma_f^2}^{(k)}, \boldsymbol{\beta}^{(\boldsymbol{k})}, \mathbf{U}_{-i}^{(\boldsymbol{k-1})}, \boldsymbol{\mathcal{F}}\right)$$

End

where $\theta_t^{(k)}$ is the k^{th} sample of θ_t drawing from the conditional posterior distribution $p\left(\theta_t \middle| \boldsymbol{\Theta}_{-\mathrm{t}}^{(\boldsymbol{k-1})}, \boldsymbol{\beta}^{(\boldsymbol{k-1})}, \sigma_\theta^{2(k-1)}, {\sigma_f^2}^{(k-1)}, \boldsymbol{U}^{(\boldsymbol{k-1})}, \boldsymbol{\mathcal{F}}\right)$. The other terms in the algorithms have the same interpretations. For a sufficient large number K, the samples of each parameter can be regarded as the samplings from the marginal posterior distribution [97]. For example, samples $\boldsymbol{\beta}^{(\boldsymbol{k})}$ can be viewed as generated from $p(\boldsymbol{\beta}|\boldsymbol{\mathcal{F}})$. With these samples, the sample mean can be used as the estimation of parameters, i.e., $\widetilde{\boldsymbol{\beta}} = \frac{1}{K}\sum_k \boldsymbol{\beta}^{(\boldsymbol{k})}$, where the $\sim$ sign indicates the values calculated from samples statistics generated by Gibbs sampling algorithm. Standard deviation can also be evaluated from samples to construct the confidence interval of the estimation.

In the hierarchical Bayesian degradation model, the conditional posterior distribution for each parameter in Table 4-1 can be derived using the properties of conjugate priors as follows. With these conditional posterior distributions, Monte Carlo sampling can be implemented.

a) The conditional posterior distribution of θ_t is a normal distribution with mean μ_t and variance ${\sigma_\mu}_t^2$.

$$p\left(\theta_t \middle| \boldsymbol{\Theta}_{-\mathrm{t}}, \boldsymbol{\beta}, \sigma_\theta^2, \sigma_f^2, \boldsymbol{U}, \boldsymbol{\mathcal{F}}\right) \propto p\left(\mathbf{F_t} \middle| \theta_t, \sigma_f^2, \boldsymbol{U}\right) \times p\left(\theta_t \middle| \boldsymbol{\beta}, \sigma_\theta^2\right)$$

$$\propto \exp\left[\frac{\left(\mathbf{F_t} - \boldsymbol{\eta}(\theta_t)\right)'\left(\mathbf{F_t} - \boldsymbol{\eta}(\theta_t)\right)}{-2\sigma_f^2}\right] \times \exp\left(\frac{(\theta_t - \boldsymbol{\beta}^T \boldsymbol{x_t})^2}{-2\sigma_\theta^2}\right)$$

$$= \exp\left[-\frac{1}{2}\left(\frac{\Sigma_{i=1}^{N_f}(f_{ti}-u_i-v_i\theta_t)^2}{\sigma_f^2}+\frac{(\theta_t-\boldsymbol{\beta}^T\boldsymbol{x_t})^2}{\sigma_\theta^2}\right)\right] \propto \exp\left[\frac{(\theta_t-\mu_t)^2}{-2\sigma_{\mu_t}^2}\right] \sim \mathcal{N}(\mu_t, {\sigma_{\mu}}_t^2)$$

where $\mu_t = \frac{\Sigma_{i=1}^{N_f} a_i b_i + cd}{\Sigma_{i=1}^{N_f} b_i^2 + d^2}$, ${\sigma_{\mu}}_t^2 = \frac{\sigma_f^2\sigma_\theta^2}{\Sigma_{i=1}^{N_f} b_i^2 + d^2}$, with $a_i = \sigma_\theta(f_{ti} - u_i)$, $b_i = \sigma_\theta v_i$, $c = \sigma_f \boldsymbol{\beta}^T \boldsymbol{x_t}$ and $d = \sigma_f$.

Note that, if $\eta_i(\cdot)$ takes non-linear form of θ_t, the above derivation may result in a very complicated formulation, in which case, slice sampling [98] can be used to sample from this density function.

b) The conditional posterior distribution of $\boldsymbol{\beta}$ is derived as:

$$p\left(\boldsymbol{\beta}\middle|\boldsymbol{\Theta}, \sigma_\theta^2, \sigma_f^2, \boldsymbol{U}, \boldsymbol{\mathcal{F}}\right) \propto p\left(\boldsymbol{\Theta}\middle|\boldsymbol{\beta}, \sigma_\theta^2\right) \times p(\boldsymbol{\beta}|\boldsymbol{b}, \sigma_\beta^2)$$

$$\propto \prod_{t=1}^{T} \exp\left[\frac{(\theta_t - \boldsymbol{\beta}^T\boldsymbol{x_t})^2}{-2\sigma_\theta^2}\right] \times \exp\left[\frac{(\boldsymbol{\beta}-\boldsymbol{b})'(\boldsymbol{\beta}-\boldsymbol{b})}{-2\sigma_\beta^2}\right] \sim \mathcal{MN}(\boldsymbol{b_{new}}, \boldsymbol{\Sigma_\beta})$$

where $\boldsymbol{b_{new}} = \boldsymbol{\Sigma_\beta}\left(\frac{\mathbf{X}^T\boldsymbol{\Theta}}{\sigma_\theta^2} + \frac{\boldsymbol{b}}{\sigma_\beta^2}\right)$ and $\boldsymbol{\Sigma_\beta} = \left(\sigma_\beta^{-2}\mathbf{I}_{3\times3} + \frac{\mathbf{X}^T\mathbf{X}}{\sigma_\theta^2}\right)^{-1}$.

c) The conditional posterior distribution of σ_f^2 is also a Gamma distribution with a_{fnew} and b_{fnew}.

$$p\left(\sigma_f^2\middle|\boldsymbol{\Theta}, \sigma_\theta^2, \boldsymbol{\beta}, \boldsymbol{U}, \boldsymbol{\mathcal{F}}\right) \propto p\left(\boldsymbol{\mathcal{F}}\middle|\boldsymbol{\Theta}, \sigma_f^2, \boldsymbol{U}\right) \times p\left(\sigma_f^2\right)$$

$$\propto \prod_{t=1}^{T} \sigma_f^{-N_f} \exp\left[\frac{\left(\mathbf{F_t} - \boldsymbol{\eta}(\theta_t)\right)'\left(\mathbf{F_t} - \boldsymbol{\eta}(\theta_t)\right)}{-2\sigma_f^2}\right] \times \left(\sigma_f^2\right)^{-a_f+1} \exp\left(\frac{-b_f}{\sigma_f^2}\right)$$

$$= \prod_{t=1}^{T} \sigma_f^{-N_f} \exp\left[-\frac{1}{2}\left(\frac{\Sigma_{i=1}^{N_f}(f_{ti}-u_i-v_i\theta_t)^2}{\sigma_f^2}\right)\right] \times \left(\sigma_f^2\right)^{-a_f+1} \exp\left(\frac{-b_f}{\sigma_f^2}\right) \sim \mathcal{IG}\left(a_{fnew}, b_{fnew}\right)$$

where $a_{fnew} = a_f + \frac{N_f T}{2}$ and $b_{fnew} = b_f + \left(\frac{\Sigma_{t=1}^{T}\Sigma_{i=1}^{N_f}(f_{ti}-u_i-v_i\theta_t)^2}{2}\right)$.

d) The conditional posterior distribution of σ_θ^2 has form:

$$p\left(\sigma_\theta^2\middle|\boldsymbol{\Theta}, \sigma_f^2, \boldsymbol{\beta}, \boldsymbol{U}, \boldsymbol{\mathcal{F}}\right) \propto p\left(\boldsymbol{\Theta}\middle|\boldsymbol{\beta}, \sigma_\theta^2\right) \times p\left(\sigma_\theta^2\right)$$

$$\propto \prod_{t=1}^{T} \sigma_\theta^{-1} \exp\left[\frac{(\theta_t - \boldsymbol{\beta}^T \boldsymbol{x_t})^2}{-2\sigma_\theta^2}\right] \times \left(\sigma_\theta^2\right)^{-a_\theta+1} \exp\left(\frac{-b_\theta}{\sigma_\theta^2}\right) \sim \mathcal{IG}(a_{\theta new}, b_{\theta new})$$

where $a_{\theta new} = a_\theta + \frac{T}{2}$ and $b_{\theta new} = b_\theta + \left(\frac{\sum_{t=1}^{T}(\theta_t - \boldsymbol{\beta}^T \boldsymbol{x_t})^2}{2}\right)$.

e) The conditional posterior distribution of u_i is derived as:

$$p\left(u_{\mathbf{i}} \middle| \boldsymbol{\Theta}, \sigma_\theta^2, \sigma_f^2, \boldsymbol{\beta}, \boldsymbol{U}_{-\mathbf{i}}, \boldsymbol{\mathcal{F}}\right) \propto p\left(\boldsymbol{\mathcal{F}} \middle| \boldsymbol{\Theta}, \sigma_f^2, u_{\mathbf{i}}\right) \times p(u_{\mathbf{i}}) = \prod_{t=1}^{T} p\left(\boldsymbol{F_t} \middle| \theta_t, \sigma_f^2, u_{\mathbf{i}}\right) \times p(u_{\mathbf{i}})$$

$$\propto \prod_{t=1}^{T} \exp\left[\frac{\left(\mathbf{F_{ti}} - \eta_i(\theta_t)\right)^2}{-2\sigma_f^2}\right] \times \exp\left[\frac{(\boldsymbol{u_i} - \boldsymbol{\tau_i})^2}{-2\sigma_u^2}\right] \sim \mathcal{N}(\boldsymbol{\mu_{u_i}}, \sigma_{u_i}^2)$$

where $\boldsymbol{\mu_{u_i}} = \frac{\sigma_u^2 \sum_{t=1}^{T}(1-\theta_t)(\mathbf{F_{ti}} - f_{0i}\theta_t) + \boldsymbol{\tau_i}\sigma_f^2}{\sigma_u^2 \sum_{t=1}^{T}(1-\theta_t)^2 + \sigma_f^2}$ and $\sigma_{u_i}^2 = \frac{\sigma_u^2 \sigma_f^2}{\sigma_u^2 \sum_{t=1}^{T}(1-\theta_t)^2 + \sigma_f^2}$.

4.2.3 Determination of the Degree of Polynomials in $\gamma(t)$

The unknown parameters can be effectively estimated by Gibbs sampling if the model structure is given. Thus, the proper degree of polynomials in $\gamma(t)$ needs to be decided, in order to recover the underlying evolving path of structural damage. The determination of the degree can be viewed as a model selection problem. Various model selection criteria have been developed for comparisons among different models. The most famous ones are Akaike's Information Criterion (AIC) [99], Bayesian Information Criterion (BIC) [100], and Bayes factor (BF) [101]. Among these selection criteria, we adopt AIC for selecting the best degree of polynomials for reasons to be explained below. The AIC value of a model is:

$$\mathrm{AIC}(M_i) = -2 \log L(M_i|\boldsymbol{y}) + 2k(M_i)$$

where $\log L(M_i|\boldsymbol{y})$ is the log likelihood given data $\boldsymbol{y}$, M_i is the i^{th} model and $k(M_i)$ is the number of parameters in M_i. The AIC takes the negative value of the log likelihood and penalize on the size of the model, thus the model with the minimum AIC value is selected.

Compared with BF, AIC and BIC do not depend on the choice of priors and penalize overfitting of the model, which makes the model selection more robust. The difference between AIC and BIC is the penalty level. In general, BIC is more stringent than AIC. Consequently, BIC tends to favor simpler models than AIC. From a practical perspective, AIC is advocated if the primary goal of modelling is for prediction, i.e., the model is built for effectively predict new outcomes. On the other hand, BIC tends to be advocated for descriptive purpose of the existing data [102]. The proposed model is used for predicting the stiffness loss along time. Thus, AIC is chosen for model selection.

The likelihood function of all unknown parameters is :

$$L\left(\boldsymbol{\beta}, \sigma_\theta^2, \sigma_f^2, \boldsymbol{U} \middle| \boldsymbol{\mathcal{F}}\right) = \int p\left(\boldsymbol{\mathcal{F}} \middle| \boldsymbol{\Theta}, \sigma_f^2, \boldsymbol{U}\right) \times p\left(\boldsymbol{\Theta} \middle| \boldsymbol{\beta}, \sigma_\theta^2\right) \mathrm{d}\boldsymbol{\Theta}$$

$$= \left[(2\pi)^{-\frac{\mathrm{N_f}}{2}} (2\pi)^{-\frac{1}{2}} (\sigma_\theta^2)^{-\frac{1}{2}}\right]^T \int \prod_{t=1}^{T} \exp\left[\frac{\left(\mathbf{F_t} - \boldsymbol{\eta}(\theta_t)\right)' \left(\mathbf{F_t} - \boldsymbol{\eta}(\theta_t)\right)}{-2\sigma_f^2}\right] \exp\left[\frac{(\theta_t - \boldsymbol{\beta^T x_t})^2}{-2\sigma_\theta^2}\right] \mathrm{d}\boldsymbol{\Theta}$$

$$= \left[(2\pi)^{-\frac{\mathrm{N_f}}{2}} (2\pi)^{-\frac{1}{2}} (\sigma_\theta^2)^{-\frac{1}{2}}\right]^T \prod_{t=1}^{T} \int \exp\left[\frac{\left(\mathbf{F_t} - \boldsymbol{\eta}(\theta_t)\right)' \left(\mathbf{F_t} - \boldsymbol{\eta}(\theta_t)\right)}{-2\sigma_f^2}\right] \exp\left[\frac{(\theta_t - \boldsymbol{\beta^T x_t})^2}{-2\sigma_\theta^2}\right] \mathrm{d}\theta_t$$

$$= \left[(2\pi)^{-\frac{\mathrm{N_f}}{2}} (2\pi)^{-\frac{1}{2}} (\sigma_\theta^2)^{-\frac{1}{2}}\right]^T \prod_{t=1}^{T} (2\pi)^{\frac{1}{2}} ({\sigma_{\mu_t}}^2)^{\frac{1}{2}} \times C_t = \left[(2\pi)^{-\frac{\mathrm{N_f}}{2}} (\sigma_\theta^2)^{-\frac{1}{2}} ({\sigma_{\mu_t}}^2)^{\frac{1}{2}}\right]^T \prod_{t=1}^{T} C_t$$

where $C_t = \exp\left[\frac{(\Sigma_{i=1}^{N_f} a_i^2 + c^2)\left(\Sigma_{i=1}^{N_f} b_i^2 + d^2\right) - \left(\Sigma_{i=1}^{N_f} a_i b_i + cd\right)^2}{-2\sigma_f^2 \sigma_\theta^2 (\Sigma_{i=1}^{N_f} b_i^2 + d^2)}\right]$. The log likelihood function is derived by taking the logarithm. We have

$$\log\left(L\left(\widetilde{\boldsymbol{\beta}}, \widetilde{\sigma_\theta^2}, \widetilde{\sigma_f^2}, \widetilde{\boldsymbol{U}} \middle| \boldsymbol{\mathcal{F}}\right)\right)$$

$$= T\left\{-\frac{\mathrm{N_f}}{2}\log(2\pi) - \frac{1}{2}\log\left(\widetilde{\sigma_\theta^2}\right) + \frac{1}{2}\log\left(\widetilde{\sigma_{\mu_t}^2}\right)\right\} + \sum_{t=1}^{T} \log\left(\widetilde{C_t}\right) \tag{4.6}$$

4.3 Numerical Study and Illustration

In this section, simulation studies are used first to validate the effectiveness of the proposed hierarchical model. Two scenarios are considered. In the first scenario, the underlying trend of the parameter θ_t is a second degree polynomial. The second scenario takes a beta function as the underlying damage growth curve. For the first case, the proposed model can perfectly recover evolving path, while for the second case, we will have a modeling error. AIC is used for model selection in both cases. The impact of the amount of data samples is also discussed.

In this numerical study, a fixed-fixed uniform beam with 60 elements is set up in FEM for calculating the natural frequencies. The beam has properties $E = 2.1 \times 10^8$ kPa, $L = 2.54$m, $I = 3.47 \times 10^{-8}$ m^4, $A = 6.45 \times 10^{-4}$ m^2 and $\rho = 0.013$ kg s^2/m. The stiffness loss is assumed to happen in the first element and the first three natural frequencies are used as the observed data, i.e., $N_f = 3$.

All natural frequencies decreases along the reduction in the weakness parameter θ_t, which is commonly observed and has been reported in many experimental studies [103]. In most cases, 5% decrease in natural frequencies can be referred to a severe damage in the structure [104]. According to the calculation by FEM, the 5% reduction in natural frequencies happens around $\theta = 0.4$. Thus, in the numerical study, we only consider the cases that the local stiffness of the first element is left above 40% level, i.e., $\theta_t \geq 0.4$. In other words, we are trying to recover the trend of the damage growth in an early stage before the damage becomes severe. We also treat $\theta = 0.4$ as the failure threshold of stiffness. Once the θ value drops to 0.4, the structure is considered as failed and not safe in the sense of stiffness reduction. The values of parameters in the hierarchical model are summarized in Table 4-2. The model takes the first three natural frequencies up to $t = 80$ as the temporal data input, where t is the time index or the load cycles. Without any knowledge on the

prior distribution parameters, values are assigned to make the priors non-informative to reduce the impact of prior choices.

Table 4-2. Summary of Parameters in the Model

	$\mathcal{MN}(\boldsymbol{b}, \sigma_\beta^2 \boldsymbol{I})$		$\mathcal{TG}(a_f, b_f)$		$\mathcal{TG}(a_\theta, b_\theta)$		$\mathcal{N}(\tau_i, \sigma_u^2)$	
N_f	σ_β^2	$\boldsymbol{b}$	a_f	b_f	a_θ	b_θ	τ_i	σ_u^2
3	10^{12}	0 0 0	1	1	1	1	0 0 0	10^{12}

4.3.1 Polynomials as Underlying Damage Growth Function

In the first scenario, the parameter θ_t follows a second degree polynomial $\gamma(t) = \boldsymbol{\beta^T x_t} = 1 - 9.375 \times 10^{-5} t^2$. It is assumed that there is no stiffness loss at the beginning and we only consider the case for $\theta_t \geq 0.4$ up to $t = 80$. The polynomial trend and the simulated data are summarized in Fig.4-1.

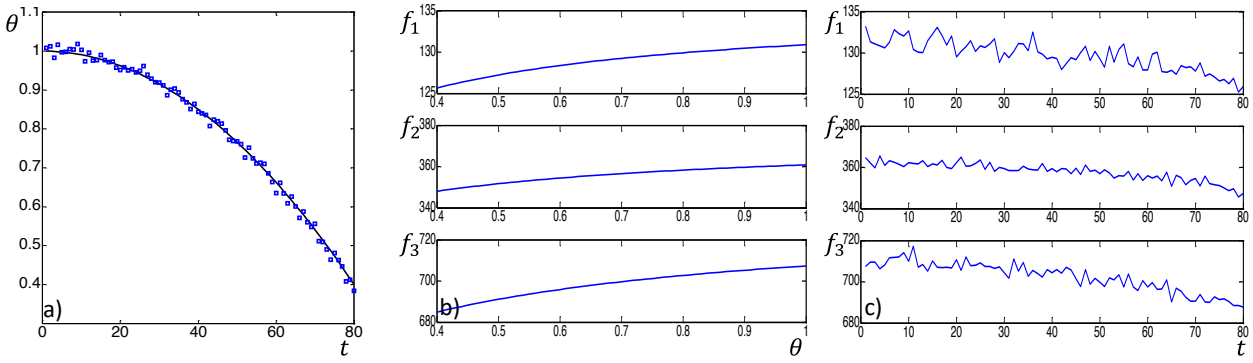

Fig 4-1 Summary plots of the first scenario. a) the polynomial trend of θ. b) the relationship between θ and f_i. c) the measurements of natural frequencies f_i

In Fig. 4-1 a), θ is plotted following the second degree polynomial. The squares in the same plot represent the θ perturbed by noise in Level 2 with $\sigma_\theta^2 = 0.001^2$. Since the variance is very small, the squares are nearly lying on $\gamma(t)$. In Fig. 4-1 b), the first three noise-free natural frequencies, i.e., f_1, f_2 and f_3, are plotted against θ. These natural frequencies are obtained from

the FEM. The reduction of natural frequencies is about 5%. In Fig. 3-1 c), white noise with $\sigma_f^2 = 1$ is added to the measurements of natural frequencies for an illustration purpose. In practice, natural frequencies can be measured accurately with noise around 0.1%. In the simulation, different levels of noise are added to the measurements of natural frequencies to test the effectiveness of the hierarchical model.

The perturbed natural frequencies in Fig. 4 -1 c) are the temporal data input of the hierarchical model. The Gibbs sampling algorithm runs $K = 60{,}000$ times and the first 30,000 iterations are considered as warm-up and are discarded. The samples that are generated in the warm-up period of the algorithm may follow different distributions before the convergence of the sampling process. In Fig. 4-2, plots for different values of T are presented. The detailed comparisons of parameters are summarized in Table 4-3.

In Fig. 4-2, T indicates the amount of the temporal data used in the model estimations. For example, $T = 10$ means only the first 10 observations of each natural frequency are being used in the estimation. The solid curve in each plot is the true underlying trend $\gamma(t)$ and the dotted curve is the estimated trend $\widetilde{\gamma(t)}$ with 95% confidence interval shown as dash curves. As the plots suggested, the estimation $\widetilde{\gamma(t)}$ recovers the underlying truth better for a larger T, i.e., for more data being used in the estimation process, which is not surprising.

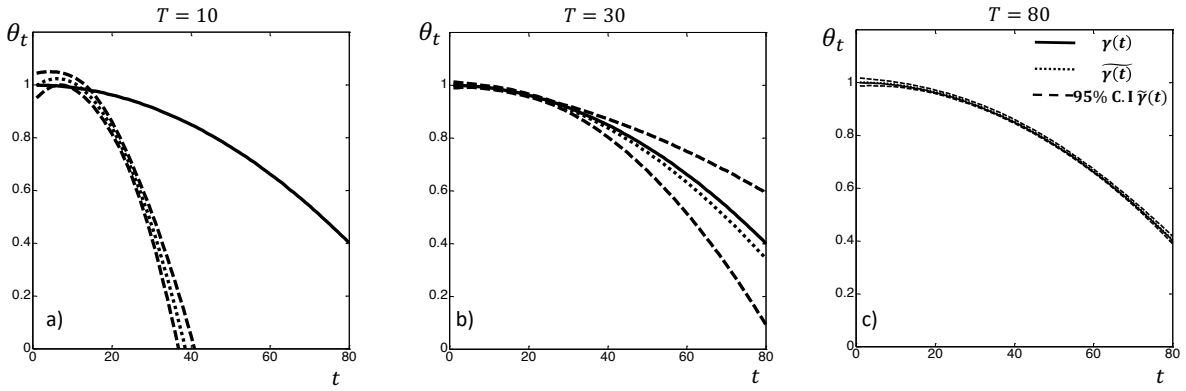

Fig 4-2 Plots of $\gamma(t)$ and $\widetilde{\gamma(t)}$ for different amount of input data. Solid curves are the underlying truth $\gamma(t)$ and dotted curves are the estimation $\widetilde{\gamma(t)}$ for different Ts with 95% confidence interval shown as dash curves.

Table 4-3. Comparison of coefficients estimation for different Ts

	$T = 10$	$T = 30$	$T = 80$
$\Delta\beta_1, s(\widetilde{\beta_1})$	$1.24 \times 10^{-2}, 1.56 \times 10^{-2}$	$3.8 \times 10^{-3}, 6.1 \times 10^{-3}$	$2.3 \times 10^{-3}, 4.0 \times 10^{-3}$
$\Delta\beta_2, s(\widetilde{\beta_2})$	$1.31 \times 10^{-2}, 6.8 \times 10^{-3}$	$1.9 \times 10^{-3}, 1.0 \times 10^{-3}$	$2.6 \times 10^{-4}, 2.1 \times 10^{-4}$
$\Delta\beta_3, s(\widetilde{\beta_3})$	$1.08 \times 10^{-3}, 5.7 \times 10^{-4}$	$2.3 \times 10^{-5}, 3.5 \times 10^{-5}$	$1.8 \times 10^{-5}, 2.8 \times 10^{-6}$
$u_1, s(\widetilde{u_1})$	128.15, 2.57	128.38, 2.13	123.94, 0.17
$u_2, s(\widetilde{u_2})$	398.41, 16.02	345.87, 3.77	342.66, 0.37
$u_3, s(\widetilde{u_3})$	744.65, 17.23	682.18, 8.01	674.73, 0.61
$\widetilde{\sigma_\theta^2}, s(\widetilde{\sigma_\theta^2})$	$1.0 \times 10^{-4}, 9.8 \times 10^{-7}$	$1.0 \times 10^{-4}, 1.0 \times 10^{-6}$	$1.0 \times 10^{-4}, 1.0 \times 10^{-6}$
$\widetilde{\sigma_f^2}, s(\widetilde{\sigma_f^2})$	$1.06 \times 10^{-2}, 1.0 \times 10^{-3}$	$1.1 \times 10^{-2}, 1.0 \times 10^{-3}$	$1.0 \times 10^{-2}, 9.2 \times 10^{-4}$
ME_T	1.77	0.017	0.001
d_T	46.2	2.7	0.23

In Table 4-3, the detailed comparisons of each parameter are presented for different values of T. $\Delta\beta_i = |\tilde{\beta}_i - \beta_i|$ is the absolute difference between the estimated coefficient $\widetilde{\beta}_i$ and the true value β_i. $s(\tilde{\beta}_i)$ is the standard derivation of the estimation $\tilde{\beta}_i$. $ME_T = \frac{1}{80}\sum_{t=1}^{80} |\gamma(t) - \widetilde{\gamma(t)}|$ is the mean absolute difference between $\gamma(t)$ and $\widetilde{\gamma(t)}$ up to $t = 80$ for a given T. Note that, ME_T computes the average difference of the entire curve, while $\widetilde{\gamma(t)}$ is only approximated by the observed data up to time T. d_T calculates the absolute difference between estimated failure time and the true

failure time if we use threshold $\theta = 0.4$, i.e., $d_T = |\widetilde{\gamma^{-1}(0.4)} - \gamma^{-1}(0.4)|$, where γ^{-1} is the inverse function of γ mapping from θ to t.

It can be seen that the estimations of β_is become more accurate with smaller standard derivations with larger sample size, which also leads to smaller values of ME_T and d_T. The estimations of the σ_θ^2 and σ_f^2 remain the same level of accuracy regardless the amount of observed data, since all the data shares the same σ_θ^2 and σ_f^2 along time and the Gibbs sampling is able to return the true values of the variation in the system.

In Table 3-4, we present the results of model selection using AIC for different degrees of polynomials. The values of AIC indicate the second degree polynomial should be selected among 4 different models, which is consistent with the underlying truth $\gamma(t)$, for both cases, $\sigma_f^2 = 1^2$ and $\sigma_f^2 = 0.01^2$.

Table 4-4. AIC Comparison for Different Models in First Scenario

	$\sigma_f^2 = 1^2$		$\sigma_f^2 = 0.01^2$	
Degree of Polynomials	Log-Likelihood	AIC	Log-Likelihood	AIC
1	-531.65	1067.30	-83.67	171.34
2	-525.42	<u>1056.84</u>	-78.18	<u>162.36</u>
3	-526.86	1061.72	-79.47	166.94
4	-527.23	1064.46	-80.05	170.10

4.3.2 Beta Function as Underlying Damage Growth Function

In the second scenario, we consider the case when the parameter θ_t follows a beta function. Again, we assume there is no stiffness loss at the beginning and we only consider the case for $\theta \geq 0.4$ up to $t = 80$. We summarize the second scenario in Fig. 3-3.

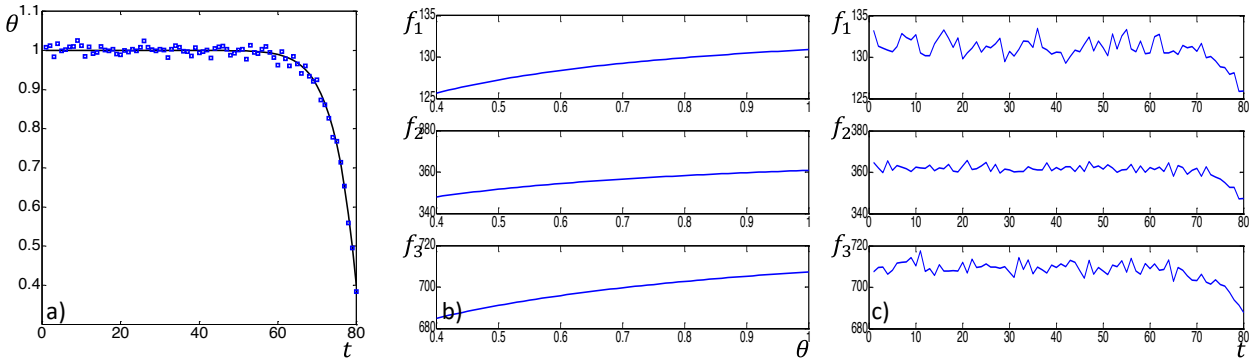

Fig 4-3 Summary plots of the second scenario. a) the beta function trend of θ. b) the relationship between θ and f_i. c) the measurements of natural frequencies f_i

Fig.4-3 b) is the same as Fig 4-1 b), since the two scenarios share the same relationship between nature frequencies and weakness parameter θ_t. The difference is the underlying trend of θ_t. In previous case, it is assumed the weakness grows gradually along time. However, in this example, we consider a non-uniform degradation rate, where θ_t decreases slowly at the beginning and drops rapidly at the end as shown in Fig.4-3 a). Such decreasing pattern is also reflected in the natural frequencies in Fig. 4-3c). The natural frequencies oscillate around the similar mean for a long time before they reduce quickly at the end. Plots for different values of T are presented in Fig. 4-4 and detailed comparisons of parameters are summarized in Table 4-5.

Similar results can be obtained from Fig. 3-4 and Table 3-5 compared with those in Fig. 4-2 and Table 3-3. It is obvious that more data will lead a better estimation of the underlying truth. The estimation $\tilde{\beta}_i s$ are reported in Table 3-5 instead of the $\Delta\beta_i$, since there is no true values of β_is in this case.

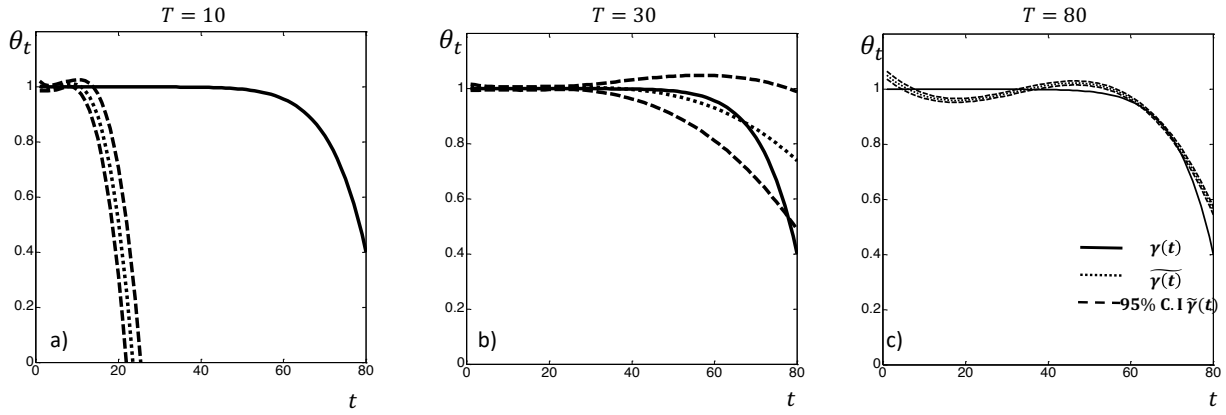

Fig 4-4 Plots of $\gamma(t)$ and $\widetilde{\gamma(t)}$ for different amount of input data. Solid curves are the underlying truth $\gamma(t)$ and dotted curves are the estimation $\widetilde{\gamma(t)}$ for different Ts with 95% confidence interval shown as dash curves.

Table 4-5. Comparison of coefficients estimation for different T

	$T = 10$	$T = 30$	$T = 80$
$\widetilde{\beta_1}, s(\widetilde{\beta_1})$	$1.2, 1.9 \times 10^{-2}$	$1.33, 6.8 \times 10^{-3}$	$1.13, 5.3 \times 10^{-3}$
$\widetilde{\beta_2}, s(\widetilde{\beta_2})$	$0.03, 1.5 \times 10^{-2}$	$-1.5 \times 10^{-3}, 1.4 \times 10^{-3}$	$-1.7 \times 10^{-2}, 5.1 \times 10^{-4}$
$\widetilde{\beta_3}, s(\widetilde{\beta_3})$	$-5.7 \times 10^{-4}, 3.1 \times 10^{-3}$	$0.97 \times 10^{-4}, 7.2 \times 10^{-5}$	$-3.9 \times 10^{-3}, 3.2 \times 10^{-5}$
$\widetilde{\beta_4}, s(\widetilde{\beta_4})$	$-5.2 \times 10^{-5}, 2.3 \times 10^{-4}$	$-1.4 \times 10^{-6}, 1.38 \times 10^{-6}$	$-6.2 \times 10^{-6}, 2.1 \times 10^{-7}$
$u_1, s(\widetilde{u_1})$	$129.9, 3.27$	$128.2, 1.83$	$124.7, 0.72$
$u_2, s(\widetilde{u_2})$	$397.0, 12.24$	$381.47, 4.25$	$344.07, 1.03$
$u_3, s(\widetilde{u_3})$	$746.6, 14.11$	$715.68, 6.8$	$677.20, 1.81$
$\widetilde{\sigma_\theta^2}, s(\widetilde{\sigma_\theta^2})$	$1.0 \times 10^{-4}, 1.0 \times 10^{-6}$	$1.0 \times 10^{-4}, 1.0 \times 10^{-6}$	$1.0 \times 10^{-4}, 1.1 \times 10^{-6}$
$\widetilde{\sigma_f^2}, s(\widetilde{\sigma_f^2})$	$0.009, 1.3 \times 10^{-3}$	$1.0 \times 10^{-2}, 7.5 \times 10^{-4}$	$6.3 \times 10^{-3}, 5.2 \times 10^{-4}$
ME_T	3.2	0.073	0.017
d_T	57.4	14.3	5.7

AIC comparison table is shown in Table 4-6. The 3rd degree polynomial is chosen for its minimum.

Table 4-6. AIC Comparison for Different Models in Second Scenario

	$\sigma_f^2 = 1^2$		$\sigma_f^2 = 0.01^2$	
Degree of Polynomials	Log-Likelihood	AIC	Log-Likelihood	AIC
1	-546.55	1097.1	-113.58	231.16
2	-538.17	1082.34	-93.46	192.92
3	-536.42	<u>1080.84</u>	-87.15	<u>182.3</u>
4	-535.91	1081.82	-86.24	182.48

4.3.3 Performance vs Amount of sample data

In the 1st and the 2nd scenarios, we investigate the effectiveness of the proposed model for different weakness growths. ME_T is used to compare the difference between $\gamma(t)$ and $\widetilde{\gamma(t)}$ under different amount of observed temporal data. In this section, we further explore the impact of the amount of data on the performance of the estimation procedure. We summarize the results in Fig. 4-5.

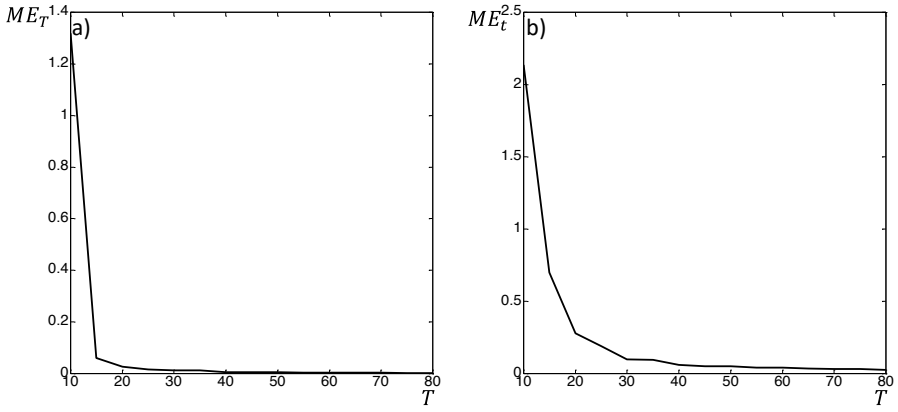

Fig 4-5 Plots of ME_T for different Ts in both polynomial and beta-function cases. a) Polynomial scenario, b) beta-function scenario.

It can be seen from Fig. 4-5 that mean error drops rapidly as data accumulating. Such feature enables us to recover or approximate the underlying damage growth accurately at an early stage before damages become severe. It is not surprised to observe that ME_T decrease even faster with smaller values in the polynomial case compared with that in the beta-function case, since the polynomial structure is adopted to estimate $\gamma(t)$ in the hierarchical model.

4.4 Case Study Using Experimental Modal Analysis Data

In this section, our proposed model is tested using real data obtained from experimental modal analysis. A fixed-fixed aluminum beam is the structure used in the experiment. The parameters of

the beam are summarized in Table 4-7. A FEM with 51 elements is set up according to the beam parameters.

Table 4-7. Parameters of the Beam Structure

Material	Young's Modulus	Density	Length	Width	Thickness
Aluminum	68.9Gpa	$2700\text{kg}/m^3$	510 mm	$19.05mm$	$4.76mm$

To simulate the stiffness loss, small masses are added on the middle of the beam and an accelerometer is used to along with modal hammer test to acquire the natural frequencies. Mathematically, adding small masses while keeping the stiffness unchanged has equivalent effect with respect to inducing stiffness reduction while keeping the mass unchanged. An illustration is shown in Fig. 4-6. Each small mass unit weights 2.9g, and a total of 9 masses are added. In Table 4-8, we report the measured natural frequencies under 9 different masses, the equivalent stiffness parameter θ and the assigned time t for each θ. The 0-mass case stands for the healthy condition of the beam. The relationship between natural frequencies and θ is approximated using linear function as shown in Fig. 4-7. The R-squared values indicate good explanations of the measured natural frequencies by linear functions. The values of u_i and v_i are labeled in each plot in Fig. 4-7. Note that, $\theta = 1.0$ is not considered in the plot, since the linear approximation can only be adopted for a small region. Thus, the degradation is assumed to start from $\theta = 0.46$ in the case study.

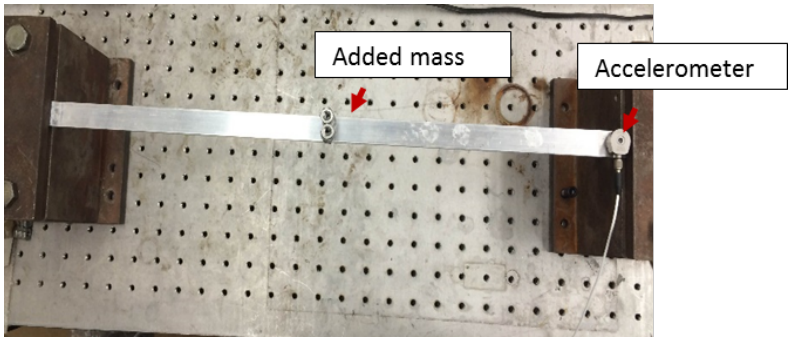

Fig 4-6 Masses are added on the middle of the beam to simulate the stiffness reduction with an accelerometer located near one end of the beam.

Table 4-8. Natural Frequencies under Different Masses with Stiffness Estimation (Hz)

#mass	f_1	f_2	f_3	θ	t
0	92	498	1219	1	
1	89.5	489	1200	0.46	0
2	87.5	481	1180	0.30	74
3	85	473	1161	0.22	75
4	83	466	1151	0.17	76
5	82	463	1145	0.14	77
6	80	457	1134	0.12	78
7	79	455	1123	0.11	79
8	76	448	1117	0.10	80

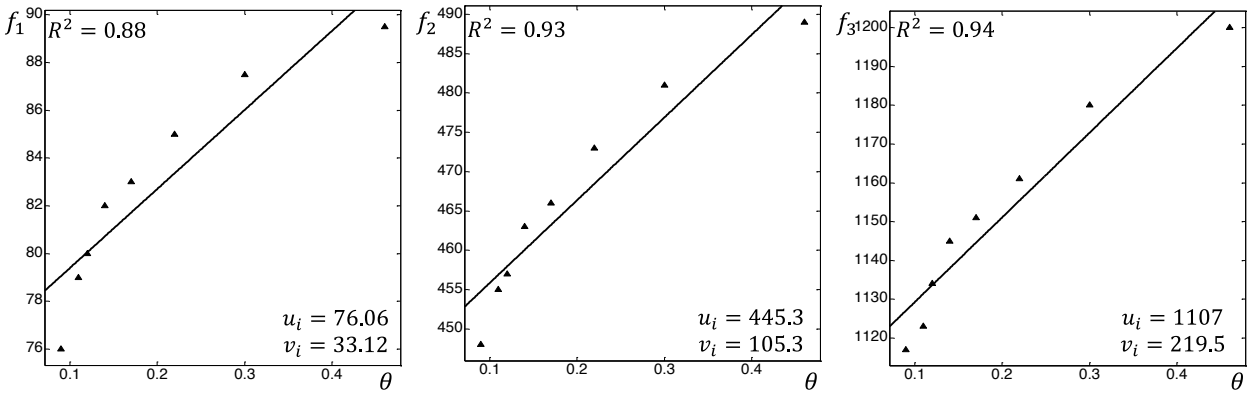

Fig 4-7 Linear approximations of the mappings from θ to f_is

In the experimental setting, the impact of the added masses on the natural frequency change can be viewed as equivalent to the impact caused by stiffness loss. Thus, the added masses are converted to the equivalent stiffness. The experimental data provide a static mapping between a

given stiffness loss and the measured natural frequency. In order to test and validate the proposed method for estimating the growth of the damage, we assigned time instances (last column in Table 4-8) to the experimental cases of different added masses. The time instances are assigned in such a way that the equivalent stiffness loss follows a beta-function trend. The proposed hierarchical model is adopted to approximate the damage growth using 2nd degree polynomial. $\theta = 0.1$ is used as the failure threshold of stiffness in the case study. The results are summarized in Fig. 3-8 and Table 3-9. It can be seen from both the plot and table that the proposed method can successfully approximate data using 2nd degree polynomial. The AIC comparison table is summarized in Table 4-10. The estimation of $\boldsymbol{\beta}$ has small standard deviation indicating a convergence of the Gibbs sampling algorithm. $u_i s$ and σ_θ^2 are estimated accurately. Note that, in the case study, $\sigma_\theta^2 = 1.0 \times 10^{-4}$ is used to represent the modelling error of θ.

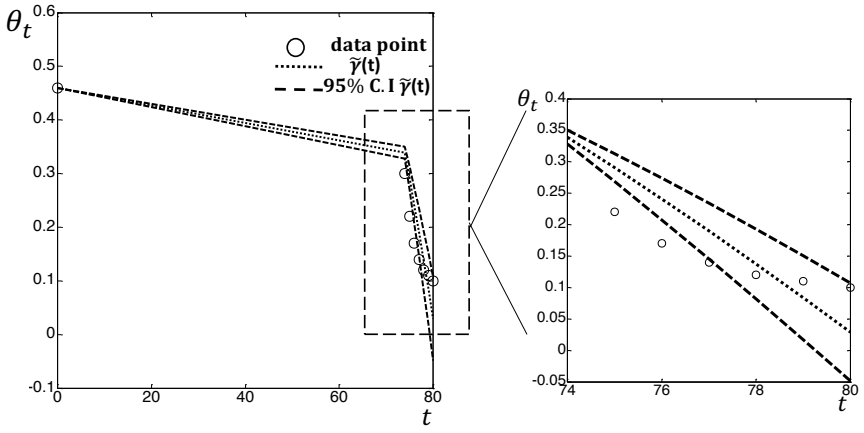

Fig 4-8 Plots of data θ and $\widetilde{\gamma(t)}$. θs are represented in circles and dotted curves are the estimation $\widetilde{\gamma(t)}$ with 95% confidence interval shown as dash curves.

Table 4-9. Coefficients estimation for real experimental data

$\widetilde{\beta_1}, s(\widetilde{\beta_1})$	$0.4604, 0.013$
$\widetilde{\beta_2}, s(\widetilde{\beta_2})$	$0.0448, 0.0025$
$\widetilde{\beta_3}, s(\widetilde{\beta_3})$	$-6.0 \times 10^{-4}, 3.2 \times 10^{-5}$
$u_1, s(\widetilde{u_1})$	$76.56, 0.47$
$u_2, s(\widetilde{u_2})$	$446.0, 0.73$
$u_3, s(\widetilde{u_3})$	$1108.3, 0.93$
$\widetilde{\sigma_\theta^2}, s(\widetilde{\sigma_\theta^2})$	$1.0 \times 10^{-4}, 1.0 \times 10^{-6}$
$\widetilde{\sigma_f^2}, s(\widetilde{\sigma_f^2})$	$0.72, 0.29$
ME_t	0.21
d_T	1.3

Table 4-10 AIC Comparison for Different Models in the Experimental Study

Degree of Polynomials	Log-Likelihood	AIC
1	-167.19	338.37
2	-135.11	276.21
3	-134.27	276.53
4	-135.32	280.64

4.5 Conclusion

This research presents a dynamic data-driven hierarchical Bayesian degradation model for estimating the evolving path of stiffness loss based on the measured natural frequencies. The model adopts a two level hierarchical structure. In the first level, the observed natural frequencies are assumed to be generated from a normal distribution with given stiffness. In the second level, the evolving path of stiffness is described using polynomial functions. The unknown parameters in the model are described by conditional posterior distribution in Bayesian framework and estimated by Gibbs sampling method. Numerical studies and results are used to validate the model for different evolving path of stiffness loss. The model performed efficiently in all cases.

One possible limitation of the proposed method is that the damage growth path is described by a polynomial function. Although polynomial function is flexible and relatively easy to use, it may cause some modeling errors when the underlying damage growth path cannot be well represented by a polynomial. For example, in practice, the system degradation often follows a beta-function like evolving path along time or load cycles. The system degradation state stays flat before rapid dropping at the end. The ability to detect the changing point quickly and accurately before the rapid drop can lead a better maintenance strategy, which enhances the safety of structures. However, such trend may not well described by a low order polynomial function. One idea is to use piecewise polynomial functions that consist of multiple low-order polynomials and change points as the damage growth model. Effective change detection technique will be needed.

5 Detecting Point Pattern of Multiple Line Segments Using Hough Transformation*

In Chapter 2, 3 and 4, quantitative analyses are applied on damage identifiability, bias reduction and damage prognosis in mechanical structures. In Chapter 5 and 6, two specific data analysis methods are adopted for spatial point pattern and functional data types, respectively.

In this chapter, we present a new method to detect the point patterns that consist of multiple line segments. The basic idea is that by using the Hough transformation, we convert the point pattern detection problem into a simple point matching problem. Compared with the existing point pattern matching methods, the proposed method does not require training data and is relatively easy to implement and compute. The details of the detection algorithm are presented and the parameter selection and performance evaluation of this method are investigated. Case studies are presented to validate the effectiveness of this method.

5.1 Introduction

A spatial point pattern (SPP) is a set of locations randomly distributed within a designated 2D or 3D space. SPP represents critical quality characteristics in various manufacturing processes. For example, surface defects on many products such as hot rolled steel bar and slab [105], semiconductor wafer [106], and glass [107] critically impact the product quality and process yield. In the emerging micro/nano processes, the particulate defects, which refer to nano/micro scale particles on the product surface that cause open or short circuit, is the important limiting factor of the process yield [108]. In composite fabrication, the distribution of the reinforced particles in the

* This chapter is based on the paper: **Liu, Yuhang**, and Shiyu Zhou. "Detecting Point Pattern of Multiple Line Segments Using Hough Transformation." IEEE Transactions on Semiconductor Manufacturing 28.1 (2015): 13-24.

base material directly impacts the mechanical property of the product [109,110]. Because SPP is a crucial indicator of quality in many processes, it is highly desirable to establish systematic quality control methodologies directly based on modeling and analysis of SPP data.

Generally, surface defects can be categorized into two types [111,112]: 1) globally scattered random defects, which are also known as background noise, caused by natural variation of manufacturing processes, and 2) locally clustered defects due to certain assignable causes. For example, the line segments on wafers can be caused by scratches during material handling and edge ring on wafer surface may be due to chemical stains. Since the assignable causes normally generate defects systematically, the detection of specific patterns of surface defects can often provide valuable information about the root causes. In the conventional quality control approaches, analysis of SPP data has been limited to high-level summary statistics. For example, statistical monitoring is realized by using various control charts based on the total count of defects on a surface area. For instance, c chart is often used to monitor the total number of defects with the underlying assumption that the number of defects follows Poisson distribution. An alarm will be raised when the number of defects falls outside the control limit [113, 114]. Control charts are conceptually intuitive and convenient to use, but they cannot provide information about specific spatial patterns of the defects since only the count data are used as monitoring statistics.

Beyond the statistical process control approaches, some techniques have been developed to detect the clustering and/or specific geometric patterns in the distribution of surface defects. These methods can be categorized into two types: (1) Spatial statistic based methods. In these methods, spatial statistic theory is adopted to model and analyze the nonrandom clustering patterns of defects. For example, Friedman et al [115] developed a model free estimation method to detect any clustering of surface defects on wafer. Jeong et al [116] developed an automatic identification

method based on spatial correlogram and dynamic time warping. The presence of clusters of defects can be detected in all of these methods. However, these methods are not designed to distinguish specific spatial patterns. In other words, they lack the ability to identify the geometric shape of a defect pattern. (2) Data mining methods. Neural networks, classification, fuzzy rule-based inferences and clustering methods are the most commonly used techniques in this category [117-126]. In these methods, the template pattern is learned from a training dataset and then the learned rules are used to detect the template pattern in the newly collected surface defects data. One issue of these methods is that they typically need a relatively large training dataset that contains the specific template patterns. However, such training datasets are often costly to obtain in practice. Zhou et al. [127] recently proposed a control chart method to detect the existence of simple geometric patterns in surface defects by using the conventional Hough Transform. However, that method requires that the patterns can be described by a simple analytic function, such as a line or circle. It lacks the ability to detect arbitrarily complex defect patterns.

In this chapter, we propose a new detection method to detect the existence of an arbitrary template consisting of multiple line segments in a SPP based on the Hough Transformation (HT). The HT is a commonly used feature extraction technique for analytical shapes, such as lines, circles and ellipses. The traditional HT method can only detect an object that can be described by an analytic equation. The Generalized Hough Transformation (GHT) is further developed based on the HT to detect arbitrary shapes [130]. The way the GHT works is to construct an R-table to store parameters (ϕ, r, α) of every edge point (X, Y) on an arbitrary pattern according to an arbitrarily selected reference point (X_c, Y_c), where ϕ is the tangent angle of the edge point, r is the length between (X, Y) and (X_c, Y_c), and α is the angle between the line segment with endpoints (X_c, Y_c) and (X, Y) and the horizontal line. Based on the R-table, the observed defect points can generate

votes to different potential reference locations (X_c, Y_c)s. The one with the highest vote will be determined as the detected reference location. Once the reference point is located, the position of the shape is determined and detected. The detailed algorithm of GHT can be found in [130]. Even though the GHT has played an important role in generalized shape detection since it was developed, it has the limitation for its substantial computational and storage requirements [129]. The limitation becomes acute when object orientation and scale have to be considered, since the rotation angle and the scaling factor are two more parameters that need to be decided by trying all possible situations. In general, the GHT needs to construct an R-table and go through a four dimensional matrix (two dimensions for the position of a reference point and the other two are referred to rotation and scaling) to detect the existence of the shape, which requires a large storage space and extensive computation for a 2D arbitrary shape. To overcome the limitation of the GHT, we propose a HT-based pattern detection technique without the construction of the R-table. Instead, for both of the given template and the observed defect point pattern, the HT is used to extract information about the Hough parameters, i.e., information about angles and distances for each line segment. Then the parameters from the template and that from the observed defect point pattern are compared and matched through two key steps: *angle matching* and *distance matching*. This method can also detect any transformation of the defect pattern, i.e., shifting, scaling and rotation from the position of the template. Compared to existing techniques, this method has the following characteristics: (*i*) It focuses on detecting a specific spatial pattern with a given template shape instead of only detecting the existence of defect clusters. (*ii*) The method has the capability to detect any irregular patterns consisting of multiple line segments. In this chapter, we also provide a design procedure for easy implementation and performance evaluation.

The rest of the chapter is organized as follows. Section 5.2 states the problem formulation and a brief introduction of the HT. A fundamental lemma is also presented in this section. Section 5.3 presents the detailed algorithm of the proposed method. Section 5.4 provides a performance evaluation. Section 5.5 presents a case study to illustrate and validate the method. Section 4.6 concludes the chapter.

5.2 Problem formulation and the basic matching principle

For the sake of clarity, we shall introduce some terminologies first. A *template* is an arbitrary shape formed by solid lines. An example of a 4-edged polygon template is presented in Figure 5-1(a). Note that a template is not necessarily to be a closed polygon. A *defect map* is a binary image consisting of randomly distributed black points (i.e., defects) on a white background. The points could be globally scattered random points, known as *background noise*, and locally clustered points, known as *defective regions*. In Figure 5-1(b) and 5-1(c), two defect maps corresponding to the 4-edeged template with different sizes and rotation angles are shown. Without loss of generality, we assume the points in the background noise and the defective region are completely random distributed with density parameter λ_0 and λ_1, respectively, where the density can be viewed as the number of points in a unit area. Furthermore, the width of the defective region is denoted as w as shown in Figure 4-1.

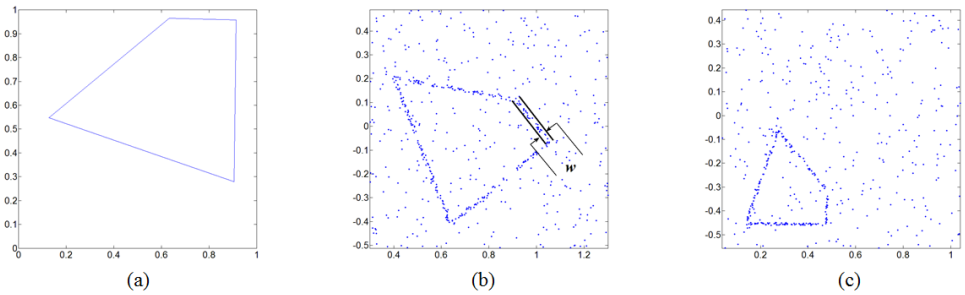

Fig 5-1 Examples of a template with two defect maps: (a) template; (b) defect map 1; (c) defect map 2.

The problem can be formulated as follows. Assume there is an n-edged template. We want to determine if there are defective regions in a defect map that are identical to the shape of the template with an arbitrary transformation $\boldsymbol{T}$ including rotation, scaling and shifting. Mathematically, the transformation of a point located at (x, y) can be described as:

$$\boldsymbol{T}(x,y) = \begin{bmatrix} 1 & 0 & \Delta x \\ 0 & 1 & \Delta y \\ 0 & 0 & 1 \end{bmatrix} \begin{bmatrix} s & 0 & 0 \\ 0 & s & 0 \\ 0 & 0 & 1 \end{bmatrix} \begin{bmatrix} cos\alpha & sin\alpha & 0 \\ -sin\alpha & cos\alpha & 0 \\ 0 & 0 & 1 \end{bmatrix} \begin{bmatrix} x \\ y \\ 1 \end{bmatrix},$$

where α is the rotation angle around the original point, s is the scaling factor and $v = (\Delta x, \Delta y)$ is the translation vector. Thus, $\boldsymbol{T}$ can be denoted as $\boldsymbol{T}_{\alpha,s,v}$. For example, the defective regions in Figure 5-1(b) and 1(c) are geometrically identical to the template in Figure 5-1(a) with different angle rotations and scaling factors. The problem is to detect the existence and to identify the best line segments in the defect map for a given template.

The basic idea of the proposed method is based on the Hough Transformation, since it has a strong capability in detecting lines. Therefore, we shall briefly introduce the principles of the HT for line detection in Section 5.2.1.

5.2.1 Introduction of the Hough Transformation for Line Detection

The Hough Transformation transfers a point from the physical domain to a curve in its parameters' domain. A line in $x-y$ plane can be uniquely defined by its distance ρ from the origin and the angle θ of its norm as

$$xcos\theta + ysin\theta = \rho \tag{5.1}$$

where θ is restricted within [0, π]. This parameterization maps every line in $x-y$ plane to a unique point in $\theta-\rho$ plane. For a point P_0 at (x_0, y_0), it will be mapped to the parameter plane as a sinusoidal curve defined as:

$$x_0cos\theta + y_0sin\theta = \rho.$$

Therefore, for points lying on the same line in $x-y$ plane, their corresponding sinusoidal curves in $\theta-\rho$ plane will pass through a common point, which is the parameters of the line. Based on this mapping relationship, a voting process can be designed to detect collinear points in $x-y$ plane, i.e., to detect any line patterns in the physical domain. In $\theta-\rho$ plane, the θ-axis and ρ-axis are divided into small intervals with equal length $\delta\theta$ and $\delta\rho$ respectively. Thus, the voting score of each pair of parameter (θ, ρ) is equivalent to the number of intersections of sinusoidal curves in each cell. A Hough matrix is then defined based on this voting process and *peak value* is defined as the highest voting score of each element in the matrix. In $x-y$ plane, the voting score of (θ, ρ) is equivalent to count how many points are in a strip with width $\delta\rho$, where the strip is located in

$x-y$ plane with a distance ρ and an angle θ. A strip in $x-y$ plane with parameters (θ,ρ) is called a *Hough strip* in this chapter. An example of this voting process is illustrated in Figure 4-2.

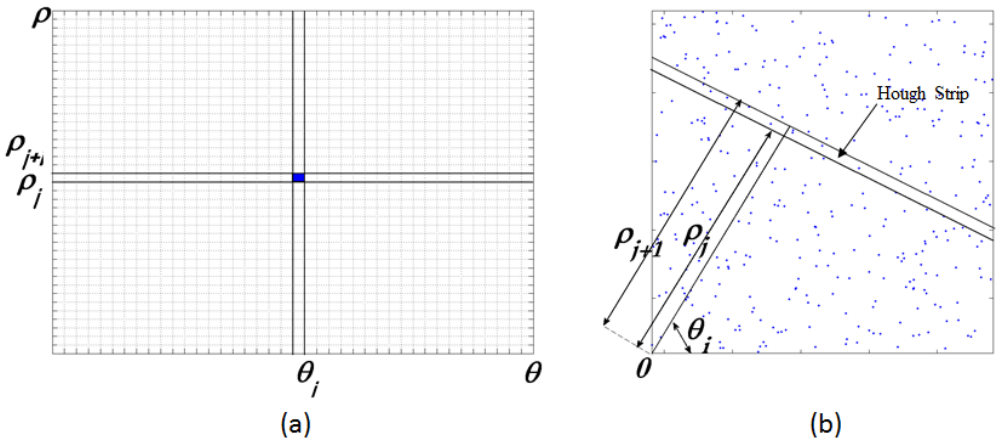

Fig 5-2 Line detection by the HT. (a) Accumulator array. (b) Defect map with a Hough strip

5.2.2 Basic principles for template matching based on the Hough transformation

Mathematically, the HT-based template matching problem can be stated as follows. Let $(\boldsymbol{\theta^0},\boldsymbol{\rho^0})$ be the set of parameters of the template with n line segments, where $\boldsymbol{\theta^0}=(\theta_1^0,\theta_2^0,\dots\theta_n^0)$ are the angle parameters and $\boldsymbol{\rho^0}=(\rho_1^0,\rho_2^0,\dots,\rho_n^0)$ are the distance parameters. Similarly, $(\boldsymbol{\theta},\boldsymbol{\rho})$ is the set of parameters of the detected line segments in the defect map, where $\boldsymbol{\theta}=(\theta_1,\theta_2,\dots\theta_m)$ are the angle parameters and $\boldsymbol{\rho}=(\rho_1,\rho_2,\dots,\rho_m)$ are the distance parameters. Without loss of generality, we assume $n\le m$. The problem is to find a subset $(\boldsymbol{\theta_s},\boldsymbol{\rho_s})$ of size n in $\boldsymbol{\theta}$ and $\boldsymbol{\rho}$ such that the parameters set $(\boldsymbol{\theta^0},\boldsymbol{\rho^0})$ can be matched under an arbitrary transformation $\boldsymbol{T}$. To solve this problem, we need the following lemma.

Lemma 5-1 . *A template under transformation* $\boldsymbol{T}_{\alpha,s,v}$ *will result in its HT parameters* $(\boldsymbol{\theta^0},\boldsymbol{\rho^0})$ *changing as follows:*

$$\begin{bmatrix} \theta_1^0 & \rho_1^0 \\ \vdots & \vdots \\ \theta_i^0 & \rho_i^0 \\ \vdots & \vdots \\ \theta_n^0 & \rho_n^0 \end{bmatrix} \xrightarrow{\boldsymbol{T}_{\alpha,s,v}} \begin{bmatrix} \theta_1^{0\prime} & \rho_1^{0\prime} \\ \vdots & \vdots \\ \theta_i^{0\prime} & \rho_i^{0\prime} \\ \vdots & \vdots \\ \theta_n^{0\prime} & \rho_n^{0\prime} \end{bmatrix}$$

where (L1) $\theta_i^{0\prime} = \theta_i^0 - \alpha$ *for a clockwise rotation, and (L2)* $\rho_i^{0\prime} = s\rho_i^0 + \Delta x \cos(\theta_i^{0\prime}) + \Delta y sin(\theta_i^{0\prime})$.

Proof.

Assume the rotation is in the clockwise direction. We define (x_i, y_i) is the intersection point between the orthogonal line of the ith edge going through the original point and the ith edge. Thus, we have

$$tan\theta_i^0 = y_i/x_i. \tag{5.2}$$

An α rotation will result in the position changing from (x_i, y_i) to (x_i', y_i'), i.e.:

$$\begin{bmatrix} x_i' \\ y_i' \end{bmatrix} = \begin{bmatrix} cos\alpha & sin\alpha \\ -sin\alpha & cos\alpha \end{bmatrix} \begin{bmatrix} x_i \\ y_i \end{bmatrix}$$

where $x_i' = x_i cos\alpha + y_i sin\alpha$ and $y_i' = -x_i sin\alpha + y_i cos\alpha$. We have

$$\tan(\theta_i^0 - \alpha) = \frac{\sin(\theta_i^0 - \alpha)}{\cos(\theta_i^0 - \alpha)} = \frac{\sin\theta_i^0 cos\alpha - cos\theta_i^0 sin\alpha}{\cos\theta_i^0 cos\alpha + sin\theta_i^0 sin\alpha}.$$

Multiply this equation by $\frac{x_i}{cos\theta_i^0}$, we have

$$\tan(\theta_i^0 - \alpha) = \frac{y_i'}{x_i'}.$$

For the case $x_i = 0$, i.e.,$\theta_i^0 = 90^\circ$, we have $x_i' = y_i sin\alpha$ and $y_i' = y_i cos\alpha$, equivalently, we have

$$\tan(90^\circ - \alpha) = \cot(\alpha) = \frac{y_i'}{x_i'}.$$

Note that, the scaling and shifting process have no impact on angles, i.e., $\tan(\theta_i^{0\prime}) = \frac{y_i'}{x_i'}$. Thus, (L1) is proved.

To see (L2), considering one line from Eq. (5.1), we have

$$y = -\frac{cos\theta}{sin\theta}x + \frac{\rho}{sin\theta}, \text{ for } \theta \neq 0.$$

The equation has the following structure:

$$y - \Delta y = -\frac{\cos(\theta+\alpha)}{\sin(\theta+\alpha)}(x - \Delta x) + \frac{s\rho}{sin(\theta+\alpha)} \tag{5.3}$$

after the transformation $\boldsymbol{T}$. Regroup Eq. (5.3), we get

$$y = -\frac{\cos(\theta+\alpha)}{sin(\theta+\alpha)}x + \frac{s\rho+\Delta x\cos(\theta+\alpha)+\Delta y sin(\theta+\alpha)}{sin(\theta+\alpha)}.$$

Thus, the new distance after transformation equals to:

$$\rho' = s\rho + \Delta x\cos(\theta+\alpha) + \Delta y sin(\theta+\alpha) = s\rho + \Delta x\cos(\theta') + \Delta y sin(\theta').$$

This derivation can be applied to every line of the template. Thus (L2) is proved. ■

Based on Lemma 5-1, two steps (i.e., the angle matching based on L1 and the distance matching based on L2) for the template matching can be designed as follows.

- *Angle Matching*

A subset of n elements satisfying (L1) needs to be selected from $\boldsymbol{\theta}$. One possible way is to try all possible rotation angles α. However, this method is time consuming. An easy result can be derived based on (L1), that is $\theta_i^0 - \theta_j^0 = \theta_i^{0\prime} - \theta_j^{0\prime},\ \forall i,j$. This invariant property can be used to

select sets of candidates in the parameter set $(\boldsymbol{\theta}, \boldsymbol{\rho})$. To achieve this, we first sort the template angles $\boldsymbol{\theta^0}$ as $\boldsymbol{\theta^0} = \left(\theta^{0(1)}, \theta^{0(2)}, \dots, \theta^{0(n)}\right)$, with $\theta^{0(1)} \leq \theta^{0(2)} \leq \cdots \leq \theta^{0(n)}$, and then an angle difference vector can be defined as $\boldsymbol{\Delta\theta^0} = \left(\theta^{0(1)} - \theta^{0(2)}, \theta^{0(2)} - \theta^{0(3)}, \dots, \theta^{0(n)} - \theta^{0(1)}\right)$. Further, we can obtain the differences between any two elements of $\boldsymbol{\theta}$ and put them in the matrix $\boldsymbol{M_\theta}$ as,

$$\boldsymbol{M_\theta} = \begin{bmatrix} 0 & \theta_1 - \theta_2 & \cdots & \theta_1 - \theta_m \\ \theta_2 - \theta_1 & \ddots & \cdots & \theta_2 - \theta_m \\ \vdots & \vdots & \ddots & \vdots \\ \theta_m - \theta_1 & \theta_m - \theta_2 & \cdots & 0 \end{bmatrix}_{m \times m}$$

Please note that we do not need to sort $\boldsymbol{\theta}$ to obtain $\boldsymbol{M_\theta}$. The jth candidate set $\boldsymbol{\theta^j} \subseteq \boldsymbol{\theta}$ is then defined as $\boldsymbol{\theta^j} = (\theta_1^j, \ \theta_2^j, \dots, \theta_n^j)$ with $\boldsymbol{\Delta\theta^0} - t_\theta \leq \boldsymbol{\Delta\theta^j} \leq \boldsymbol{\Delta\theta^0} + t_\theta$, where $\boldsymbol{\Delta\theta^j} = \left(\theta_1^j - \theta_2^j, \theta_2^j - \theta_3^j, \dots, \theta_n^j - \theta_1^j\right)$, θ_k^j is the kth element of $\boldsymbol{\theta^j}$, and t_θ is an allowance parameter. The reason of using an allowance parameter in the matching is that because of the random distribution of points, it is impossible for an exact match. The rotation angle of the jth set can be estimated as $\alpha^j = \frac{1}{n} \Sigma_{\mathrm{k}=1}^{n} (\theta_k^j - \theta_k^0)$. The details of the angle matching algorithm is presented as follows.

Table 5-1. Pseudocode for angle matching

Input : $\boldsymbol{\theta^0}, \boldsymbol{\theta}$
Sort $\boldsymbol{\theta^0}$ and $\boldsymbol{\theta}$ in an ascending order
Calculate $\boldsymbol{\Delta\theta^0}$
Calculate $\boldsymbol{M_{\theta_{m\times m}}}$ of $\boldsymbol{\theta}$
Define a $m \times m$ zero matrix $\boldsymbol{B}$
for i=1:m, j=1:m
  if $\boldsymbol{M_\theta}(i,j)$ in $[\boldsymbol{\Delta\theta^0} - t_\theta, \boldsymbol{\Delta\theta^0} + t_\theta]$
    $\boldsymbol{B}(i,j) = 1$
  end
end
for all nonzero element in $\boldsymbol{B}$
  if $\boldsymbol{B}(i_1,i_2) = \boldsymbol{B}(i_2,i_3) = \cdots = \boldsymbol{B}(i_n,i_1) = \mathbf{1}$ **for** $i_k \neq i_l$
    if $\boldsymbol{M_\theta}(i_k, i_{k+1})$ in $[\boldsymbol{\Delta\theta^0}(k) - t_\theta, \boldsymbol{\Delta\theta^0}(k) + t_\theta]$ **for** k=1,2,…,n-1
    A candidate set $(\theta_{i_1}, \theta_{i_2}, \ldots, \theta_{i_n})$ from $\boldsymbol{\theta}$ is determined
    A rotation angle α is calculated as $\alpha = \frac{1}{n}\,\Sigma_{\mathrm{k=1}}^{n}(\theta_{i_k} - \theta_k^0)$
    end
  end
end
return all candidate sets

After the angle matching procedure, if there is no candidate set being selected, we can claim the non-existence of the template pattern in the defect map. If multiple candidate sets survive the angle matching, then a checking based on the property (L2), called the distance matching, can be carried out as follows.

- *Distance Matching*

Assume the set $\boldsymbol{\theta^j}$ is selected after angle matching. The corresponding set of distance parameters is denoted as $\boldsymbol{\rho^j} = (\rho_1^j, \rho_2^j, \ldots, \rho_n^j)$, where (θ_k^j, ρ_k^j) is a pair of parameters of a detected line in the defect map by the HT. Because the rotation angle α of each candidate set has been estimated in the angle matching procedure, the other two transformation parameters s and $\boldsymbol{v}$ can

be determined for $\boldsymbol{T}_{\alpha,s,v}$ by minimizing the difference in the origin-line distance between the template and the detected line segments as:

$$d_j^* = min_{\boldsymbol{z^j}} \ ||\boldsymbol{\rho^j} - \boldsymbol{D^j z^j}|| \tag{5.4}$$

where $\boldsymbol{D^j} = \begin{bmatrix} \cos(\theta_1^{0\,j}) & sin\left(\theta_1^{0\,j}\right) & \rho_1^0 \\ \vdots & \vdots & \vdots \\ \cos(\theta_i^{0\,j}) & \sin\left(\theta_i^{0\,j}\right) & \rho_i^0 \\ \vdots & \vdots & \vdots \\ \cos(\theta_n^{0\,j}) & \sin\left(\theta_n^{0\,j}\right) & \rho_n^0 \end{bmatrix}$, $\boldsymbol{z}^j = \begin{bmatrix} \Delta x^j \\ \Delta y^j \\ s^j \end{bmatrix}$ and $\theta_i^{0\,j} = \theta_i^0 + \alpha^j$ for the jth candidate set. By (L2) in Lemma 5-1, the new distance $\rho_i^{0\,j}$ after $\boldsymbol{T}_{\alpha^j,s^j,\boldsymbol{v^j}}$ has the form $\rho_i^{0\,j} = s^j\rho_i^0 + \Delta x^j \cos\left(\theta_1^{0\,j}\right) + \Delta y^j sin(\theta_1^{0\,j})$ for all i. The goal is to find a transformation $\boldsymbol{T}_{\alpha^j,s^j,\boldsymbol{v^j}}$ that minimize the sum of squares of the differences, i.e., $\Sigma_i\left(\rho_i^j - \rho_i^{0\,j}\right)^2$, which has an equivalent matrix form as shown in Eq. (5.4).

Since this is a standard least square optimization problem, a closed form solution of the optimal $\boldsymbol{z^j}$ can be obtained by $\boldsymbol{z^j} = (\boldsymbol{D^{j^T}D^{j^{-1}}})\boldsymbol{D^{j^T}\rho^j}$, where $\boldsymbol{D^{j^T}}$ and $\boldsymbol{D^{j^{-1}}}$ are the transpose and inverse of the matrix $\boldsymbol{D^j}$ respectively**.** Thus, we can apply this optimization procedure to all the candidate sets that survive the angle matching and return the smallest value among all d_j^*s. If the returned value is smaller than a threshold t_ρ, then we claim a matching is found. Intuitively, the distance matching is to check the 'fitness' between the candidate shape and the template which is under scaling and shifting.

In this section, we presented basic principles of two critical matching steps, the angle matching and the distance matching. To successfully implement this pattern matching strategy,

several parameters such as t_θ, t_ρ need to be selected. The complete implementation of the algorithm and the parameters design issues are discussed in details in the following section.

5.3 **Parameter selection for the pattern matching algorithm**

In this section, we first present the entire flow of the pattern matching algorithm as shown in Figure 5-3. The template and the defect map are the inputs to the algorithm. For both images, The HT is used to detect the line segments in the template and the defect map. To apply the Hough transformation, we need to select the HT parameters $(\delta\theta, \delta\rho)$ for the template and the defect map, respectively. Because the template is formed by solid lines, it is straightforward to identify all the line segments in the template with parameters $(\boldsymbol{\theta}^0, \boldsymbol{\rho}^0)$. However, for the defect map, we need to establish a couple of thresholding parameters, i.e., $p_{\lambda_0}$and t_p, to detect the line segments. Particularly, if the highest voting score H_p in the Hough matrix is smaller than a threshold p_{λ_0}, we claim the defect map containing background noise only. To further reduce the influence of background noise, if the voting score of a cell at (θ, ρ) is higher than t_p, then we treat the corresponding line with parameters (θ, ρ) as a candidate. The parameters $(\boldsymbol{\theta}, \boldsymbol{\rho})$ formed by all the candidates will be used in the angle matching and the distance matching. As discussed in Section 5.2, thresholding parameters t_θ and t_ρ are used in these two matching steps. We claim the existence of the template pattern in the defect map if there are candidates surviving these matching steps.

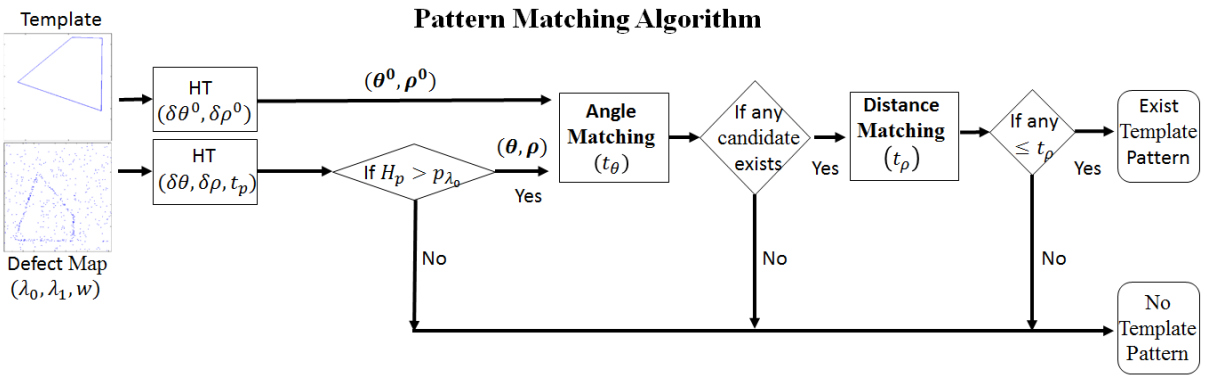

Fig 5-3 Pattern Matching Algorithm. The angle matching and the distance matching are sequentially applied to $(\boldsymbol{\theta}, \boldsymbol{\rho})$ and $(\boldsymbol{\theta^o}, \boldsymbol{\rho^o})$ after the HT.

Strategies of how to select the parameters used in the algorithm are discussed in details in the following subsections. For the illustration purposes, we will use a pattern matching example as shown in Figure 4-1 throughout the discussion. In this example, the template is a 4-edged polygon as shown in Figure 4-1(a) and two defect maps with parameters $(\lambda_0 = 500, \lambda_1 = 6000, w = 0.02)$ as shown in Figure 4-1(b,c), which contain the template with different rotation angles (30° and 50°) and scaling factors (0.8 and 0.5), respectively.

5.3.1 Selection of the parameters ($\delta\theta$ and $\delta\rho$) for the Hough transformation

Because the template is given in the form of solid line segments without background noise, it is straightforward to choose the HT parameters for the template and these parameters will not significantly impact on the resulting detected line segments in the template. Thus, we will focus on the HT parameter selection for the line detection in the defect map. The selection of the HT parameters for the defect map needs more consideration for the following reasons: (1) If $\delta\theta$ and $\delta\rho$ are too small, then the Hough matrix will be large, which will in turn lead to a large matrix $\boldsymbol{M_{\theta_{m\times m}}}$ in the angle matching step. Roughly, the angle matching step needs $\binom{m}{n}$ calculations to detect all possible candidate sets. When m is getting larger, the computational cost increases

dramatically. (2) On the other hand, if $\delta\theta$ and $\delta\rho$ are too large, then the resolution of the line detection will be low and a misdetection of the template may happen.

It is very difficult, if not impossible, to identify the optimal values for $\delta\theta$ and $\delta\rho$ for general line detection scenarios. Here we provide some heuristic guidelines on the HT parameters selection. Intuitively, if a Hough strip (as illustrated in Figure 4-2(b)) that corresponds to a single cell in Hough domain passes the defective region and overlaps with the defective region in the largest possible way, then the value difference in the corresponding cells between the case with the defective region and that without the defective region will be large. As a result, the defective region will be easier to detect. Furthermore, it can be expected that the orientation of a Hough strip that has a large overlapping region with the defective region will be aligned better with the defective region than that of partially overlapped Hough strips. As a result, the orientation of the defect region can be detected more accurately, which will in turn lead to more accurate detection. In other words, for the defect pattern that indeed matches with the template, then we will have higher detection rate; while for a defect pattern that does not match with the template, it becomes easier for us to reject. The parameters ($\delta\theta$ and $\delta\rho$) determine all the possible locations and orientations of the Hough strips. Based on the above intuition and noting that the defective region is completely randomly distributed, we can obtain the approximated upper bounds for $\delta\theta$ and $\delta\rho$.

We define a Hough strip is fully overlapped with a defective region if the upper and lower bounds of the strip are crossing the short edges of the rectangular defective region. The extreme of the fully overlapped case is when a strip passes through the corners of a defective region as shown in Figure 4-4(a). We define the angle between the strip and the defective region in this extreme case as β (a geometry illustration in Figure 4-4(a)), and we can obtain $\beta =$

$arcsin\frac{w}{\sqrt{w^2+l^2}} - arcsin\frac{\delta\rho}{\sqrt{w^2+l^2}}$. Note that the angle between the defective region and any fully overlapped Hough strips is no larger than β. With this angle β, we can identify the parameters $\delta\rho, \delta\theta$ such that at least one Hough strip is fully overlapped with a given defective region that is arbitrarily located. First note that, for a given $\delta\theta$, the minimal absolute difference between the exact angle value θ of a defective region and the quantization value $k\delta\theta$ can be as large as $\frac{\delta\theta}{2}$, for integer $k = 0,1,2$ ..., i.e.,

$$\min_k |\theta - k\delta\theta| \leq \frac{\delta\theta}{2},$$

since $\theta \in [k\delta\theta, (k+1)\delta\theta]$ for a value k, the minimal value $|\theta - k\delta\theta|$ is no larger than $\frac{\delta\theta}{2}$. Define the optimal k value to be k^*.

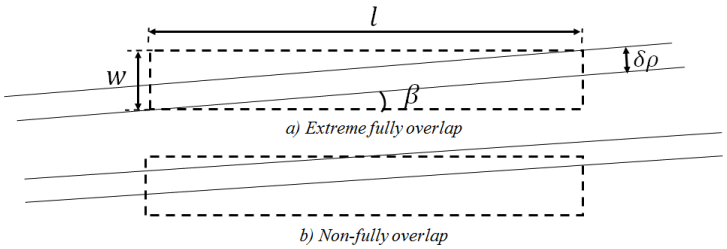

Fig 5-4 Examples of a fully overlapped strip and a non-fully overlapped strip. β is the angle between a Hough strip and the defective region in the extreme case as shown in (a).

Then we have the following Lemma.

Lemma 5-2. For a defective region with length l and width w and its centerline is arbitrarily located at (ρ, θ), a sufficient condition to have a fully overlapped Hough strip with the defective region is :

$$\delta\rho \leq \frac{w\cos(|\theta - k^*\delta\theta|) - l\sin(|\theta - k^*\delta\theta|)}{2}. \quad (5.5)$$

Proof.

The proof is illustrated directly by the Figure 4-5. If two parallel lines which have the minimal absolute angle difference, i.e., $|\theta - k^*\delta\theta|$ with the defective region, are crossing the diagonal corners of the defective region, then the distance between the two parallel lines equals to $(w - l \cdot tan(|\theta - k^* \cdot \delta\theta|)\cos(|\theta - k^* \cdot \delta\theta|) = w \cdot cos(|\theta - k^* \cdot \delta\theta|) - l \cdot sin(|\theta - k^* \cdot \delta\theta|)$ as shown in Figure 5-5. Thus, if $\delta\rho$ is no larger than half of the distance, then there will be at least one Hough strip which is fully overlapped with this defective region regardless the position of the defective region. ■

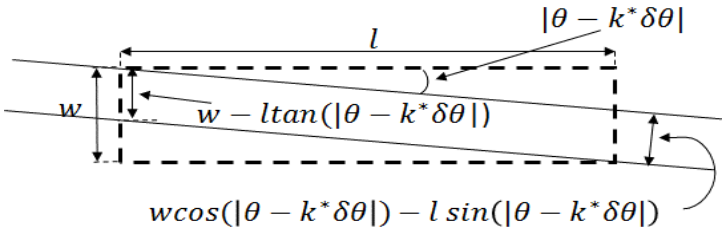

Fig 5-5 Illustration of Lemma 4-2. $\delta\rho$ needs to be smaller than half of the distance between the two parallel lines as shown in the figure.

Remarks

(1)The function $w \cdot cos(x) - l \cdot sin(x)$ is a decreasing function both of x in range $[0, \frac{\delta\theta}{2}]$ and of l, so we can chose $\delta\rho$ as:

$$\delta\rho \leq \frac{wcos\left(\frac{\delta\theta}{2}\right) - \max_i\{l_i\}sin\left(\frac{\delta\theta}{2}\right)}{2},$$

where i is the index of the defective regions in the template. This will guarantee that we will have fully overlapped Hough strips for any of the defective regions in the template.

(2)$|\theta - k^*\delta\theta| \leq \beta$. By the inequality in (4.5), $\delta\rho$ is smaller than half of the distance between the two parallel lines. Thus, the angle $|\theta - k^*\delta\theta|$ between the defective region and its fully overlapped Hough strip with width $\delta\rho$ is not extremely fully overlapped.

(3)We can see that $\lim_{\delta\theta\to 0}|\theta - k^*\delta\theta| = 0$. This means that the sufficient condition of a fully overlapped strip with the defective region becomes $\delta\rho \leq \frac{\mathrm{w}}{2}$ as $\delta\theta \to 0$. This is consistent with the intuitive observation. Note if $\delta\theta$ is chosen to be 1°, the absolute angle difference $|\theta - k^*\delta\theta|$ will be no larger than 0.5°. In most practical cases, this is regarded as a small angle. Thus, we can approximately select $\delta\rho \leq \frac{w}{2}$ for the parameter $\delta\rho$ when $\delta\theta \leq 1^{\circ}$. In the example and the following simulation discussion, we select $\delta\theta = 1^{\circ}$ and $\delta\rho = w/2$.

5.3.2 **Selection of the thresholds ($p_{\lambda_0}$and t_p) for line detections in defect map**

As described at the beginning of this section, we employed a two-step procedure in order to select a candidate set of detected lines for the following angle matching and distance matching. In the first step, we check if there are lines in the defect map. To achieve this, we follow the common practice in the HT-based line detection approach [121]: we check if the peak value H_p of the Hough matrix of the defect map is larger than a threshold value p_{λ_0}. If not, then we claim that the voting scores in the Hough matrix are due to the background noise and there are no lines in the map. The value of p_{λ_0} can be identified as follows. We denote H_0 as the peak value of the Hough matrix when there is only background noise with parameter λ_0 in the defect map. It is clear that H_0 is a random variable. The distribution of H_0 can be obtained through Monte Carlo simulations. With the distribution of H_0, we can determine p_{λ_0} as the αth quantile of H_0, i.e., $P(H_0 \geq p_{\lambda_0}) = 1 - \alpha$. Typically we select α as a small number, say 0.1.

In the second step, we check the number of lines in the defect map. It is obvious that the long defective region is easier to be detected compared to the short ones because the long defective region corresponds to a large voting score in the Hough matrix. Thus, in this step, we should make sure that the short defective regions in the template can be detected with high probability. To achieve this, we establish a threshold value t_p such that if $h_{\theta_i,\rho_i} \geq t_p$, then we say the line with parameters (θ_i, ρ_i) exists in the defective map. Here (θ_i, ρ_i) is the ith pair of parameters after the HT and h_{θ_i,ρ_i} is the voting score of (θ_i, ρ_i) in the Hough matrix. The value of t_p is determined in a relative sense as $t_p = rH_p$, where H_p is the peak value of the Hough matrix and r is a constant. The value of r is selected such that the shortest line in the template can be detected with a high probability. Specifically, assume (θ_i, ρ_i) and (θ_j, ρ_j) are the parameters for the longest and shortest line segment in the template, respectively and h_{θ_i,ρ_i} and h_{θ_j,ρ_j} are the Poisson random variables that correspond to the voting scores in the Hough matrix. Then r can be selected as

$$r = sup\{c: P\left(h_{\theta_j,\rho_j} > c \cdot h_{\theta_i,\rho_i}\right) \geq 0.9\}. \tag{5.6}$$

Based on Eq. (5.6) and setting $t_p = r \cdot H_p$, we will have at least 90% chance to detect the shortest line segment in the template. The probability function in Eq. (4.6) does not have a closed form. However, a straightforward Monte Carlo simulation can be used to identify the value of c. Specifically, we can generate random values through Monte Carlo simulation for h_{θ_i,ρ_i} and h_{θ_j,ρ_j} according to their Poisson distribution parameters $l_i sw\lambda_1$ and $l_j sw\lambda_1$ respectively, and calculate the ratio $h_{\theta_j,\rho_j}/h_{\theta_i,\rho_i}$, here s is the scaling factor. A distribution plot of the ratio can be achieved and c can be determined from the plot. Please note that, since $\lambda_1 \gg \lambda_0$, the background noise has little effect on the final result of r.

Considering the example given in Figure 4-1. The empirical probability mass function of H_0 is obtained through 1000 runs of Monte Carlo simulation and is given in Figure 5-6(a). Based on this probability function, we can find the 0.1th quantile value of H_0 to be 13. Furthermore, the function of $P\left(h_{\theta_j,\rho_j} > c \cdot h_{\theta_i,\rho_i}\right)$ is obtained through 1000 runs of Monte Carlo simulation. From this function, we can determine r to be 0.26. Finally, we can determine $p_{\lambda_0} = 13$ and $t_p = 0.26 \cdot H_p$ for this example problem.

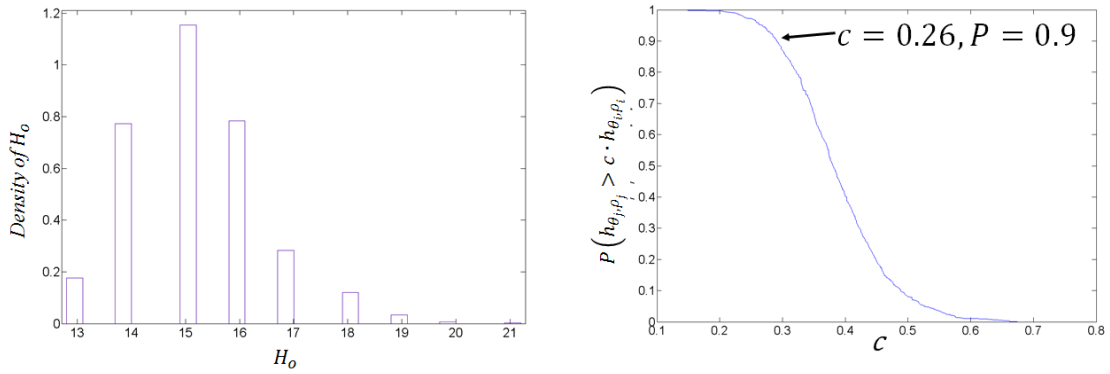

(a) (b)

Fig 5-6 (a) Density diagram of H_0. (b) Distribution plot of $P\left(h_{\theta_j,\rho_j} > c \cdot h_{\theta_i,\rho_i}\right)$.

5.3.3 Selection of t_θ and t_ρ in the angle and distance matching

Because the defect map is formed by random points, it is impossible to have a perfect match in the angle and distance parameters between the template and the observed defect map. Thus, allowances are needed for the angle and distance matching.

The following lemma can be used to determine the threshold of the allowance t_θ in the angle matching.

Lemma 5-3. *For two defective regions with centerlines located at* (θ_1, ρ_1) *and* (θ_2, ρ_2), *and any two Hough strips that are fully overlapped with the two defective regions, respectively, the angle difference between these two Hough strips is no larger than:*

$$(\theta_1 - \theta_2) + 2\beta \tag{5.7}$$

where $\beta = arcsin\frac{w}{\sqrt{w^2+l^2}} - arcsin\frac{\delta\rho}{\sqrt{w^2+l^2}}$ *is the angle between the shorter defective region and the fully overlapped strip in the extreme case.*

Proof.

Without loss of generality, we can assume the two Hough strips have the angle values of $\theta_1 + |\theta_1 - k_1^*\delta\theta|$ and $\theta_2 - |\theta_2 - k_2^*\delta\theta|$, respectively. We have

$$(\theta_1 + |\theta_1 - k_1^*\delta\theta|) - (\theta_2 - |\theta_2 - k_2^*\delta\theta|) = (\theta_1 - \theta_2) + (|\theta_1 - k_1^*\delta\theta| + |\theta_2 - k_2^*\delta\theta|),$$

with the term $|\theta_1 - k_1^*\delta\theta| + |\theta_2 - k_2^*\delta\theta|$:

$$|\theta_1 - k_1^*\delta\theta| + |\theta_2 - k_2^*\delta\theta| \leq 2\max\{\,|\theta_1 - k_1^*\delta\theta|, |\theta_2 - k_2^*\delta\theta|\,\}.$$

However, from the remark (2) of Lemma 5-2, we know $\max\{\,|\theta_1 - k_1^*\delta\theta|, |\theta_2 - k_2^*\delta\theta|\,\} \leq \beta$. Thus, the lemma is proved. ■

From Lemma 5-3, we can see that 2β is likely the largest difference between the true angle difference and the detected angle difference of two defective regions, because intuitively the Hough strips that are fully overlapped with the defective regions are likely to be detected. Thus, for a template with multiple defective regions, we can select the threshold $t_\theta = 2\max_i \beta_i$, where i is the index of defective regions.

It is quite difficult to derive the threshold t_ρ in the distance matching. Because the distance is measured from the original point, the difference between the true distance and the detected distance of a defective region is related with the location of the defective region in the defect map. For the sake of simplicity, here we ignore the errors in the detected angle of the defective region. Thus, for a defective region, the maximum difference between the true distance and the detected distance can be as large as $w/2$. Further, since t_ρ is the threshold for the accumulated distance detection error for all the defective regions in the template, we can select $t_\rho = \sqrt{n}w/2$, where n is the number of defective regions in the template.

Note that t_θ depends on the length of edges in the template and t_ρ depends on the number of edges and the width of the defective region. For a template with the larger number of edges, its threshold t_ρ is larger. In the example in Figure 4-1, we select the threshold $t_\theta = 6^\circ$ and $t_\rho = 0.02$ according to the above guidelines.

In the example in Figure 4-1(b,c), the two defect maps have the same densities $\lambda_1 = 6000, \lambda_2 = 500$ and the common width $w = 0.02$ with different rotation angles $\alpha = 30^\circ, 50^\circ$ and scaling factors $s = 0.8, 0.5$, respectively. The HT parameters used in the detection are $\delta\theta = 1^\circ, \delta\rho = \frac{w}{2} = 0.01, t_p = 11, p_{\lambda_0} = 13, t_\theta = 6^\circ$ and $t_\rho = 0.02$. The numerical results are shown in the following table and the final graphical detections are in Figure 5-7.

Table 5-2. Numerical results of the example.

	d^*	α^*	s^*	α	s
(b)	0.016	30	0.79	30	0.8
(c)	0.017	52	0.62	50	0.5

d^* and s^* are the minimal distance difference and the optimal scaling factor calculated in the distance matching process. α^* is the rotation angle calculated in the angle matching process. The results validate the accurate detection of the pattern detection algorithm. In the next section, a performance evaluation is presented.

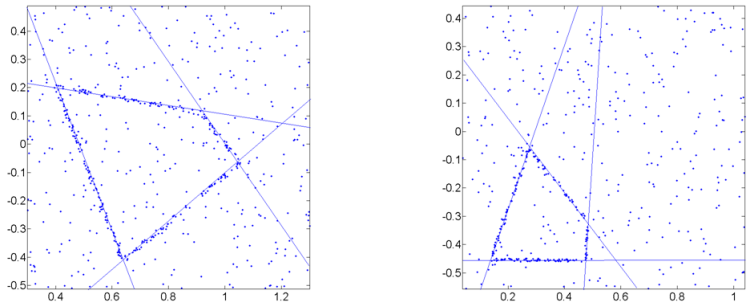

Fig 5-7 Detection results of the examples in Figure 4-1.

5.4 Numerical Study and Performance Evaluation

In this section, we first present the performance evaluation results for the proposed point pattern detection method. For a pattern detection algorithm, the performance is often evaluated through Type I error probability and the Type II error probability, where Type I error probability refers to the false alarms (i.e., the probability that we claim the existence of a template pattern in the defect map when in fact the template pattern does not exist) and Type II error probability refers to the misdetection (i.e., the probability that we do not detect the truly existing template pattern in the defect map). Besides Type I and Type II error probabilities, detection power is also used to evaluate the performance of a pattern detection algorithm. The detection power refers to the probability that we detect a truly existing template in the defect map. Clearly, detection power is actually $1 - Type$ II error probability.

The factors that influence the detection performance and the comparison between the proposed method and the GHT on the detection of arbitrary shapes will also be discussed in this section.

5.4.1 Type I error and the detection power of the proposed method

Due to the complexity of the algorithm and the random distribution of the template and defect map, it is intractable to establish closed form expression of evaluation indices for a given scenario. Here we use an extensive numerical study to illustrate the performance of the algorithms and the impacts of various factors on the performance. In the numerical study, the Type I error and the detection power of the algorithm are investigated for the various templates with $n = 4,6,8$ edges and with scaling factor $s = 0.5, 0.8$ and different$\lambda_0 s, \lambda_1 s$. The detailed simulation procedure is showed below:

Table 5-3. Numerical study procedure for performance evaluation

(1) Input**:** n $(4\ or\ 6\ or\ 8)$, s $(0.5\ or\ 0.8)$, λ_0, λ_1, $w = 0.02$
(2) Randomly generate an n-edged template in a 1×1 unit square with the shortest edge no smaller than 0.3. Save length l of each edge. Save it as the template image.
(3) Randomly generate a rotation angle : α
(4) Rotate the template with α and scale it by s
(5) Generate random points in a rectangle with size $w \times l_i \times s$ along each edge of the template from step (4). The points are uniformly distributed in each rectangle and the number of points are following Poisson distribution with parameter $\lambda_1 \times w \times l_i \times s$.
(6) Background noise is added to the unit square with the number of points following Poisson distribution with parameter λ_0. Remove solid lines and save it as the defect map.
(7) Run **Pattern Matching Algorithm**
(8) Estimate the detection power and the Type I error probability
For detection power:
Repeat (2) – (7) $M = 1000$ times
Count the number of detection of existence of template, denoted as m
Report estimated detection power as m/M
For Type I error probability:

Modify Step (2) as $(2')$, where two random templates are generated, one used to generate defect regions in the defect map and one used in the pattern detection algorithm as the template pattern
Repeat $(2')$ – (7) M times and count the number of detection of existence of template as m
Report Type I error probability as m/M

One point we would like to mention that in Step (2), we require the minimum length of the edges of the template to be at least 0.3. The reason is that if the edge length is too small, it is difficult for the Hough transformation to detect that edge at the first place. In simulation study, the template and the input parameters can be designed easily. In practice, the template shape and the values of $l, w, \lambda_1 \; and \; \lambda_0$ can be decided by looking at typical defect patterns in the historical data or by physical analysis of the fault modes based on engineering experiences. For example, it is known that some optical system errors in a semiconductor manufacturing process will cause specific defect patterns on a wafer. Another example is that chattering in a metal cutting process will leave specific waviness patterns on the finished workpiece. So with physical understanding of the fault modes of a process, the template pattern could be established. Furthermore, the values of $l, w, \lambda_1 \; and \; \lambda_0$ can also be obtained by looking at the historical data. λ_1 and λ_0 are the densities of the defective regions and the background noise. They can be calculated by using the number of defect points divided by the area of defective regions and the entire defect map respectively. For l and w, they can be measured from the template identified from the historical data.

Through extensive simulation, we can obtain the following Type I error probability and the detection power for various parameter combinations.

Table 5-4. Type I error and the detection power

		n=4(s=0.8/s=0.5)		n=6(s=0.8/s=0.5)		n=8(s=0.8/s=0.5)	
λ1	λ0	Power	Type I error	Power	Type I error	Power	Type I error
6000	500	93.18%/92.17%	0.4%/0.7%	88.42%/83.34%	0.7%/0.4%	79.45%/68.10%	0.2%/0.5%
6000	100	93.62%/91.14%	0.2%/0.4%	90.28%/87.17%	0.3%/0.4%	83.24%/75.31%	0.3%/0.1%
3000	250	86.08%/76.25%	0.5%/0.3%	70.12%/54.38%	0.2%/0.7%	53.22%/36.58%	0.4%/0.4%
3000	500	78.75%/59.34%	0.3%/0.2%	65.23%/42.15%	0.8%/0.3%	45.12%/28.50%	0.9%/0.2%
1500	125	58.47%/41.91%	0.4%/0.6%	42.18%/27.56%	1.2%/0.8%	21.50%/11.12%	0.5%/0.7%

From these results, we have the following remarks.

(1) Regarding the detection power

It is not surprising that the detection power is directly related with the difference between λ_1 and λ_0. The larger the difference, the higher the power. This is certainly expected because the higher value of the rate λ_1, the more significant contrast between the defective region and the background noise. Figure 4-8 includes several defect maps with different $\lambda_0 s$ and λ_1s, which clearly illustrates the above point. Besides λ_0 and λ_1, the detection power is also influenced by the number of edges in the template and the scaling factor. As the number of edges increases, the detection power decreases. This is not surprising because if p_i is the probability of detecting the ith edge of the template, then $\prod_i p_i$ is roughly the probability to detect all the edges of the template. As n gets larger, this probability gets smaller. The detection power increases as the scaling factor s gets larger. The reason is that in general, a larger defective region is easier to be detected.

(2) Regarding the Type I error probability

The numerical study results show that the Type I error probability is quite small for all cases. We investigate the numerical results in more detail and find that about 90% of the defect maps that do not contain the template are rejected at the angle matching step, i.e., there are no angles in the detected $\boldsymbol{\theta}$ parameters that can form a vector containing n components such that $\boldsymbol{\Delta\theta} \in$

$[\boldsymbol{\Delta\theta^0} - t_\theta, \boldsymbol{\Delta\theta^0} + t_\theta]$. For any candidates that pass the angle matching step, the distance matching is also an effective step to differentiate the shape of the defective regions and the template pattern. For example, Figure 4-9 shows a case that a defect map passes the angle matching step but fails at the distance matching step. In Figure 4-9, thin lines represent the template's shape and thick lines are the shape of defective regions. Since for each thin line, there is a thick line which is almost parallel with it, the thick lines can pass the angle matching step. However, these two shapes can't be fitted very well for any transformation value s and v due to the fact that they are not in a similar shape. To be more specific, two shapes are the same if one of them can be transformed into another shape by a translation, rotation, and scaling transformation with the same scaling factor in both x and y directions. Thus, a large distance difference value will be obtained between two different shapes even they share the same interior angles.

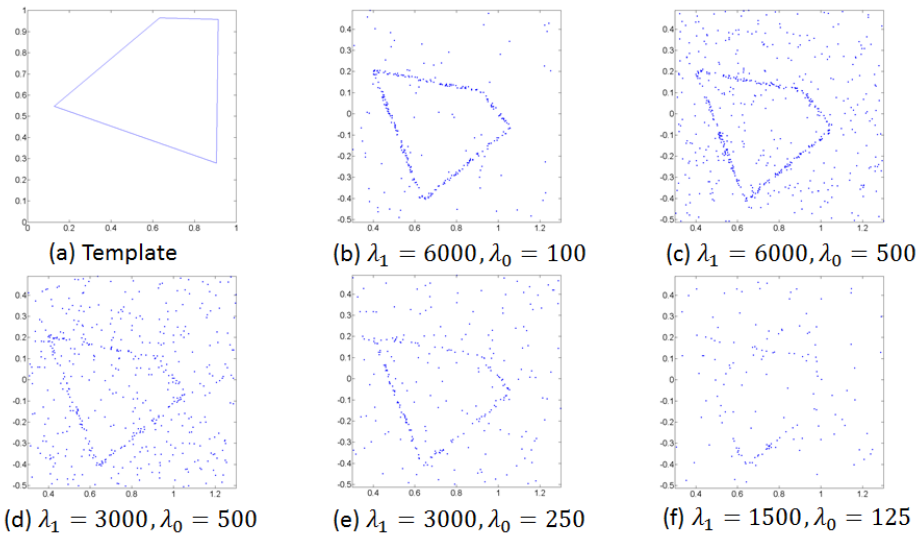

Fig 5-8 Impact of densities of λ_0, λ_1. The defective region is more difficult to be differentiated from the background as λ_1 decreasing. Thus, the power of detection is decreasing.

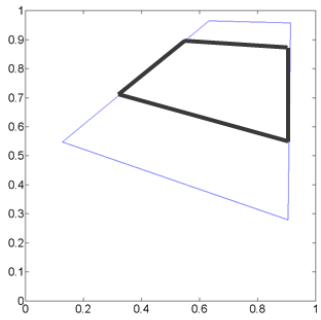

Fig 5-9 Shape variation. Thick lines are the shape of defective regions and thin lines are the pattern of the template. Due to the different shapes, the defective regions rarely pass the distance matching process.

5.4.2 Discussion of other influential factors

Variations of other parameters besides λ_1 and λ_0 will also influence the performance of the proposed detection method. In this subsection, the impacts of the scaling factors s_x and s_y on the *x* and *y* axis respectively and the width *w* of defective regions are discussed.

(1) Influence of different scaling factors on x and y axis

In subsection 5.4.1, the performance evaluations are conducted for the same scaling factor s in both the x and y directions. In order to investigate the impact of the scaling factor, a further simulation study has been conducted with the scaling factor of x axis s_x fixed to be 0.8 and the scaling factor of y axis s_y chosen as 0.8,0.75, 0.7, 0.6 and 0.5. The defect pattern will be regarded different from the template when $s_y \neq 0.8$. Examples are shown in the Figure 4-10. As we can see from these examples, the shape of defect pattern with $s_y = 0.75$ has very little difference compared to that with $s_y = 0.8$. The differences are becoming more obvious as s_y decreasing. Based on this observation, it's reasonable to expect that the Type I error of the detection will decrease as s_y getting smaller from s_x. The simulation results (see Table 5-5) verify our expectation and indicate that the Type I error is reasonably small when $s_y < 0.7$. Note that, when $s_y = s_x = 0.8$, the Type I error becomes the detection power because the defect pattern in fact matches the template in this case. In this simulation study, simulation parameters $\lambda_1 = 6000, \lambda_0 = 500, n = 4,6 \; and \; w = 0.02$ are used.

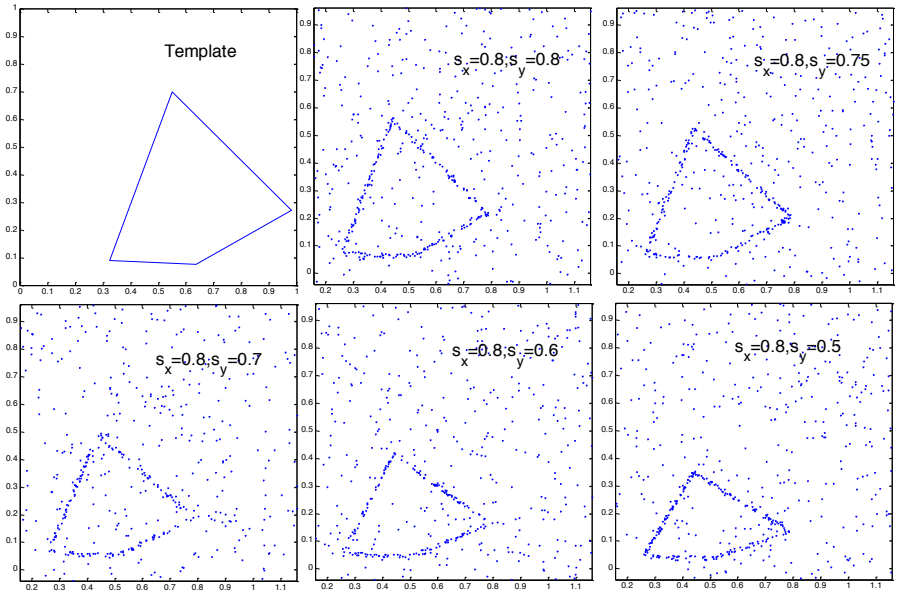

Fig 5-10 Examples of different scaling factors on y-axis.

Table 5-5. Simulation results of Type I error of different scaling factors for *y* axis.

		Power	Type I error			
		sy=0.8	sy=0.75	sy=0.7	sy=0.6	sy=0.5
sx=0.8	n=4	92.17%	17.13%	5.22%	1.89%	0.70%
	n=6	83.07%	9.85%	1.61%	0.58%	0.63%

Note that, the scaling factor s or (s_x, s_y) are all smaller than 1 in the simulation studies. In practice, we can always scale the defect map first to make it small before we apply the detection method. So we only discussed the case of $s < 1$ in the chapter for the sake of simplicity. The situation of $s > 1$ will not cause any extra issue for the algorithm.

(2) Discussion of the Influence of the widths of defective regions

In previous simulation studies, the width w are fixed to be 0.02 for all defective regions for the sake of convenience. On average, the number of defect point in each defective region is $slw\lambda_1$. As w decreasing, the number defect points due to the defect region gets smaller and the defect region will just looks like the background (this is similar to the case when λ_1 is decreasing). Thus, we shall expect a lower detection power with a smaller value of w. In fact, if w is extremely small,

then the detection method will not be able to differentiate the defective region with the background noise. On the other hand, if w is very large, then the defective regions will cover a large space in the defect map with density λ_1, which will benefit the detection power. However, this will lead to a large Type I error. This is not surprising because with a larger defect region, a larger number of line segments will be detected and will lead to larger number of false alarms in the pattern detection step. A simulation with parameters $\lambda_1 = 6000, \lambda_0 = 500, s = 0.8, \text{and } n = 4$ is conducted to investigate the impact of this scenario. In the simulation, w is taken value as 0.01, 0.05 and 0.1. The simulation results are presented in Table 5-6.

Table 5-6. Performance comparison with different ws.

w	Power	Type I error
0.01	82.50%	0.13%
0.02	93.18%	0.40%
0.05	94.77%	1.05%
0.1	97.15%	4.87%

The result is consistent with the intuition. There could also be a situation that the widths of the edges of the defect pattern are different. In section 4.3, $\delta\rho$ is desgined to be no larger than $w/2$ in order to guarantee that at least one Hough strip is fully overlapped with each defective region. If the widths of defective regions are different, in order to reach the above criteria, we need to have $\delta\rho = \min(w_i)/2$ to insure the defective region with the smallest width being fully overlapped with a Hough strip. Since $\delta\rho$ is selected to accommodate the defective region with the smallest width, there may be multiple Hough strips with width $\delta\rho$ fully overlapped with defective regions that have larger widths. Thus, one can expect multiple patterns with small variations from each other will be detected by the proposed detection method.

5.4.3 Comparison with the Generalized Hough Transform (GHT)

In this subsection, the proposed detection method is compared with the GHT, which is a popular method in detecting arbitrary shapes. The details of the GHT algorithm can be found in [130]. The comparison results are presented in Table 4-7.

Table 5-7. The comparison between the proposed detection method and GHT

		Proposed Detection Method				Generalized Hough Transform			
		n=4(s=0.8)		n=6(s=0.8)		n=4(s=0.8)		n=6(s=0.8)	
λ_1	λ_0	Power	Type I error	Power	Type I error	Power	Type I error	Power	Type I error
6000	500	93.18%	0.40%	88.42%	0.70%	81.75%	0.70%	78.31%	1.50%
3000	250	86.08%	0.50%	70.12%	0.20%	66.20%	0.60%	59.42%	0.50%
1500	125	58.47%	0.40%	42.18%	1.20%	27.52%	0.40%	22.47%	1.70%
Average Running Time		0.9395s		1.0328s		1.9206s		3.5309s	

From these comparison results, we can see that the proposed method has higher detection power and has a faster speed than GHT in detecting patterns consisting of multiple line segments. In addition, in this comparison, the scaling and rotation are not considered in the GHT (i.e., $s = 1, \text{and } \alpha = 0^o$). If these two transformations are involved, the detection power of GHT will further decrease and the average running time will increase due to that two more parameters s and α need to be calculated in the detection.

5.5 Case Study for Wafer Defect Pattern Detection

In this section, we shall use a case study for wafer defect pattern detection to demonstrate the effectiveness of the proposed method. Wafer defect distributions and yield patterns are an important source of information about the performance of a wafer production line [117]. Under normal working condition, the spatial distribution of the defects on the wafer is typically pure random and does not exhibit any systematic pattern. The systematic distribution pattern often indicates the existence of an abnormal condition. For example, the defects may distribute in a circular or semi-circular region near the edge of the wafer [117]. The potential root cause of this pattern is the damage of the die during yielding. In this section, we apply the proposed pattern

detection method to detect such pattern. We would like to point out that although the true template is circular in shape, we can certainly use multiple line segments to approximate the shape and use the approximation line segments as the template. Actually we can significantly expand the applicable field of the proposed method through this approximation.

The defect maps used in this case study is shown in Figure 4-11. Figure 4-11(a) is generated using a real defect map from [117]. Figure 4-11(b,c) are generated numerically through simulation based on the characteristics of the observed distribution characteristics in practice [118]. Specifically, in generating the defect maps, we set the background noise $\lambda_0 = 50$ in a $1x1$ unit square, the defective rate $\lambda_1 = 500$ for the circular defective region with width $w = 0.10$. In this case, the total points in Figure 4-11(b,c) are 139 and 120 respectively compared with the 117 points in the Figure 4-11(a). To detect the defect pattern, we create a template consisting 5 line segments with the same length $l = 0.5$ to approximate the semi-circular pattern. The template is shown in Figure 4-11(d).

The numerical results of the pattern detection are the following. Based on the parameter selection method discussed in Section 4.3, the HT parameters of the detection are designed as $\delta\theta = 1^{\circ}$ and $\delta\rho = \frac{w}{2} = 0.05$. The threshold t_p of the peak value equals to $t_p = rH_p = 0.61 \times 27 \approx 17$, i.e., pairs (θ, ρ) with voting score smaller than 17 will be not be considered. The threshold $t_\theta = 10^{\circ}$ and $t_\rho = 0.11$. The final results have distance differences d^* =0.082, 0.079 and 0.081 with rotation angles $\alpha = -73^{\circ}, -15^{\circ}$and $65^{\circ}$from the template, respectively. The one that passes the angle test and is with the smallest distance difference is chosen as the final result, and the graphical result is presented in Figure 5-12(a). Similarly, Figure 5-12(b,c) are the graphical results of the two simulated cases.

The results show that the proposed pattern detection algorithm can effectively detect ring patterns in wafer defect maps.

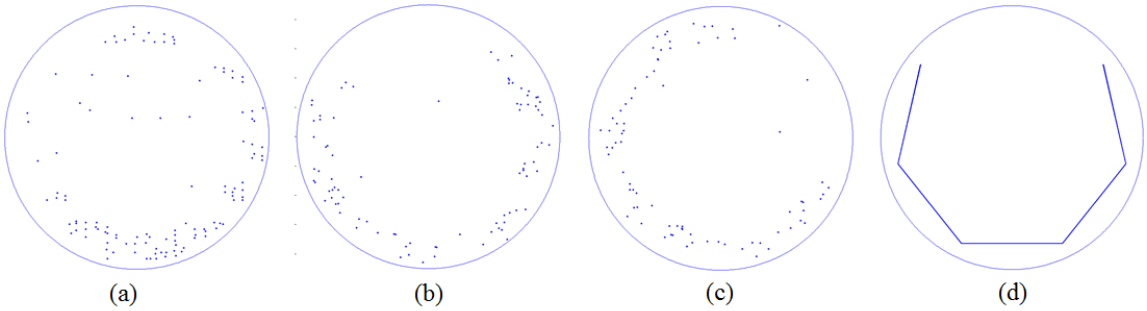

Fig 5-11 Wafer defects. (a) is a real wafer defect map. (b) and (c) are generated by simulation. (d) is the template being used in all three cases.

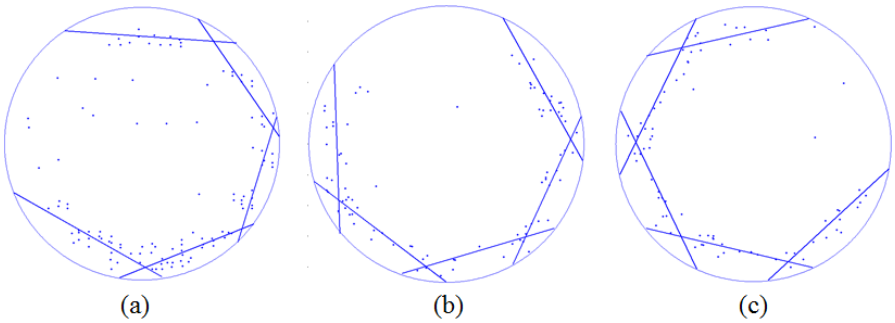

Fig 5-12 Detection results of three defect maps. The lines in each figure are the detected pattern.

In the above case study, a 5-line segment template is used to approximate the ring defects pattern. However, we could also use smaller number of line segments, e.g., 4 or larger number of line segments, e.g., 8, to approximate the original template. A tradeoff needs to be considered in determining the number of line segments used. The tradeoffs contains the following two aspects. On one hand, it is obvious that to accurately approximate a continuous pattern, we need large number of line segments with small length. For example, in this case, an 8 line segment approximation will give us better approximation to the ring-type of defect pattern. On the other hand, a template with large number of short lines will impact on the detection power. As we have discussed in section 4.4.1, a shorter edge will contain relatively less defects which will increase

the difficulty in detection. Furthermore, as the number of edges increases, the detection power decreases. From this detection power point of view, an approximation using smaller number of line segments is better.

A simulation is conducted to confirm this understanding. In this simulation, we present three alternative template approximation for the circular defects with 5, 4 and 8 edges respectively. Simulation parameters $\lambda_1 = 500, \lambda_0 = 50, w = 0.1$ and $s = 1$ are used. The results of the simulation are presented in Table 4-8.

Table 5-8. Performance comparison among the three alternative templates

	Power	Type I error
n=5	54.21%	1.10%
n=4	60.93%	1.50%
n=8	33.28%	0.70%

From the results, we see the template with 5-line segments has a higher detection power than the 8-line segments template, while lower than that of the 4-line segments template.

Due to the above mentioned trade-off, if the precise shape of the template is not critical (e.g., for the cases that different fault modes lead to quite different fault patterns), then a rough approximation with small number of line segments is preferred. However, if the precision shape is required, then a careful analysis should be conducted to approximate the shape to a required accuracy level with smallest number of line segments. This is an interesting topic and a further research on this tradeoff is needed in the future.

5.6 Conclusion

In this chapter, we proposed a HT-based method to detect point patterns that consist of arbitrary line segments. The basic idea is to convert the line pattern detection problem in physical domain into the problem of detecting multiple points in Hough domain. The detection is attained through two critical steps, the angle matching and the distance matching, which allows arbitrary rotation, scaling, and translation of the pattern. Based on the simple intuition that a line is most likely to be detected if a Hough strip fully overlaps with the defective region, a detailed discussion on how to select tuning parameters of the algorithm, such as $\delta\theta, \delta\rho$, t_p,t_θ, t_ρ, and p_{λ_0} are provided. An extensive numerical study shows that the detection method performance well in terms of both Type I error and the detection power if the defective region has reasonable size and the contrast between the defective region and the background noise is reasonably large.

6 Microstructure Modelling and Ultrasonic Wave Propagation Simulation of A206-Al_2O_3 Metal Matrix Nanocomposites for Quality Inspection [*]

The research in this chapter is motivated by the complexity of the wave-microstructure interaction, and the difficulty in fabricating nanocomposites of different microstructural features in ultrasonic testing. It is very challenging to build reliable relationships between ultrasonic testing results and nanocomposites quality. In this chapter, we propose a microstructure modelling and wave propagation simulation method to simulate ultrasonic attenuation characteristic for A206-Al_2O_3 metal matrix nanocomposites (MMNCs). In particular, a modified Voronoi diagram is used to reproduce the microstructures and the numeric method elastodynamic finite integration technique (EFIT) is used to simulate the wave propagation through the generated microstructures. Linear mixed effects model (LME) is used to quantify the between-curve variation of ultrasonic attenuation from both experiment and simulation. Permutation test is employed to quantify the similarity of the quantified variation between experiment and simulation. This research supports the experimental results through the simulation approach and provides an efficient way for quality inspection of MMNCs.

6.1 Introduction

A206-Al_2O_3 metal matrix nanocomposites (MMNCs), where lightweight A206 alloys (93.5% -95.3%Al, 4.2%-5.0% Cu) are reinforced with nanosized Al_2O_3 particles, have been intensively studied recently because of their significantly enhanced mechanical properties, such as high strength, ductility, long fatigue life, and excellent hot tearing resistance [131-134]. It can be

[*] This chapter is based on the paper: **Liu, Y**., Wu, J., Zhou, S., & Li, X. (2016). Microstructure Modeling and Ultrasonic Wave Propagation Simulation of A206–Al2O3 Metal Matrix Nanocomposites for Quality Inspection. Journal of Manufacturing Science and Engineering, 138(3), 031008.

fabricated by dispersing Al_2O_3 nanoparticles into the molten A206 using ultrasonic cavitation assisted casting technologies [135, 136]. Well dispersed Al_2O_3 nanoparticles in A206 have strong nucleation potency and can significantly reduce the grain size of the primary Al phase and break the Al_2Cu intermetallic network [131, 133], thus leading to significantly reduced hot-tearing susceptibility and enhanced mechanical properties. To facilitate the scale-up production, a fast yet effective quality inspection technique is critically important to ensure the quality of nanoparticle dispersion and morphology modification. Currently, the standard quality inspection method is to use microscopic images of nanocomposites microstructures, which are very time-consuming and costly to obtain. It is highly desirable to develop alternative simpler and effective quality inspection techniques.

Ultrasonic testing is one of the most popular nondestructive evaluation techniques. It has been intensively investigated and widely used in size measurement, flaw detection [137], structural health monitoring (SHM) [138], and materials and biological tissue characterization [139-143] etc. Ultrasonic attenuation is one of the most commonly used ultrasonic parameters in the ultrasonic testing applications. It refers to the decaying rate of the acoustic wave as it propagates through materials, which can be measured using the spectral ratio analysis technique [144], as shown in Fig 6-, where the two successive echoes reflected from the back wall of the sample are extracted and ratio of the spectrum amplitude is used to calculate the attenuation curves. The ultrasonic attenuation is highly dependent on the material properties and microstructural features, e.g., elastic constant, grain size, grain boundaries, inclusions, porosity and dislocations. Therefore, ultrasonic testing is promising to be an economical and effective method to characterize the microstructural configurations and material properties.

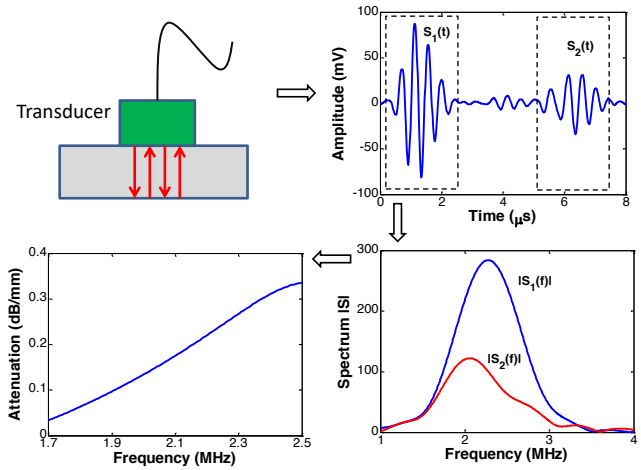

Fig 6-1 Illustration of the ultrasonic testing using ultrasonic attenuation curves [133].

Recently, Wu *et al* [133] discovered an important relationship between acoustic attenuation profiles and the microstructural characteristics of A206-Al_2O_3 nanocomposites. For nanocomposites with satisfactory microstructures (i.e., small grain size, dissolved Al_2Cu phase and well dispersed Al_2O_3 nanoparticles), the between-curve variation of attenuations measured at different locations is much lower than that of bad quality nanocomposites. This study provided useful guidelines to establish a new quality inspection technique for A206-Al_2O_3 MMNCs. However, there still exist several issues that need to be addressed in order to develop a reliable quality inspection method: 1) there are multiple microstructural features (e.g., grain size, Al_2Cu morphology) affecting the variation of ultrasonic attenuation. However, due to the complexity of the interaction between the microstructural configuration and wave propagation, how each feature contributes to the variation is still unknown; 2) the nanocomoposites samples and experimental data are quite limited because of the high experimental cost and the difficulty in fabricating samples with planned microstructural features, which makes it difficult to build a quantitative relationship between the attenuation curve and microstructural features.

For the reasons given above, numerical simulations of ultrasonic wave propagation in A206-

Al_2O_3 MMNCs are needed to support the experimental tests by generating alternative data under different microstructural features, leading to a better understanding of the relationship between the microstructural configurations and attenuations. Numerical simulation of ultrasonic wave propagation have attracted intense interest for its promising in solving problems that may be inaccessible to direct experimental study or too complicated for theoretical analysis. It allows easy control of each experimental parameter independently, which enhances the understanding of wave propagation in complex systems. The most common techniques used to solve the wave propagation equations include the finite difference methods (FDM) [145-147], the elastodynamic finite integration technique (EFIT) [148], the finite element method (FEM) [149, 150], and the spectral finite element method (SFEM) [151]. Acoustic wave simulation has gained more popularities in many areas in recent years for the progress in computational power and availability. For instance, assessing the stability of an implant is difficult due to the complex heterogeneous nature of bone in ultrasonic bone and biological implant characterization. The use of numerical simulation enable researchers to understand the wave propagation phenomena occurring in prototype titanium cylindrical implants and to investigate the sensitivity of the ultrasonic response to variations of the biomechanical properties of surround tissues, which are determinant for the implant stability [143, 147, 152]. Another example is the area of structural health monitoring (SHM). SHM for the detection of damage in aerospace materials is an important engineering area. Experimental signals of complicated flaw geometries may be difficult to interpret. With the help of numerical simulation, scientists are able to investigate ultrasound scattering from flaws in materials and to develop optimized experimental SHM techniques [153]. Ultrasonic wave propagation simulation has also been applied in materials characterization [154, 155], however, very limited simulation work has been done on lightweight alloy based nanocomposites.

In this study, the simulation approach to model the microstructural features of A206-Al2O3 MMNCs in 2D space is developed and the ultrasonic wave propagation on the generated nanocomposites is simulated to study the relationship between the microstructural properties and ultrasonic attenuations. To simulate the MMNCs microstructure, a Voronoi diagram is first generated, and then the edges of the generated diagram is modified to describe different morphologies of Al2Cu intermetallic phase. In the wave propagation simulation, the EFIT is selected for the following reasons: 1) EFIT naturally requires staggered spatial and temporal grids, which leads to stability; 2) boundary conditions are easily incorporated into EFIT; 3) the mathematical analysis is straight-forward and leads to equations that are easy to implement in any programming language. The simulated acoustic attenuations are consistent with the experimental measurements, which then can be used to further investigate the relationship between the microstructural properties and ultrasonic attenuations and to develop statistical quality control methods for scale-up production.

The rest of this chapter is organized as follows. In Section 5.2, the Al2O3 nanoparticle based morphology modification mechanism is first introduced. Then the microstructure of A206-Al2O3 MMNCs is simulated based on the microscopic images and the morphology modification mechanism. In Section 5.3, the EFIT is briefly introduced. The simulation and experimental results are presented in Section 5.4. The statistical similarity testing between the simulation results and the experimental ultrasonic measurements is given in Section 5.5. Section 5.6 presents the conclusion.

6.2 Modelling and Simulating Microstructure of A206-Al_2O_3

In this section we first introduce the microstructural features of the A206 alloys and Al_2O_3 reinforced nanocomposites, and the morphology modification mechanisms. Based on these

features, we propose a new microstructure modelling method. Three experimental samples are used in this chapter to show the microstructural features and measured attenuations curves: the A206 alloy, the A206-Al_2O_3 MMNCs with 1wt.% and 5wt.% of Al_2O_3 nanoparticles. These samples are fabricated using the ultrasonic cavitation based casting technology [133]. The experimental setup of ultrasonic processing in the casting of A206–Al_2O_3 MMNCs consists of a resistance heating furnace, an ultrasonic cavitation based processing system (Misonic Sonicator 3000) with a niobium probe of 12.7 mm in diameter and 92 mm in length, a temperature control system and a gas protection system. A graphite crucible with an inner diameter of 88.9 mm and a height of 101.6 mm was used for melting. The ultrasonic probe vibrates with the operating frequency of 20 KHz and power of 4.0 KW. A206 alloy was first melted in the graphite crucible under the protection of argon gas with temperature controlled at 700℃. The γ-Al_2O_3 nanoparticles with a diameter of 50 nm were then added into the molten melt with ultrasonic cavitation turned on for 15 minutes. Then the molten melt was heated up to 740℃ and poured into a steel permanent mold with a preheated temperature of 400℃. The casted samples are polished for ultrasonic testing. The attenuations were measured using the Olympus Epoch 1000 series NDT device using transducer D785-RP with a nominal central frequency of 2.25 MHz.

6.2.1 Microstructures and Morphology Modification

The left panel in Fig 6- shows the representative optical micrographs (top) and polarized light micrographs (bottom) of pure A206 and A206-1wt.%Al_2O_3 nanocomposite [133], and the right panel shows the simulated microstructures. The pure A206 alloy exhibits large dendritic primary α-Al surrounded by continuous θ-Al_2Cu phases. The θ-Al_2Cu phases are distributed along the boundaries of primary aluminum grains and have the morphology of long continuous network. For the nanocomposites with 1wt.% Al_2O_3 nanoparticles, the α-Al dendrites becomes small equiaxed

crystals and the intermetallic θ-Al_2Cu phases turn to be smaller, thinner and much less continuous. It indicates that the Al_2O_3 nanoparticles can reduce the grain size of α-Al phase and break or refine the θ-Al_2Cu phase.

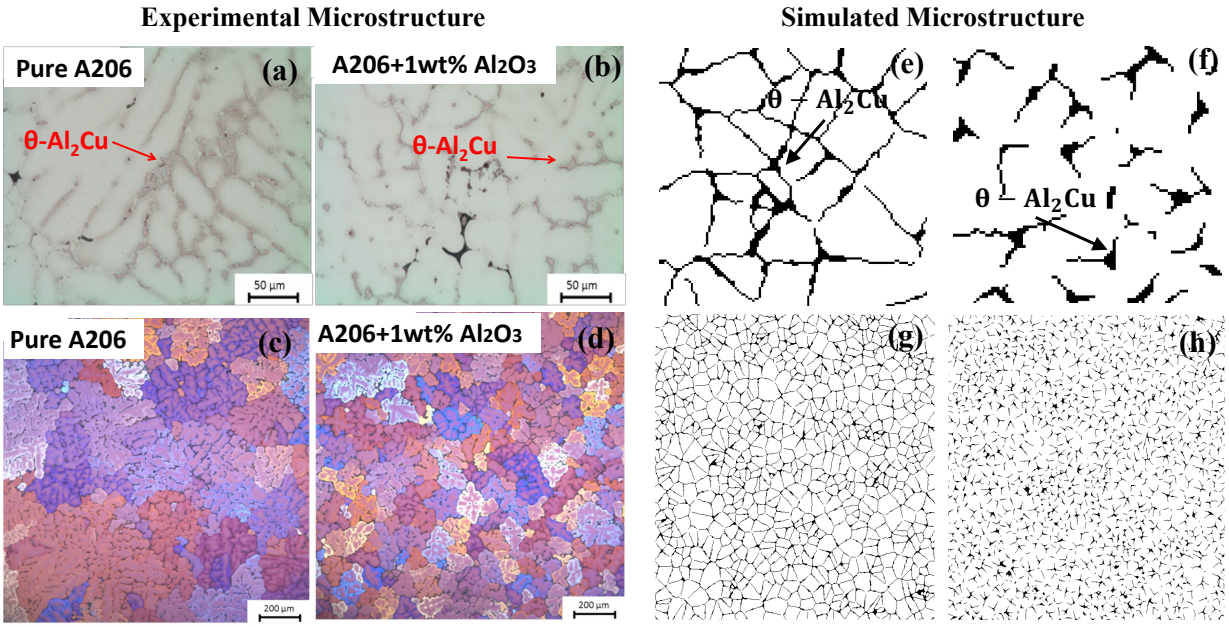

Fig 6-2 Microstructures for pure A206 and A206-Al_2O_3 MMNCs. Left panel: experimental micrographs. Right panel: simulated microstructures.

The formation mechanism of the continuous network of θ-Al_2Cu in A206 and the morphology modification mechanism by Al_2O_3 in A206-Al_2O_3 nanocomposites have been well studied [131, 134, 156, 157]. For the pure A206 alloys, due to the high percentage of Al content, the primary α-Al phases nucleate first and then grow to large dendritic structure during the solidification process. The Cu solute is pushed out of the α-Al phases into the remaining liquid phase due to the high super-cooling of the θ-Al_2Cu nucleation. As the temperature decreases and the content of Cu increases in the remaining liquid, the θ-Al_2Cu phase is finally able to nucleate and grow between α-Al dendrites. At last, the θ-Al_2Cu phase will form a layer in-between the α-Al dendrites, which is called the divorced eutectic microstructure.

For the A206-Al_2O_3 nanocomposites, however, the eutectic formation mechanism is modified with the existence of Al_2O_3 nanoparticles. Similarly, the primary α-Al phases first nucleate and grow in the melt, pushing most of the Al_2O_3 nanoparticles and Cu to the remaining liquid. The Al_2O_3 nanoparticles have good nucleant potency and they can serve as effective nucleation sites for θ-Al_2Cu to nucleate and grow before the remaining liquid reaches the eutectic composition. While the θ-Al_2Cu phases are growing, the liquid surrounding the θ-Al_2Cu is enriched with Al due to the depletion of Cu. Consequently, the α-Al phase nucleates and grows on the edges and tips of the θ-Al_2Cu, which blocks the growth of θ-Al_2Cu. Finally, the partially divorced eutectic phase is formed and both α-Al phase and θ-Al_2Cu phase are refined.

6.2.2 Microstructure Modelling Using Voronoi Diagram

To achieve successful simulations of the ultrasonic wave propagation and reproduce the comparable attenuation curves, the key step is to generate microstructures that can sufficiently capture the microstructural features of A206-Al_2O_3 MMNCs. The most common method to generate polycrystalline material structure in the computational materials science is the Voronoi diagram or Voronoi tessellation [158-161]. It assigns the same number of points to the space as the desired number of grains, and the space is subsequently divided into many polyhedral based on the closeness to these points. Fig 6- shows a representative Voronoi diagram where the space is partitioned to 20 cells based on the 20 randomly generated points.

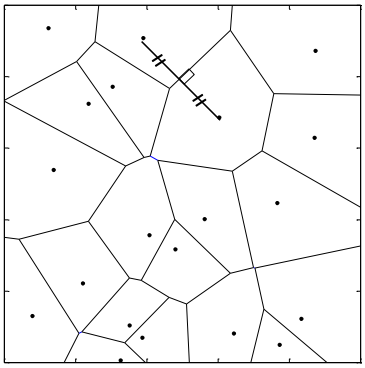

Fig 6-3 Example of Voronoi diagram with 20 random points.

Based on the micrographs of A206-Al_2O_3 MMNCs (Fig 6- left panel) and the morphology modification mechanism, we know that the intermetallic network is broken and become thinner and less continuous with the introduction of Al_2O_3 nanoparticles. The extent to which the intermetallic phase is modified is positively correlated with the amount of Al_2O_3 nanoparticles [133]. To model this microstructural feature, we first generate a Voronoi diagram with an appropriate number of grains N, and then modify the edges by: 1) randomly selecting some edges, 2) shortening these selected edges, and 3) randomly assigning the width of the remaining edges. After these operations, we obtain a modified Voronoi diagram with edges denoting the intermetallic θ-Al_2Cu phase and the inner space denoting the primary α-Al phase. The rationale of this strategy to model the nanocomposites for ultrasonic wave propagation simulation is based on the following considerations and simplifications: 1) It is known that when the grain or inclusion size is less than 1/1000 of the wavelength, its scattering effects on the acoustic wave are negligible [162]. Since the sizes of the dispersed nanoparticles are significantly smaller than the ultrasonic wave length (2~3mm), we neglect the wave scattering by nanoparticles and do not consider nanoparticles in the microstructure simulations; 2) The acoustic scattering arises at the boundaries between grains or inclusions due to the change of material properties. The neighboring α-Al grains have slightly different material properties because of their different crystal orientations. Therefore

the boundaries between α-Al grains can scatter acoustic waves and contribute to ultrasonic attenuations. However, their scattering effects are negligible compared with those between α-Al grain and θ-Al_2Cu phase. Therefore, to simplify the modeling process, the grain boundaries between α-Al grains are not considered.

To implement the first two operations in the edge modification process, we introduce another two parameters: 1) α, the percentage of edges in the Voronoi diagram to be dissolved, and 2) β, the percentage of length left after dissolving. For example, if there are total 100 edges in the diagram, $\alpha = 0.3$ and $\beta = 0.7$ means 30 edges are randomly selected and each of the selected edges is dissolved to 70% of its original length. Fig (b) shows a result of applying α and β to the initial Voronoi diagram in Fig (a). A well fabricated nanocomposites is featured by small grain size and short intermetallic phases. Therefore we can select large N, large α and small β to model the microstructures of the good samples. For the experimental microstructures, the thickness of the intermetallic is not constant. To model this, we add random widths to each edge after the edge dissolving step (Fig (b)) using the following way (shown in Fig (d)). We first select m points with equal interval for each edge, and then assign two points for each selected point along two sides at the same horizontal location with uniformly distributed distances in the vertical direction. After that these assigned points are connected to form a polygon and finally the space within each polygon is used to denote the intermetallic phase. In this width assigning step, the number of middle points m and the distribution parameters of the random distance can be changed to capture various microstructures. Note that we do not keep the amount of intermetallic phase constant in the morphology modification process. The reason is that the dissolved part of the intermetallic phase is very small in size and has negligible effects on the acoustic attenuation. For simplicity,

we do not consider this aspect in the microstructure modeling process. In summary, the microstructure generation procedure is listed in Table 6-1.

Table 6-1. The microstructure generation procedure.

Input N

1) Generate N random points.
2) Partition the pace using ordinary Voronoi diagram based on N generated points.
3) Index all edges in the diagram.

Input α, β

4) Randomly select α percentage edges among all edges.
5) Shorten the selected edges to β percentage of their original lengths.

Input m, u_l and u_u

6) Evenly select m middle points for each edge
7) Generate one point above each selected point with vertical distance following uniform distribution $U(u_l, u_u)$.
8) Generate one point below each selected point with random distance following uniform distribution $U(u_l, u_u)$.
9) Connect the generated points to form polygons.
10) Fill polygons with black color representing the θ-Al_2Cu phase

Fig shows the overall microstructure modeling process and Fig 6- (right panel) shows four generated microstructures to simulate pure A206 and A206-Al_2O_3 MMNCs. In Fig, we present several simulated microstructures with different parameters α, β and N. Typically, a small *N* and a large βwill be chosen for pure A206 and a large *N* and a small $\beta$for A206-Al_2O_3. By adjusting these parameters, we can generate microstructures that are similar to the observed microstructures. For example, the modified Voronoi diagrams are visually similar to observed microstructures in Fig 6-. The similarity can also be roughly quantified. In Fig. 6-2, the microstructure of pure A206

(Fig. 2a and 2c) and the composite with 1wt% Al_2O_3 (Fig. 6-2b and 2d) are simulated using parameter combinations N=800, β=0.9,α=1.0 (Fig. 5- 2e and 2g) and N=1200, β=0.7,α=1.0 (Fig. 5-2f and 2h), respectively. Through a simple image processing and measure of the optical image, we found that the average grain sizes are ~1936 μm^2 and ~1309 μm^2 and the percentage of the dark phase that corresponds to Al_2Cu are 10.75% and 5.13% for pure A206 and the composite with 1wt% Al_2O_3, respectively. In the corresponding simulated microstructure, the average grain sizes are ~1849 μm^2 and ~1156 $\mu m^2$and the percentage of the dark phase are 10.02% and 5.05%, respectively. We can see that these measures are close between the observed and the simulated microstructure.

The simulated microstructures will be used as the input in the wave propagation simulation. In the next section, we introduce the EFIT, the acoustic attenuation simulation in details.

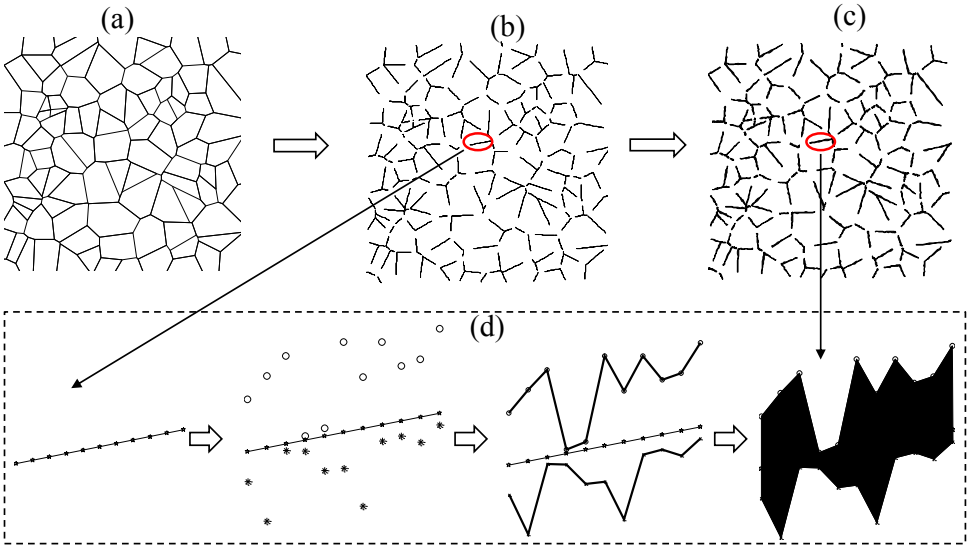

Fig 6-4 The microstructure modeling process: (a) initial Vononoi diagram, (b) after edge dissolving step controlled by $\boldsymbol{\alpha}$ and $\boldsymbol{\beta}$, (c) after assigning random thickness to each edge, (d) the random thickness assigning process.

6.3 Wave Propagation Simulation using EFIT

The EFIT is a very stable and efficient numerical scheme to model wave propagation in homogeneous and heterogeneous, isotropic and anisotropic elastic media. It was first developed by Fellinger et al [148], and since then it has been widely used to explore elastic wave behaviors in a variety of applications [153, 163]. The EFIT uses velocity-stress formalism on a staggered spatial and temporal grid. It discretizes the following first-order equations:

$$\iiint_{\mathbf{v}} \frac{\partial}{\partial t}\underline{\mathbf{p}}(\underline{\mathbf{r}},\mathbf{t})\mathbf{d}\boldsymbol{V} = \oiint_{\boldsymbol{S}} \underline{\mathbf{n}}\cdot\underline{\underline{\mathbf{T}}}(\underline{\mathbf{r}},\boldsymbol{t})\mathbf{d}\boldsymbol{S} + \iiint_{\mathbf{v}} \underline{\mathbf{f}}(\underline{\mathbf{r}},\boldsymbol{t})\mathbf{d}\boldsymbol{V}\,, \tag{6.1}$$

$$\iiint_{\mathbf{v}} \frac{\partial}{\partial t}\underline{\underline{\mathbf{S}}}(\underline{\mathbf{r}},\mathbf{t})\mathbf{d}\boldsymbol{V} = \oiint_{\boldsymbol{S}} \mathbf{sym}\{\underline{\mathbf{n}}\,\underline{\mathbf{v}}(\underline{\mathbf{r}},\boldsymbol{t})\}\mathbf{d}\boldsymbol{S} + \iiint_{\mathbf{v}} \underline{\underline{\mathbf{h}}}(\underline{\mathbf{r}},\boldsymbol{t})\mathbf{d}\boldsymbol{V}. \tag{6.2}$$

$\underline{\mathbf{p}}$ is the momentum density vector, $\underline{\underline{\mathbf{T}}}$ the stress second rank tensor, $\underline{\underline{\mathbf{S}}}$ is the strain second rank tensor, $\underline{\mathbf{v}}$ is the particle velocity vector, $\underline{\mathbf{f}}$ is the source of force density, $\underline{\underline{\mathbf{h}}}$ is the source of deformation rate second rank tensor, $\underline{\mathbf{n}}$ is the outward normal unit vector of S and $\mathbf{sym}\{\underline{\mathbf{n}}\,\underline{\mathbf{v}}(\underline{\mathbf{r}},\boldsymbol{t})\}$ denotes the symmetric part of the dyad $\{\underline{\mathbf{n}}\,\underline{\mathbf{v}}(\underline{\mathbf{r}},\boldsymbol{t})\}$. More detailed explanation of (1) and (2) can be found in [164].

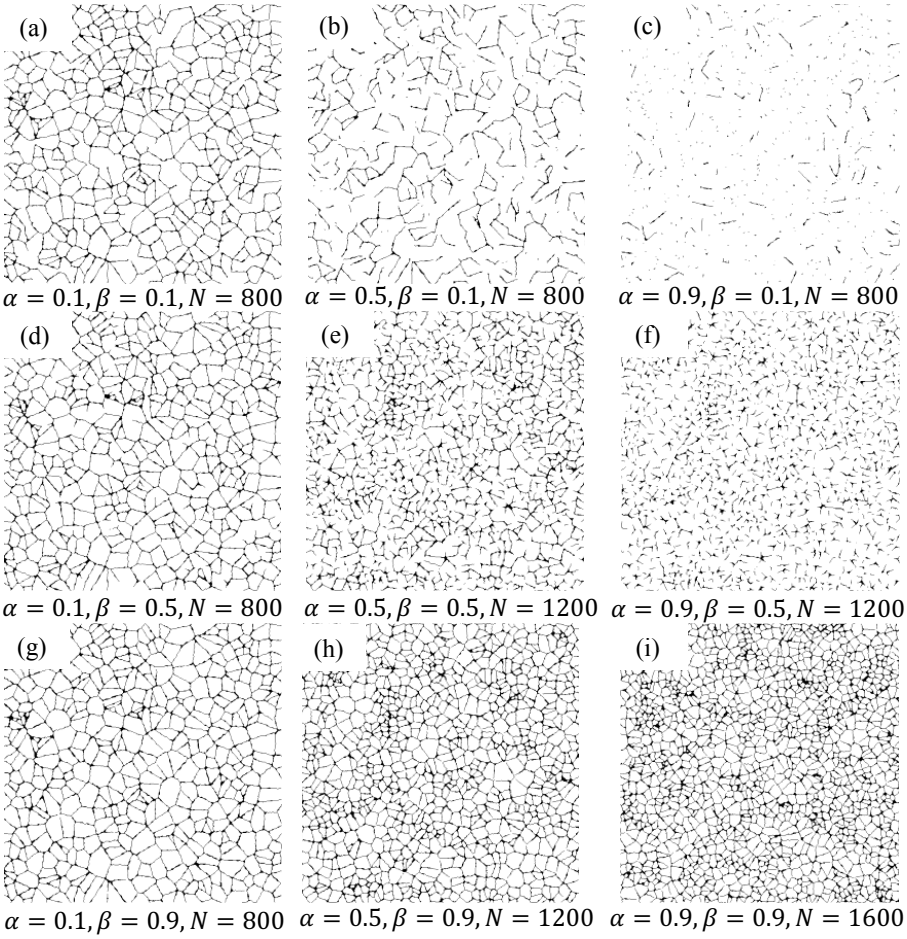

Fig 6-5 Microstructures generated using different parameters $\boldsymbol{\alpha}$, $\boldsymbol{\beta}$ and $\boldsymbol{N}$.

In our research, we employ the existing code Visco-Elastodynamic Finite Integration Wave Solver (VEFIT) [165], which is written in C with interface with MATLAB. The VEFIT uses EFIT equations (see Appendix A for details) to solve wave propagation in media. The VEFIT requires a user-defined phantom (i.e., a 2D geometry which can be homogeneous or inhomogeneous), the phantom parameters (i.e., the density of material, the normal and shear velocity of the ultrasonic wave in the media, the bulk viscosity and shear viscosity) and the transducer parameters including the position and size of transducers and the excitation signals as the inputs. The outputs include the stress, the velocity, the acceleration at any selected locations, and the transducers outputs recording the velocity received by transducers at each time step. The transducer outputs will be

used to calculate the acoustic attenuation. Example of input phantom, the wave propagation and the transducers output generated by VEFIT are presented in Fig.

In Fig 5-6, the transducer output shows the waveforms of initial pulse and received echo. The two waveforms are extracted using a rectangular window with the same size. The frequency spectra are obtained by performing the fast Fourier transform (FFT) on the extracted signals. The attenuation can be calculated using the spectral ratio analysis technique [166] as:

$$\boldsymbol{A(f) = \frac{1}{2d}\left(\ln\left|\frac{S_1(f)}{S_2(f)}\right|\right)}, \tag{6.3}$$

where $A(f)$ is the attenuation coefficient at frequency f, d is the thickness of the media, $S_i(f)$ is the frequency spectra calculated using FFT on the extracted signals. $S_1(f)$ is calculated from the incident wave $S_1(t)$ and $S_2(f)$ is from the first bounced back wave $S_2(t)$.

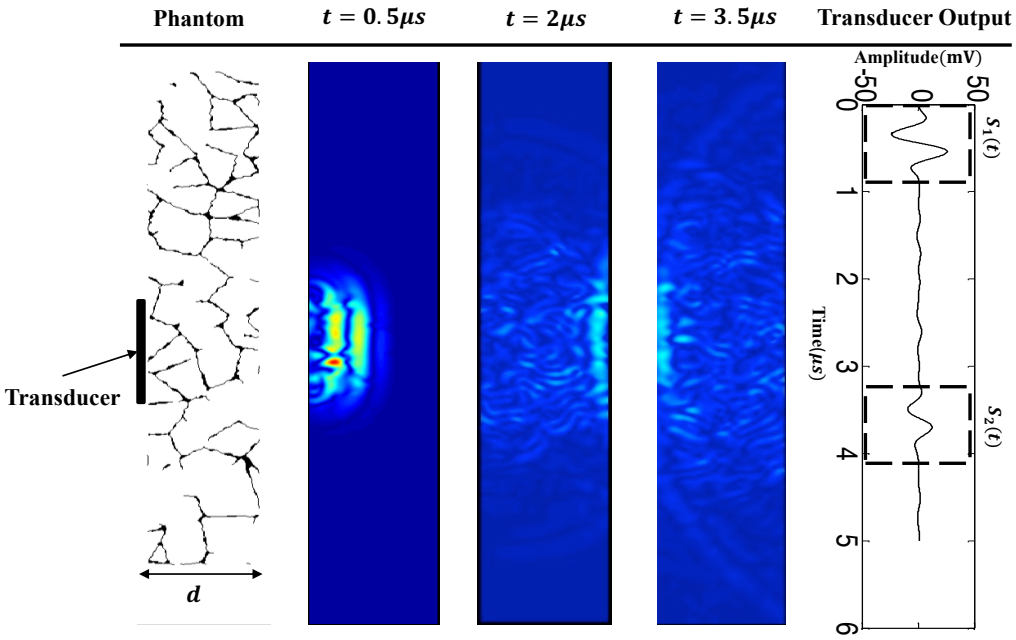

Fig 6-6 Examples of input phantom, wave propagation snapshots and transducer output by VEFIT.

The overall simulation procedure is presented in Fig 6-7. The material properties in the phantom need to be determined. For Al-Cu alloy A206, the main chemical compositions are Al

(93.5%-95.3%) and Cu (4.2%-5.0%). The acoustic properties are calculated based on its elastic properties i.e., Young's modulus, Poisson's ratio and density, which are found in [173, 174]. The phantom parameters are summarized in Table 5-2. In the wave propagation simulation, the transducer is placed in the middle of the left side of the microstructure, as shown in Fig 5-7. The size of the microstructure is selected as $1.2\text{mm} \times 1.2\text{mm}$ and the size of the transducer is selected as one sixth of the length of left side of the microstructure. The central frequency of the excitation signals is set to be 2.25MHz, the same as used in the experiment [133]. The boundaries are specified to be absorbing in the top and bottom sides and reflective in the left and right sides. In the next section, the simulation results will be discussed and compared with experimental data.

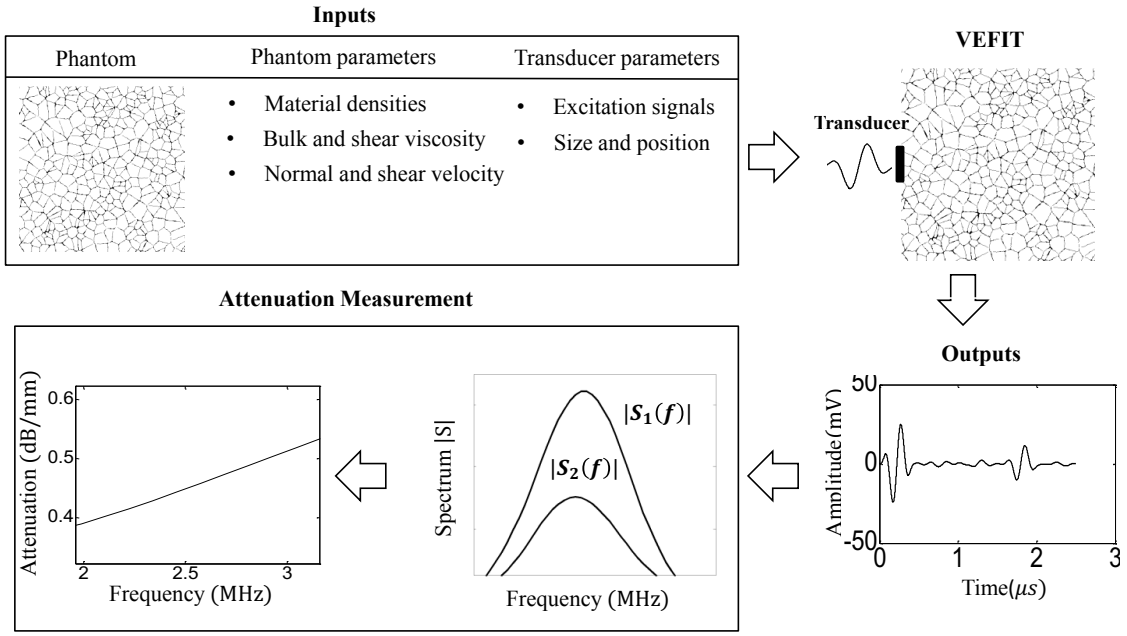

Fig 6-7 Simulation procedure using VEFIT and attenuation measurement.

Table 6-2. Phantom parameters of $\mathbf{Al_2Cu}$ and Al

	Density (g/mm^3)	Normal velocity(m/s)	Shear velocity(m/s)	Bulk viscosity	shear viscosity
Al_2Cu	0.00436	5945	2892	0	0
Al	0.0027	6420	3040	0	0

6.4 Simulation and Experimental Results

In the first set of simulation, we fix $\alpha = 1.0$, i.e., we dissolve all edges of the initial Voronoi diagram. The number N of cells ranges from 800 to 1600. $N = 800$ is approximately the number of grains in pure A206 in the space of $1.2\text{mm} \times 1.2$ mm. $N = 1600$ is roughly the number of grains in A206 nanocomposites of the same dimension size with 5wt.% Al_2O_3 nanoparticles. β is chosen from 0.9, 0.7 and 0.5. For every combination of N and β, 20 microstructures are randomly generated for wave propagation simulation. Since the Voronoi diagram is regenerated for each simulation, we expect different attenuation curves for each replication.

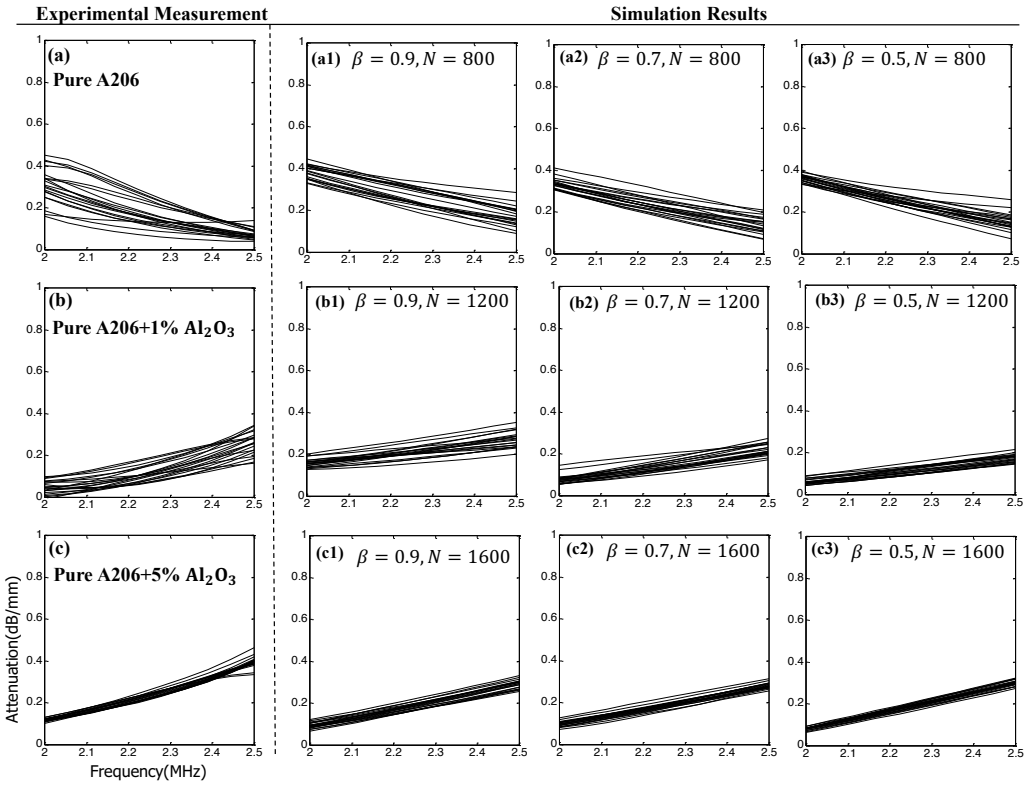

Fig 6-8 The comparison of experimental attenuation curves and the simulated attenuation curves with different simulation parameters (attenuation units: dB/mm, frequency unit: MHz).

Fig 5-8 shows the experimentally measured attenuation curves from [133] and the simulated attenuation curves using different microstructural parameters. In Fig. 6-8, (a), (b) and (c) show experimental attenuation curves measured at 20 randomly selected locations on each sample using the Olympus Epoch 1000 series NDT device with transducer D785-RP of 6mm in diameter and of 2.25MHz in nominal central frequency. Based on the experimental results, Wu *et al* [133] stated that there are three sources that influence the material homogeneity and cause the between-curve variations, the large α-Al dendrites, the long and continuous intermetallic Al_2Cu phases, and the non-fully dispersed Al_2O_3 clusters. Well dispersed Al_2O_3 nanoparticles can enhance the nucleation of both α-Al and Al_2Cu phases, resulting in more homogeneous materials. In the simulation we do not consider Al_2O_3 clusters. Only the grain size of α-Al phase and morphology of Al_2Cu phase

influence the attenuation curves. From Fig we can see that increasing N or decreasing β can reduce the variation of attenuation curves, which is consistent with the experimental results, for that larger N or smaller β indicates a more homogeneous material. Besides, the trend and mean value of the attenuation curves are also quite similar to the experimentally measurements. For the pure A206 alloy, the attenuation decreases with frequency, while for the Al_2O_3 reinforced nanocomposites, the attenuation is more severe for acoustic wave of higher frequency. Therefore, the simulation approach is capable of reproducing the characteristics of the attenuation measurements.

To investigate the influence of parameters α and β on the attenuation curves, we fix $N = 1200$ and run the simulation with different α and β, as shown in Fig. From the simulation results we observe the following phenomenon: 1) For a fixed β, as α increases from 0 to 1, the attenuation curves tend to be more uniform. This is what we expect. Since α controls the percentage of edges being dissolved, more edges dissolved as α increasing result in the more homogenous microstructures; 2) For a larger value β, increasing α will change the attenuation curves less significantly. In the extreme case, if there is no dissolving at all, i.e., $\beta = 1.0$, then the change of α will not influence the attenuation curves. Similarly, for a smaller α, the change of β can hardly influence the attenuation curves; 3) For fixed α or β, the decreasing of β or increasing of α will result in the down shift of the attenuation curves. It is because the decreasing of β or increasing of α for fixed α or β will reduce the amount of the intermetallic phase in the microstructure, thus reducing the wave scattering effects. In the next section, we will investigate the similarity of the between-curve variation between experimental and simulated attenuation curves.

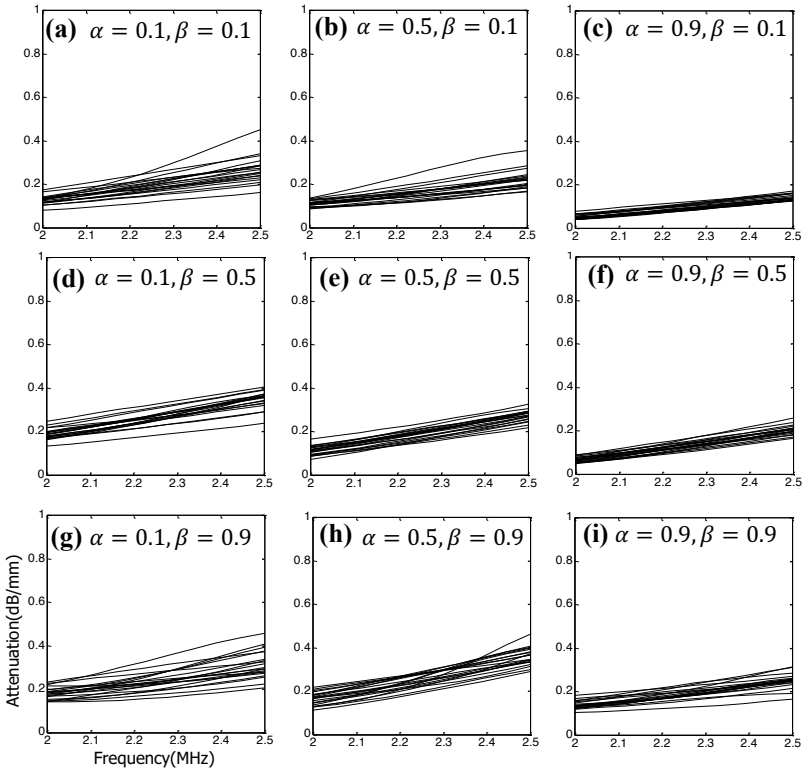

Fig 6-9 The influence of α and β on the attenuation curves (N=1200).

6.5 Statistical Comparison of Experimental and Simulated Attenuation

Both the experiment and simulation show that the between-curve variation can be used to measure the homogeneity of the A206-Al_2O_3 MMNCs. Therefore it is important to quantify this variation and compare it between experiment and simulation for future statistical quality control tool development. From Fig and Fig we can see that all the attenuation curves of each sample share the similar characteristics (e.g.,slope, intercept). On the other hand, the variation from curve to curve also exist for each sample. Therefore, it is natural to select the linear mixed-effects model [167] to describe the population-level features and also model the variation among replicated attenuation curves.

Let y_{ij} denote the acoustic attenuation coefficient for i-th curve at j-th frequency f_j. a and b represent the fixed intercept and slope of the regression line respectively. The linear mixed effects model with first order polynomial in the fixed effects can be written as:

$$y_{ij} = a + bf_j + a_i + b_i f_j + \epsilon_{ij}, i = 1,2, \dots, n, j = 1,2, \dots, m, \quad (6.4)$$

where a_i and b_i are random effects of the intercept and slope for i-th curve with the assumption $\begin{bmatrix} a_i \\ b_i \end{bmatrix} \sim N(\mathbf{0}, \mathbf{\Sigma}), \mathbf{\Sigma} = \begin{bmatrix} \sigma_1^2 & \rho\sigma_1\sigma_2 \\ \rho\sigma_1\sigma_2 & \sigma_2^2 \end{bmatrix}$, and $\epsilon_{ij} \sim N(0, \sigma^2)$ is the error term which is used to model the measurement error or model inadequacy, and is assumed to be independently and identically distributed for all attenuation curves. In this model there are two parts, fixed effects and random effects. Fixed-effects term $a + bf$ is the conventional linear regression part used to describe the population-level mean attenuation curve. The random-effects term $a_i + b_i f$ is associated with individual measurement i and is used to describe its deviation from the mean attenuation curve. Note that we can alternatively use higher order polynomial in the linear mixed effects model. However, this may result in over-fitting issue. The attenuation curves in Fig and Fig show a good linear relationship with frequency f, therefore first order polynomial is sufficient in the model fitting.

The model parameters can be estimated using maximum likelihood estimation (MLE) method. Suppose $\boldsymbol{y}_i = (y_{i1}, y_{i2} \dots, y_{im})$. Denote $\boldsymbol{\beta} = (a, b)^T$, $\boldsymbol{b_i} = (a_i, b_i)^T$, and $\boldsymbol{\Theta} = (\boldsymbol{\beta}, \sigma^2, \boldsymbol{\Sigma})$, then the likelihood function is

$$L(\boldsymbol{\Theta}|\boldsymbol{y}_1, \dots \boldsymbol{y}_n) = p(\boldsymbol{y}_1, \dots \boldsymbol{y}_n|\boldsymbol{\Theta}) = \prod_{i=1}^{n} p(\boldsymbol{y}_i|\boldsymbol{\Theta}) = \prod_{i=1}^{n} \int p(\boldsymbol{y}_i|\boldsymbol{\Theta}, \boldsymbol{b_i}) p(\boldsymbol{b_i}|\boldsymbol{\Theta})\, d\boldsymbol{b_i}$$

where

$$p(\boldsymbol{y}_i|\boldsymbol{\Theta}, \boldsymbol{b_i}) = (2\pi\sigma^2)^{-\frac{m}{2}} \exp\left(-\frac{1}{2\sigma^2} \|\boldsymbol{y}_i - \boldsymbol{X}_i(\boldsymbol{\beta} + \boldsymbol{b_i})\|^2\right)$$

$$p(\boldsymbol{b_i}|\boldsymbol{\Theta}) = (2\pi)^{-1}|\boldsymbol{\Sigma}|^{-\frac{1}{2}}\exp(-\boldsymbol{b_i^T\Sigma^{-1}b_i}/2)$$

$$\boldsymbol{X_i} = [1,1,\dots,1; f_1, f_2, \dots, f_m]^T$$

By integrating out $\boldsymbol{b_i}$ we can get

$$L(\boldsymbol{\Theta}|\boldsymbol{y}_1,\dots\boldsymbol{y}_n) = \prod_{i=1}^{n}(2\pi)^{\frac{m}{2}}\left|\boldsymbol{X}_i\boldsymbol{\Sigma}\boldsymbol{X}_i^T + \sigma^2\boldsymbol{I}\right|^{-\frac{1}{2}}\exp\left(-\frac{1}{2}(\boldsymbol{y}_i - \boldsymbol{X_i\beta})^T\left(\boldsymbol{X_i\Sigma X_i^T} + \sigma^2\boldsymbol{I}\right)^{-1}(\boldsymbol{y_i} - \boldsymbol{X_i\beta})\right)$$

By maximizing $L(\boldsymbol{\Theta}|\boldsymbol{y}_1,\dots\boldsymbol{y}_n)$ with respect to $\boldsymbol{\beta}$ and $\boldsymbol{\Sigma}$, we can obtain the MLE estimated model parameters. The optimization details can be found in [168].

Table 6-3 shows the fitting results for the experimental measurement of A206-5wt.%Al_2O_3 and attenuation curves shown in Fig (c3). We select the attenuation curves in Fig (c3) here as an example due to its visual similarity to the experimental measurements of A206-5wt.%Al_2O_3. From this table we can see that the fitted results for the simulation data are quite close to the experimental data.

Table 6-3. Fitting results for experimental attenuation curves of A206-5wt.%Al_2O_3 and attenuation curves shown in Fig (c3). "Lower" and "Upper" are the lower and upper bound of the 95% confidence interval.

Experimental measurements of A206+5 wt.% Al_2O_3								
Fixed	Estimate	S.E	p-value	Lower	Upper	Random	std	corr
a	-1.00	0.024	≈ 0	-1.05	-0.96	a_i	0.095	
b	0.55	0.011	≈ 0	0.53	0.58	b_i	0.044	-0.996
Simulation data shown in Fig (c3)								
Fixed	Estimate	S.E.	p-value	Lower	Upper	Random	std	corr
a	-0.92	0.015	≈ 0	-0.95	-0.88	a_i	0.069	
b	0.49	0.007	≈ 0	0.48	0.51	b_i	0.034	-0.997

The histograms of the fitted random effects and the residuals are shown in Fig. The fitted a_i, b_i and ϵ_i approximately follow normal distribution, which validates the model assumption of a_i and b_i. From these histograms, we see the linear mixed effects model can model the attenuation curves well.

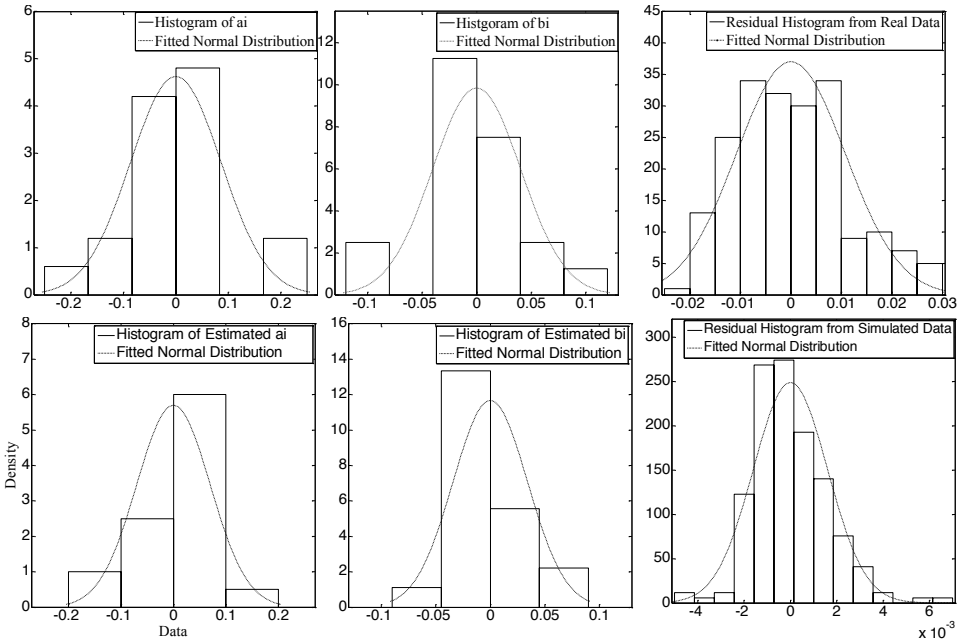

Fig 6-10 Histograms of the fitted random effects and residuals for the experimental measurements of A206-5wt.% Al_2O_3 (top) and simulated attenuation curves shown in Fig (c3) (bottom).

To test the similarity between the simulation and the experimental measurement in terms of the non-uniformity of the acoustic attenuation, we need to compare the covariance matrix $\boldsymbol{\Sigma}^{(s)}$ and $\boldsymbol{\Sigma}^{(r)}$ calculated in the model fitting, where $\boldsymbol{\Sigma}^{(s)}$ is for the simulation and $\boldsymbol{\Sigma}^{(\mathbf{r})}$ is for the experimental measurement. Testing if the covariance matrices of different groups of dataset are equal has been well studied, where the likelihood ratio test is the most commonly used methodology [169]. However, these studies focus on the covariance matrices of the observations, whose dimension would be very high for attenuation curves. Instead, we focus on the covariance matrix of model

parameters $(a_i, b_i)^T$ with significantly reduced dimension. Therefore the likelihood ratio test cannot be directly applied in this study. We employ the permutation test [170], a non-parametric and computationally efficient method to tackle this issue. Intuitively, if two sets of data (e.g., the acoustic attenuation curves from simulation and experimental measurements) are similar enough to each other, i.e., they come from the same distribution, then by randomly shuffling the data components between the two data sets, we expect to see the similar statistics (e.g., the difference of means or variances between the original two sets and the sets after random shuffling). We may now test how similar the two datasets by comparing the statistics before and after the random permutation. To make the comparison more rigorous, repeat the permutation process many times to get the sample distribution of the test statistic and calculate the p value for the statistic of the original data sets. An example of permutation test on testing means of two data sets is presented in Fig. Suppose we want to test if the means are equal for two datasets X_1 and X_2, which are generated from the same uniform distribution. The values in each set are randomly generated just for illustration purpose. By randomly shuffling the components in the two sets, we obtain X_1^* and X_2^*. The difference of the mean of the new sets is calculated. Repeat the permutation 1000 times to get the sample distribution of $\left|\overline{\mathrm{X}_1^*} - \overline{\mathrm{X}_2^*}\right|$. Calculate the p-value of test statistic of the original data sets. Here the p-value is the percentage of the generated 1000 samples that satisfy $\left|\overline{\mathrm{X}_1^*} - \overline{\mathrm{X}_2^*}\right| \geq |\overline{\mathrm{X}_1} - \overline{\mathrm{X}_2}|$. If the p-value is very small, it is likely that X_1 and X_2 have different means. In Fig the p-value is about 0.9, therefore the two means are likely to be equal.

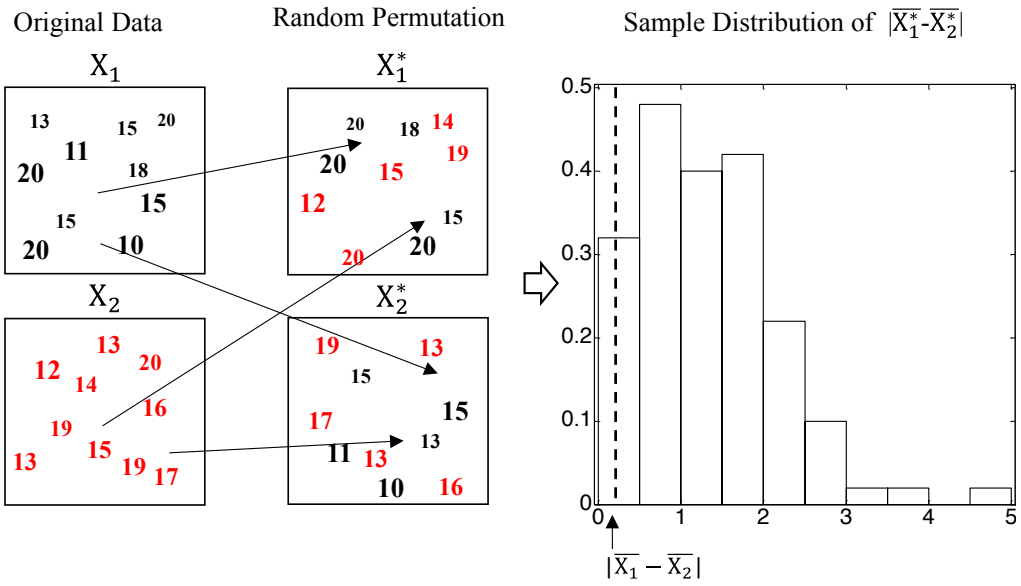

Fig 6-11 Illustration of permutation test on population means of two data sets.

In our case, the null hypothesis is $H_0: \mathbf{\Sigma}^{(s)} = \mathbf{\Sigma}^{(r)}$, which is equivalent to $H_0: \sigma_1^{(s)} = \sigma_1^{(r)}, \sigma_2^{(s)} = \sigma_2^{(r)}$, and $\rho^{(s)} = \rho^{(r)}$. In this testing there are simultaneously three components to be tested. To avoid the inconvenience of multiple testing problems [171], we reformulate it to an identical hypothesis testing $H_0: T = \max\left\{\left|\sigma_1^{(s)} - \sigma_1^{(r)}\right|, \left|\sigma_2^{(s)} - \sigma_2^{(r)}\right|, \left|\rho^{(s)} - \rho^{(r)}\right|\right\} = 0$. In other words, the hypothesis testing of equality of the two covariance matrices is performed by testing if the maximum difference of the matrix entries is zero. Considering that the sample variances of the three absolute differences in the testing statistic T may be different in the permutation test, it is necessary to standardize these three terms first by dividing their standard deviations (SD). Therefore the hypothesis test can be expressed as

$$H_0: T = \max\left\{\frac{\left|\sigma_1^{(s)} - \sigma_1^{(r)}\right|}{SD_{\left|\sigma_1^{(s)} - \sigma_1^{(r)}\right|}}, \frac{\left|\sigma_2^{(s)} - \sigma_2^{(r)}\right|}{SD_{\left|\sigma_2^{(s)} - \sigma_2^{(r)}\right|}}, \frac{\left|\rho^{(s)} - \rho^{(r)}\right|}{SD_{\left|\rho^{(s)} - \rho^{(r)}\right|}}\right\} = 0$$

$$H_1: T \neq 0$$

The permutation test can be summarized as: (1) random shuffle curves between the simulation set and the experimental measurement set and fit the linear mixed effects model to each new dataset to get $\boldsymbol{\Sigma}_{\boldsymbol{p}}^{(\mathbf{s})}$ and $\boldsymbol{\Sigma}_{\boldsymbol{p}}^{(\mathbf{r})}$; (2) calculate the absolute differences of σ_1, σ_2 and ρ between the two covariance matrices; (3) repeat (1) and (2) N_s times to obtain the three sets of samples for $\left|\sigma_1^{(s)} - \sigma_1^{(r)}\right|$, $\left|\sigma_2^{(s)} - \sigma_2^{(r)}\right|$ and $\left|\rho^{(s)} - \rho^{(r)}\right|$; (4) calculate their standard deviations and standardize these samples; (5) calculate the T statistic for these samples to obtain a set of samples $\{T_1, \dots, T_{N_s}\}$; (6) calculate the standardized T statistic for the observations (i.e., simulation set and experimental measurement before random shuffle) T_o; (7) calculate the p-value (the percentage of T samples that are larger than T_o) for the observations. If the p-value is smaller than a certain threshold, e.g., 0.1, then reject the null hypothesis H_0, i.e., $\boldsymbol{\Sigma}^{(\mathrm{s})} \neq \boldsymbol{\Sigma}^{(\mathrm{r})}$.

Fig shows two examples of the permutation test, where we compare the covariance matrices between Fig (c) (A206+5wt.% Al_2O_3) and Fig (c3), Fig (b) (A206+1wt.% Al_2O_3) and Fig (c3). The p-values for these two tests are 0.99 and 0.08 respectively. If we select the 0.1 as the testing threshold, then we can conclude that the variation of attenuation curves in Fig (b) is statistically different from Fig (c3), and Fig (c) is quite similar to Fig (c3) in terms of the between-curve variation. Also, we can use the p-value to evaluate the similarity of the covariance matrices of two sets of attenuation curves. The higher the p-value, the closer the two sets of attenuation curves. On the other hand, small p-values ($\leq$0.1) indicate a large difference between simulated attenuation curves and the experimental measurements due to mismatched microstructures. The p-value are 0.24, 0.71 and 0.99 for the comparisons between Fig (a) and Fig (a1), Fig (b) and Fig (b2), Fig (c)

and Fig (c3), respectively. These large p-values (>0.1) indicate that the simulated microstructures can well reproduce the attenuation variation.

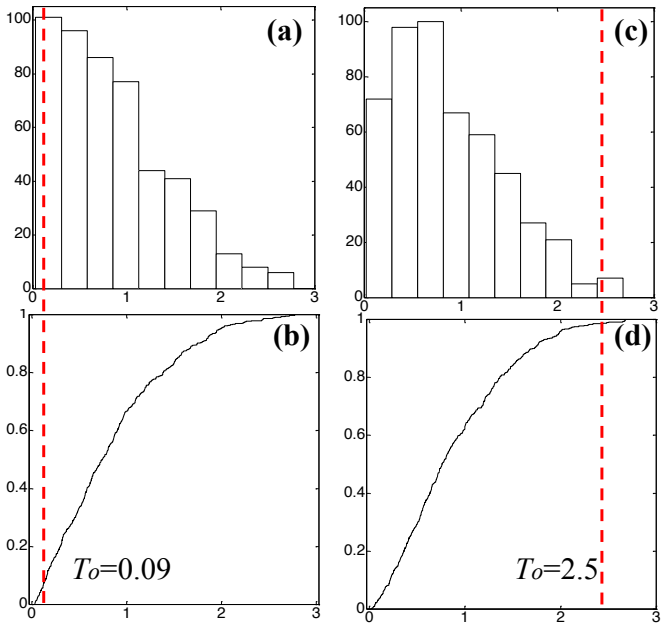

Fig 6-12 Illustration of the permutation test. (a) and (b): Fig (c) VS. Fig (c3), p-value=0.99; (c) and (d): Fig (b) VS. Fig (c3), p-value=0.06. The vertical dashed lines denote the observed test statistics.

Note that, the permutation test of T statistic calculated by LME can be applied for quality inspection of MMNCs. Because the consistency of the simulation results has been validated, the simulated acoustic attenuation curves are ready to be set as reference profiles. For example, the attenuation curves in Fig. 6-8 (c3) can be used as the reference of MMNCs with high quality. The measured attenuation curves from samples with low quality (e.g., Fig. 6-8 (b)) can be significantly identified by permutation test as shown in Fig. 6-12 (c) and (d).

6.6 Discussion and Conclusion

In this research, we propose a microstructure modelling and wave propagation simulation method to generate the microstructures and to simulate the ultrasonic attenuation curves for A206-Al_2O_3 MMNCs. Based on the micrographs and morphology modification mechanism of the nanocomposites, a modified Voronoi diagram is developed to simulate 2D microstructures and capture the microstructural features, where three key parameters are used to control the grain size of the primary phases and the morphology modification of the intermetallic phases. The numeric method EFIT is used to simulate the wave propagation through the generated microstructures. The attenuation curves are calculated by performing the fast Fourier transform (FFT) on the extracted signals from the outputs of EFIT. The simulated acoustic attenuation curves are quite consistent with the experimental measurements.

The linear mixed effects model is used to model the attenuation curves. A permutation test based on the maximum difference of each matrix entry is developed to test the equality of the covariance matrices from the simulated and experimental attenuation curves. The hypothesis tests show that by adjusting the microstructural parameters of the simulation, the simulated attenuation curves are able to closely match the experimental measurement in terms of the between-curve variations.

This research directly supports the experimental results and findings in [133] through the simulation approach. It helps us better understand the phenomenon of the non-uniformity of the attenuation curves and how the microstructural features influence this non-uniformity. In the future, the quantitative model will be conducted to infer the microstructural features based on the experimental and simulation database of different microstructures and the corresponding attenuations. Using that model, the statistical process control (SPC) charts will be developed to

control the quality of A206-Al_2O_3 MMNCs based on the attenuation profiles or inferred microstructural features. Although 2D simulation has been commonly used, it may be not as accurate as 3D simulations. Therefore it is desirable to extend the simulation to three dimensions to better represent the experimental microstructures and wave propagation processes, which will also be our future work.

6.7 Appendix : EFIT equations and resolution conditions

The 2D EFIT equations of (5.1) and (5.2) are presented as

$$v_{x,i,j}^{n} = v_{x,i,j}^{n-1} + \frac{\Delta t}{\Delta x} B_x \left(\tau_{xx,i+1,j}^{n-\frac{1}{2}} - \tau_{xx,i,j}^{n-\frac{1}{2}} + \tau_{xy,i,j}^{n-\frac{1}{2}} - \tau_{xy,i,j-1}^{n-\frac{1}{2}} \right), \tag{6.5}$$

$$v_{y,i,j}^{n} = v_{y,i,j}^{n-1} + \frac{\Delta t}{\Delta x} B_y \left(\tau_{xy,i,j}^{n-\frac{1}{2}} - \tau_{xy,i-1,j}^{n-\frac{1}{2}} + \tau_{yy,i,j+1}^{n-\frac{1}{2}} - \tau_{yy,i,j}^{n-\frac{1}{2}} \right), \tag{6.6}$$

$$\begin{aligned} \tau_{xx,i,j}^{n+\frac{1}{2}} = \tau_{xx,i,j}^{n-\frac{1}{2}} + \frac{\Delta t}{\Delta x} \{ & (\lambda + 2\mu) \left[v_{x,i,j}^{n} - v_{x,i-1,j}^{n} \right] + \lambda \left[v_{y,i,j}^{n} - v_{y,i,j-1}^{n} \right] \\ & + (\eta + 2\phi) \left[\dot{v}_{x,i,j}^{n} - \dot{v}_{x,i-1,j}^{n} \right] + \eta \left[\dot{v}_{y,i,j}^{n} - \dot{v}_{y,i,j-1}^{n} \right], \end{aligned} \tag{6.7}$$

$$\begin{aligned} \tau_{yy,i,j}^{n+\frac{1}{2}} = \tau_{yy,i,j}^{n-\frac{1}{2}} + \frac{\Delta t}{\Delta x} \{ & (\lambda + 2\mu) \left[v_{y,i,j}^{n} - v_{y,i-1,j}^{n} \right] + \lambda \left[v_{x,i,j}^{n} - v_{x,i,j-1}^{n} \right] \\ & + (\eta + 2\phi) \left[\dot{v}_{y,i,j}^{n} - \dot{v}_{y,i-1,j}^{n} \right] + \eta \left[\dot{v}_{x,i,j}^{n} - \dot{v}_{x,i,j-1}^{n} \right], \end{aligned} \tag{6.8}$$

$$\begin{aligned} \tau_{xy,i,j}^{n+\frac{1}{2}} = \tau_{xy,i,j}^{n-\frac{1}{2}} + \frac{\Delta t}{\Delta x} \{ & \mu_{xy} \left[v_{x,i,j+1}^{n} - v_{x,i,j}^{n} + v_{y,i+1,j}^{n} - v_{y,i,j}^{n} \right] \\ & + \upsilon_{xy} \left[\dot{v}_{x,i,j+1}^{n} - \dot{v}_{x,i,j}^{n} + \dot{v}_{y,i+1,j}^{n} - \dot{v}_{y,i,j}^{n} \right], \end{aligned} \tag{6.9}$$

where the velocities (v_x, v_y) at time n are calculated using the sum of the velocities at time $n-1$ and a linear combination of the stresses $(\tau_{xx}, \tau_{yy}, \tau_{xy})$ in the spatial coordinates i, j and the half step time $n - \frac{1}{2}$. Similarly, the stresses $(\tau_{xx}, \tau_{yy}, \tau_{xy})$ at time $n + \frac{1}{2}$ are calculated by adding the

stresses at $n-\frac{1}{2}$ and the linear combination of velocities multiplied by the lame constants λ and μ for the elastic factor and the viscous factor η and ϕ multiplied by the rate of change in velocities (denoted as $(\dot{v}_x, \dot{v}_y)$). Δx and Δt represent spatial step and time step respectively. B_x and B_y are the effective buoyancies defined as :

$$B_x = \frac{2}{\rho_{i+1,j} + \rho_{i,j}},$$

$$B_y = \frac{2}{\rho_{i,j+1} + \rho_{i,j}},$$

where ρ is the mass density for the spatial coordinates i, j. μ_{xy} and υ_{xy} are the effective rigidity defined as :

$$\mu_{xy} = \frac{4}{\frac{1}{\mu_{i,j}} + \frac{1}{\mu_{i+1,j}} + \frac{1}{\mu_{ij+1}} + \frac{1}{\mu_{i+1.j+1}}},$$

$$\upsilon_{xy} = \frac{4}{\frac{1}{\phi_{i,j}} + \frac{1}{\phi_{i+1,j}} + \frac{1}{\phi_{ij+1}} + \frac{1}{\phi_{i+1.j+1}}}.$$

The spatial resolution Δx and the time resolution Δt must be chosen small enough to provide sufficiently smooth representations of the computed filed. However, these two resolutions cannot be chosen independently, they must satisfy the Courant's stability condition, that is:

$$\Delta t \leq \frac{\Delta x}{c_{max}\sqrt{d}},$$

where d is the space dimension ($d = 2$ is used for our simulation) and c_{max} is the largest wave speed in the media. Δx is recommended ranging from $\frac{\lambda}{8}$ to $\frac{\lambda}{20}$ for the wavelength λ [172].

7 Conclusion and Future Work

Fault detection and prognosis play important role in the engineering systems. In structures an early detection of faults in mechanical structures ensures the safety and avoids any potential damages. Precise prognosis of the fault progression make the timely maintenance and reparation possible. In manufacturing processes, early detection of nonconforming parts or products with low qualities leads early corrective actions to ensure consistent delivery of a quality product and to avoid productivity loss. The research presented in this dissertation aimed to quantitatively address several fundamental and significant issues that remain in the areas of structural fault detection and prognosis, and fault detection of specific data types in manufacturing process.

In the study of mechanical structures, the identifiability issue of FEM, the measurement selection algorithm for bias reduction and structural property degradation are investigated. Specifically,

1) The identifiability issue in FEM for fault detection is addressed by a quantitative framework. FEM of a beam structure is re-formulated into a state space model representing LTI dynamic system. By using the properties of an inverse of a block diagonal matrix, the uniqueness of the system transfer function is proven for different severity level of damages at the same location. That is, the damages are theoretically identifiable in the FEM for a given damage location of a beam structure. Moreover, a sufficient condition for the identifiability of multiple damages at different locations is established based on the natural frequencies. A numerical algorithm is proposed to numerically check and validate the location identifiability of scalar valued damage location. With this checking procedure, it is showed that damages at two different locations will only result in the same transfer function under the symmetric conditions. In other words, two

damages at different locations will be differentiable in most cases. The algorithm can be extended for vector valued damage. Several representative case studies are conducted to demonstrate the effectiveness and usefulness of the proposed framework for providing a theoretical guideline on the damage identifiability by using FEM-based vibration analysis.

2) A natural frequency selection algorithm is proposed to reduce the bias in the estimation of damage parameters using linear approximation under mild damage scenarios. The selected combination of natural frequency has high probability to be the optimal combination which leads to the smallest bias in the estimation among all the possible combinations. The algorithm consists three sub-algorithms. In the first algorithm, the L_1- norm regularization with iterative matrix randomization is adopted for estimation of damage parameters followed by a majority voting process. In the second algorithm, the damage locations are identified by sequential updating. The improved estimation L_1- IMR helps to choose the best combination of measurements in the third algorithm. The effectiveness of the proposed method is validated through numerical studies. Factors that influence the performance of the method are also discussed.

3) The progression of stiffness loss is predicted by the dynamic data-driven hierarchical Bayesian degradation model. The model adopts a two level hierarchical structure. In the first level, the observed natural frequencies are assumed to be generated from a normal distribution with given stiffness. In the second level, the evolving path of stiffness is described using polynomial functions. The unknown parameters in the model are described by conditional posterior distribution in Bayesian framework and estimated by Gibbs sampling method. Numerical studies and results are used to validate the model for different evolving path of stiffness loss. The model performed efficiently in all cases.

For two specific data types in manufacturing process, the following data analytics models and methods are adopted for fault detection.

1) A HT-based method to detect point patterns that consist of arbitrary line segments is proposed for detecting defects distributed as spatial point pattern in semiconductor wafers. The basic idea is to convert the line pattern detection problem in physical domain into the problem of detecting multiple points in Hough domain. The detection is attained through two critical steps, the angle matching and the distance matching, which allows arbitrary rotation, scaling, and translation of the pattern. Based on the simple intuition that a line is most likely to be detected if a Hough strip fully overlaps with the defective region, a detailed discussion on how to select tuning parameters of the algorithm are provided. An extensive numerical study shows that the detection method performance well in terms of both Type I error and the detection power if the defective region has reasonable size and the contrast between the defective region and the background noise is reasonably large.

2) Linear mixed effect model and permutation test are adopted to analyze the variation of acoustics attenuation curves for quality inspection of A206-Al2O3 MMNCs. The acoustic attenuation curves are characterized by linear mixed effect model, where the model parameters are estimated using MLE method. The variance model parameters are formed as T statistic to test the null hypothesis by permutation test. In addition, a microstructure modelling and wave propagation simulation method to generate the microstructures and to simulate the ultrasonic attenuation curves for A206-Al2O3 MMNCs is proposed, where the microstructures are modelled by Voronoi diagram and wave propagation is simulated by numerical calculation of EFIT. The statistical analysis shows the consistency of the simulation results with the experimental results. By such

simulation model, the understanding of the wave-microstructure interaction is enhanced, while providing a flexible platform for further quantitative analysis.

Future work will focus on fault identification based on the framework of integrating piezoelectric transducer circuitry (PTC) network into mechanical structures. The PTC enhances the performance of frequency-shift-based damage identification method. However, a quantitative analysis on the tuning variable of the network is lacking of studies. For instance, how to tune the inductance in the circuit to make the most sensitive damage detection and how to quantify the accuracy of detection results as function of the amount of tuning variables. These issues are planned to be investigated before the final defense.

Some potential future directions are summarized in the following.

1) *On-line change point detection in structural monitoring:* As discussed in Chapter 3, the trend of structural property degradation may follow beta function trend, where the rapid decrease of structural property happens at certain time point. It is important to detect such changing time point accurately and quickly to prevent further potential damages of the structures.
2) *Adaptive fault identification methodology:* The monitoring signals carry the information of engineering systems under certain environmental factors. The environmental factors may influence the systems in a dramatic way, in which case, the analysis of signals ignoring the environmental effects leads unreliable results. Methods that incorporate the impacts of the environment are needed for precise fault identification.

8 References

[1] Staszewski, Wieslaw, Chr Boller, and Geoffrey R. Tomlinson, eds. Health monitoring of aerospace structures: smart sensor technologies and signal processing. John Wiley & Sons, 2004.

[2] Peeters, Bart. "System identification and damage detection in civil engineering." Department of Civil Engineering, Katholieke Universiteit Leuven, Leuven (2000): 233.

[3] Ellyin, Fernand. Fatigue damage, crack growth and life prediction. Springer Science & Business Media, 2012.

[4] Wang, Lihui, and Robert X. Gao, eds. Condition monitoring and control for intelligent manufacturing. Springer Science & Business Media, 2006.

[5] Tzafestas, Spyros G., ed. Knowledge-based system diagnosis, supervision, and control. Springer Science & Business Media, 2013.

[6] Ling, You, and Sankaran Mahadevan. "Integration of structural health monitoring and fatigue damage prognosis." Mechanical Systems and Signal Processing 28 (2012): 89-104.

[7] Sankararaman, Shankar, et al. "Uncertainty quantification in fatigue damage prognosis."

[8] Ding, Yu, Dariusz Ceglarek, and Jianjun Shi. "Modeling and diagnosis of multistage manufacturing processes: part I: state space model." Proceedings of the 2000 Japan/USA symposium on flexible automation. 2000.

[9] Camelio, Jaime, S. Jack Hu, and Dariusz Ceglarek. "Modeling variation propagation of multi-station assembly systems with compliant parts." Journal of Mechanical Design 125.4 (2003): 673-681.

[10] Haghighi, Firoozeh, Nazanin Nooraee, and Narges Nazeri Rad. "On the general degradation path model: Review and simulation." Advances in Degradation Modeling. Birkhäuser Boston, 2010. 147-155.

[11] Rammohan, Roshan, and Mahmoud Reda Taha. "Exploratory investigations for intelligent damage prognosis using hidden Markov models." Systems, Man and Cybernetics, 2005 IEEE International Conference on. Vol. 2. IEEE, 2005.

[12] Zaidi, Syed Sajjad H., et al. "Prognosis of gear failures in dc starter motors using hidden Markov models." Industrial Electronics, IEEE Transactions on 58.5 (2011): 1695-1706.

[13] Dey, Story, and J. A. Stori. "A Bayesian network approach to root cause diagnosis of process variations." International Journal of Machine Tools and Manufacture 45.1 (2005): 75-91.

[14] Kresta, James V., John F. MacGregor, and Thomas E. Marlin. "Multivariate statistical monitoring of process operating performance." The Canadian Journal of Chemical Engineering 69.1 (1991): 35-47.

[15] Joe Qin, S. "Statistical process monitoring: basics and beyond." Journal of chemometrics 17.8-9 (2003): 480-502.

[16] Hamzeloo, S. R., Shamshirsaz, M., & Rezaei, S. M. (2012). Damage detection on hollow cylinders by electro-mechanical impedance method: experiments and finite element modeling. *Comptes Rendus Mecanique*, 340(9), 668-677.

[17] Stubbs, Norris, Taft H. Broome, and Roberto Osegueda, Nondestructive construction error detection in large space structures. AIAA journal 28.1 (1990): 146-152.

[18] Stubbs, Norris, and Robert Osegueda, Global non-destructive damage evaluation in solids. International Journal of Analytical and Experimental Modal Analysis 5 (1990): 67-79.

[19] Stubbs, Norris, and Robert Osegueda, Global damage detection in solids-Experimental verification. International Journal of Analytical and Experimental Modal Analysis 5 (1990): 81-97.

[20] Shiradhonkar, S. R., & Shrikhande, M. (2011). Seismic damage detection in a building frame via finite element model updating. *Computers & Structures*, 89(23), 2425-2438.

[21] Mayes, Randy. Error localization using mode shapes: An application to a two link robot arm. No. SAND-91-2297C; CONF-920234--1. Sandia National Labs., Albuquerque, NM (United States), 1991.

[22] Jafarkhani, R., & Masri, S. F. (2011). Finite element model updating using evolutionary strategy for damage detection. *Computer-Aided Civil and Infrastructure Engineering*, 26(3), 207-224.

[23] Lee, J. J., Lee, J. W., Yi, J. H., Yun, C. B., & Jung, H. Y. (2005). Neural networks-based damage detection for bridges considering errors in baseline finite element models. *Journal of Sound and Vibration*, 280(3), 555-578.

[24] Wu, J. R., & Li, Q. S. (2006). Structural parameter identification and damage detection for a steel structure using a two-stage finite element model updating method. *Journal of Constructional Steel Research*, 62(3), 231-239.

[25] Pandey, A. K., M. Biswas, and M. M. Samman, Damage detection from changes in curvature mode shapes. Journal of sound and vibration 145.2 (1991): 321-332.

[26] Chen, Jay-Chung, and John A. Garba, On-orbit damage assessment for large space structures. AIAA journal 26.9 (1988): 1119-1126.

[27] Chen, Jay-Chung, and John A. Garba, Structural damage assessment using a system identification technique. Structural safety evaluation based on system identification approaches. Vieweg+ Teubner Verlag, 1988. 474-492.

[28] Sanayei, Masoud, and Oladipo Onipede, Damage assessment of structures using static test data. AIAA journal 29.7 (1991): 1174-1179.

[29] Sanayei, Masoud, Oladipo Onipede, and Suresh R. Babu, Selection of noisy measurement locations for error reduction in static parameter identification. AIAA journal 30.9 (1992): 2299-2309.

[30] Liu, Pei-Ling, Identification and damage detection of trusses using modal data. Journal of Structural Engineering 121.4 (1995): 599-608.

[31] Lim, T. W., A Submatrix Approach To Stiffness Using Modal Test Data, AIAA Journal , 1990 Vol. 28, No. 6, pp. 1123–1130.

[32] Lim, T. W., Structural Damage Detection Using Modal Test Data, AIAA Journal, 1991 Vol.29, No. 12, pp. 2271–2274.

[33] Lim, T. W., Structural Damage Detection of a Planar Truss Structure Using a Constrained Eigenstructure Assignment, in Proc. of 35th AIAA/ASME/ ASCE/AHS/ASC Structures, Structural Dynamics and Materials Conf., 1994,AIAA-94-1715-CP, pp. 336–346.

[34] Zimmerman, David C., and Mohammed Kaouk. Structural damage detection using a minimum rank update theory. Journal of Vibration and Acoustics 116.2 (1994): 222-231.

[35] Zimmerman, David C., Todd Simmermacher, and Mohamed Kaouk. Structural damage detection using frequency response functions. Proceedings of the 13th International Modal Analysis Conference. Vol. 2460. 1995.

[36] Zimmerman, D. C., M. Kaouk, and T. Simmermacher. On the role of engineering insight and judgement structural damage detection. Proceedings of the 13th International Modal Analysis Conference. Vol. 2460. 1995.

[37] Chang, Jin-De, and Bao-Zhu Guo. Identification of variable spacial coefficients for a beam equation from boundary measurements. Automatica 43.4 (2007): 732-737.

[38] Ju, Frederick D., et al. Diagnosis of Fracture Damage in Simple Structures: A Modal Method. No. CE-62 (82) AFOSR-993-1. NEW MEXICO UNIV ALBUQUERQUE BUREAU OF ENGINEERING RESEARCH, 1982.

[39] Nguyen, V. V., and E. F. Wood. Review and unification of linear identifiability concepts. SIAM review 24.1 (1982): 34-51.

[40] Franco, G., Betti, R., & Longman, R. W. (2006). On the uniqueness of solutions for the identification of linear structural systems. Journal of applied Mechanics, 73(1), 153-162.

[41] De Angelis, M., Lus, H., Betti, R., & Longman, R. W. (2002). Extracting physical parameters of mechanical models from identified state-space representations. Journal of applied mechanics, 69(5), 617-625.

[42] Sun, H., Luş, H., & Betti, R. (2013). Identification of structural models using a modified Artificial Bee Colony algorithm. Computers & Structures, 116, 59-74.

[43] Reynders, E. (2012). System identification methods for (operational) modal analysis: review and comparison. Archives of Computational Methods in Engineering, 19(1), 51-124.

[44] Simani, S., Fantuzzi, C., & Patton, R. J. (2013). Model-based fault diagnosis in dynamic systems using identification techniques. Springer Science & Business Media.

[45] Rugh, Wilson J. Linear system theory. Vol. 2. Upper Saddle River, NJ: prentice hall, 1996.

[46] Segerlind, L. J., & Saunders, H. (1987). Applied finite element analysis.

[47] Meurant, Gérard. A review on the inverse of symmetric tridiagonal and block tridiagonal matrices. SIAM Journal on Matrix Analysis and Applications 13.3 (1992): 707-728.

[48] Nabben, Reinhard. Decay rates of the inverse of nonsymmetric tridiagonal and band matrices. SIAM Journal on Matrix Analysis and Applications 20.3 (1999): 820-837.

[49] Demko, Stephen, William F. Moss, and Philip W. Smith. Decay rates for inverses of band matrices. Mathematics of computation 43.168 (1984): 491-499.

[50] Eijkhout, Victor, and Ben Polman. Decay rates of inverses of banded M-matrices that are near to Toeplitz matrices. Linear Algebra and its Applications 109 (1988): 247-277.

[51] Yamamoto, Tetsuro, and Yasuhiko Ikebe. Inversion of band matrices. Linear Algebra and Its Applications 24 (1979): 105-111.

[52] Balageas, Daniel, Claus-Peter Fritzen, and Alfredo Güemes, eds. Structural health monitoring. Vol. 493. London: ISTE, 2006.

[53] Wang, S. Q., & Li, H. J. (2012). Assessment of structural damage using natural frequency changes. *Acta Mechanica Sinica*, 28(1), 118-127.

[54] Salawu, O. S. (1997). Detection of structural damage through changes in frequency: a review. *Engineering structures*, 19(9), 718-723.

[55] Lo, S. S., Philippe, B., & Sameh, A. (1987). A multiprocessor algorithm for the symmetric tridiagonal eigenvalue problem. *SIAM Journal on Scientific and Statistical Computing*, 8(2), s155-s165.

[56] Trefftz, C., Huang, C. C., McKinley, P. K., Li, T. Y., & Zeng, Z. (1995). A scalable eigenvalue solver for symmetric tridiagonal matrices. *Parallel Computing*, 21(8), 1213-1240.

[57] Fernandez, F. A., Davies, J. B., Zhu, S., & Lu, Y. (1991). Sparse matrix eigenvalue solver for finite element solution of dielectric waveguides. *Electronics Letters*, 27(20), 1824-1826.

[58] Gruber, R. (1980). HYMNISBLOCK—Eigenvalue solver for blocked matrices. *Computer Physics Communications*, 20(3), 421-428.

[59] Demmel, J. W., Marques, O. A., Parlett, B. N., & Vömel, C. (2008). Performance and accuracy of LAPACK's symmetric tridiagonal eigensolvers. *SIAM Journal on Scientific Computing*, 30(3), 1508-1526.

[60] Peng, D., Middendorf, N., Weigend, F., & Reiher, M. (2013). An efficient implementation of two-component relativistic exact-decoupling methods for large molecules. *The Journal of chemical physics*, 138(18), 184105.

[61] Beyn, W. J. (2012). An integral method for solving nonlinear eigenvalue problems. *Linear Algebra and Its Applications*, 436(10), 3839-3863.

[62] Davidson, G. G., Evans, T. M., Jarrell, J. J., Hamilton, S. P., Pandy, T. M., & Slaybaugh, R. N. (2014). Massively parallel, three-dimensional transport solutions for the k-eigenvalue problem. *Nuclear Science and Engineering*, 177(2), 111-125.

[63] Barrett, Wayne W. A theorem on inverse of tridiagonal matrices. Linear Algebra and Its Applications 27 (1979): 211-217.

[64] Engwerda, Jacob C., AndréC M. Ran, and Arie L. Rijkeboer. Necessary and sufficient conditions for the existence of a positive definite solution of the matrix equation X+ A∗ X-1A= Q. Linear Algebra and its Applications 186 (1993): 255-275.

[65] Adams, R. D., et al. A vibration technique for non-destructively assessing the integrity of structures. Journal of Mechanical Engineering Science 20.2 (1978): 93-100.

[66] Qian, G-L., S-N. Gu, and J-S. Jiang. The dynamic behaviour and crack detection of a beam with a crack. Journal of Sound and Vibration 138.2 (1990): 233-243.

[67] Gillich, Gilbert-Rainer, et al. The relationship between changes of deflection and natural frequencies of damaged beams.

[68] Hearn, George, and Rene B. Testa. Modal analysis for damage detection in structures. Journal of Structural Engineering 117.10 (1991): 3042-3063.

[69] Hassiotis, S. Identification of damage using natural frequencies and Markov parameters. Computers & Structures 74.3 (2000): 365-373.

[70] Li, R. C. (2013). Rayleigh Quotient Based Optimization Methods For Eigenvalue Problems. Summary of Lectures Delivered at Gene Golub SIAM Summer School.

[71] Kato, T. (2012). Perturbation theory for linear operators. Springer Science & Business Media.

[72] Doebling, Scott W., Charles R. Farrar, and Michael B. Prime. "A summary review of vibration-based damage identification methods." Shock and vibration digest 30.2 (1998): 91-105.

[73] Farrar, Charles R., Scott W. Doebling, and David A. Nix. "Vibration–based structural damage identification." Philosophical Transactions of the Royal Society of London A: Mathematical, Physical and Engineering Sciences 359.1778 (2001): 131-149.

[74] Sobczyk, Kazimierz, and B. F. Spencer Jr. Random fatigue: from data to theory. Academic Press, 2012.

[75] Luo, Jianhui, et al. "Model-based prognostic techniques [maintenance applications]." AUTOTESTCON 2003. IEEE Systems Readiness Technology Conference. Proceedings. IEEE, 2003.

[76] Li Y, Billington S, Zhang C, Kurfess T, Danyluk S, Liang S (1999) Adaptive prognostics for rolling element bearing condition. Mech Sys Signal Process 13:103–113

[77] Nechval, Nicholas, et al. "Stochastic fatigue models for efficient planning inspections in service of aircraft structures." Analytical and stochastic modeling techniques and applications. Springer Berlin Heidelberg, 2008. 114-127.

[78] Madsen, Henrik O., Steen Krenk, and Niels Christian Lind. Methods of structural safety. Courier Corporation, 2006.

[79] Spencer Jr, B. F., and J. Tang. "Markov process model for fatigue crack growth." Journal of engineering mechanics 114.12 (1988): 2134-2157.

[80] Lin, Y. K., W. F. Wu, and J. N. Yang. "Stochastic modeling of fatigue crack propagation." Probabilistic Methods in the Mechanics of Solids and Structures. Springer Berlin Heidelberg, 1985. 103-110.

[81] Ray, Asok, and Shashi Phoha. "Stochastic modeling of fatigue crack damage for information-based maintenance." Annals of Operations Research 91 (1999): 191-204.

[82] Haghighi, Firoozeh, Nazanin Nooraee, and Narges Nazeri Rad. "On the general degradation path model: Review and simulation." Advances in Degradation Modeling. Birkhäuser Boston, 2010. 147-155.

[83] Ye, Zhi-Sheng, et al. "Degradation data analysis using Wiener processes with measurement errors." Reliability, IEEE Transactions on 62.4 (2013): 772-780.

[84] Friswell, Michael, and John E. Mottershead. Finite element model updating in structural dynamics. Vol. 38. Springer Science & Business Media, 1995.

[85] Freer, Jim, Keith Beven, and Bruno Ambroise. "Bayesian estimation of uncertainty in runoff prediction and the value of data: An application of the GLUE approach." Water Resources Research 32.7 (1996): 2161-2173.

[86] Berger, James O. Statistical decision theory and Bayesian analysis. Springer Science & Business Media, 2013.

[87] Si, Xiao-Sheng, et al. "Remaining useful life estimation–a review on the statistical data driven approaches." European Journal of Operational Research 213.1 (2011): 1-14.

[88] Charles R. Farrar and Nick A.J. Lieven. "Damage prognosis: the future of structural health monitoring." Philosophical Transactions: Mathematical, Physical and Engineering Sciences 365.1851(2007): 623-632

[89] Charles R. Farrar, Francois M. Hemez, Gyuhae Park, Amy N. Robertson, Sohn, Hoon and Todd O. Williams. "A coupled approach to developing damage prognosis solutions." Key Engineering Materials, 245.246(2003): 289-306.

[90] Rasouli, Asghar, Seyed Sina Kourehli, Gholamreza Ghodrati Amiri, and Ali Kheyroddin. "A two-stage method for structural damage prognosis in shear frames based on story displacement index and modal residual force." Advances in civil engineering 2015 (2015).

[91] Salawu, O. S. "Detection of structural damage through changes in frequency: a review." Engineering structures 19.9 (1997): 718-723.

[92] Wilkinson, James Hardy. The algebraic eigenvalue problem. Vol. 87. Oxford: Clarendon Press, 1965.

[93] Schijve, Jaap. Fatigue of structures and materials. Dordrecht: Kluwer Academic, 2001.

[94] Press, S. James, and James S. Press. Bayesian statistics: principles, models, and applications. New York: Wiley, 1989.

[95] Jeffreys, Harold. Scientific inference. Cambridge University Press, 1973.

[96] Gelfand, Alan E., et al. "Illustration of Bayesian inference in normal data models using Gibbs sampling." Journal of the American Statistical Association 85.412 (1990): 972-985.

[97] Gamerman, Dani, and Hedibert F. Lopes. Markov chain Monte Carlo: stochastic simulation for Bayesian inference. CRC Press, 2006.

[98] Neal, Radford M. "Slice sampling." Annals of statistics (2003): 705-741.

[99] Bozdogan, Hamparsum. "Model selection and Akaike's information criterion (AIC): The general theory and its analytical extensions." Psychometrika 52.3 (1987): 345-370.

[100] Burnham, Kenneth P., and David R. Anderson. "Multimodel inference understanding AIC and BIC in model selection." Sociological methods & research 33.2 (2004): 261-304.

[101] Ansari, Asim, and Kamel Jedidi. "Bayesian factor analysis for multilevel binary observations." Psychometrika 65.4 (2000): 475-496.

[102] Spiegelhalter, David J., et al. "Bayesian measures of model complexity and fit." Journal of the Royal Statistical Society: Series B (Statistical Methodology) 64.4 (2002): 583-639.

[103] GILLICH, GILBERT-RAINER, et al. "The relationship between changes of deflection and natural frequencies of damaged beams."

[104] Melbourne, Clive, ed. Arch Bridges: Proceedings of the First International Conference on Arch Bridges, Held at Bolton, UK on 3-6 September 1995. Thomas Telford, 1995.

[105] AISI, Steel industry technology roadmap, American Iron and Steel Institute., Washington D.C, 2001.

[106] Guldi, R. L. (2004). In-line defect reduction from a historical perspective and its implications for future integrated circuit manufacturing. *Semiconductor Manufacturing, IEEE Transactions on*, *17*(4), 629-640.

[107] Gao, S. L., Mäder, E., & Plonka, R. (2008). Nanocomposite coatings for healing surface defects of glass fibers and improving interfacial adhesion.*Composites Science and Technology*, *68*(14), 2892-2901

[108] A. Busnaina, Micro & nanoscale defects in micro & nanofabrication, ASME Continuing Education Institute Programs, New York, 2001.

[109] Yang, Y., & Li, X. (2007). Ultrasonic cavitation based nanomanufacturing of bulk aluminum matrix nanocomposites. *Journal of manufacturing science and engineering*, *129*(3), 497-501.

[110] Zhang, Z., & Chen, D. L. (2008). Contribution of Orowan strengthening effect in particulate-reinforced metal matrix nanocomposites. *Materials Science and Engineering: A*, *483*, 148-152

[111] Hansen, M. H., Nair, V. N., & Friedman, D. J. (1997). Monitoring wafer map data from integrated circuit fabrication processes for spatially clustered defects. *Technometrics*,*39*(3), 241-253

[112] Hwang, J. Y., & Kuo, W. (2007). Model-based clustering for integrated circuit yield enhancement. *European Journal of Operational Research*, *178*(1), 143-153.

[113] D. C. Montgomery, Introduction to Statistical Quality Control, 5th ed. Hoboken, NJ: Wiley, 2005.

[114] Spanos, C. J. (1992). Statistical process control in semiconductor manufacturing. *Proceedings of the IEEE*, *80*(6), 819-830.

[115] Friedman, D. J., Hansen, M. H., Nair, V. N., & James, D. A. (1997). Model-free estimation of defect clustering in integrated circuit fabrication. *Semiconductor Manufacturing, IEEE Transactions on*, *10*(3), 344-359.

[116] Jeong, Y. S., Kim, S. J., & Jeong, M. K. (2008). Automatic identification of defect patterns in semiconductor wafer maps using spatial correlogram and dynamic time warping. *Semiconductor Manufacturing, IEEE Transactions on*,*21*(4), 625-637

[117] Lee, F., Chatterjee, A., & Croley, D. (1996, November). Advanced yield enhancement: computer-based spatial pattern analysis. Part 1. In *Advanced Semiconductor Manufacturing Conference and Workshop, 1996. ASMC 96 Proceedings. IEEE/SEMI 1996* (pp. 409-415). IEEE..

[118] Karnowski, T. P., Tobin Jr, K. W., Gleason, S. S., & Lakhani, F. (1999, June). Application of spatial signature analysis to electrical test data: validation study. In *Microlithography'99* (pp. 530-541). International Society for Optics and Photonics

[119] Tobin, K. W., Gleason, S. S., Lakhani, F. R. E. D., & Bennett, M. H. (1997). Automated analysis for rapid defect sourcing and yield learning. *Future Fab International*, *4*, 313

[120] Chen, F. L., & Liu, S. F. (2000). A neural-network approach to recognize defect spatial pattern in semiconductor fabrication. *Semiconductor Manufacturing, IEEE Transactions on*, *13*(3), 366-373.

[121] Duda, R. O., & Hart, P. E. (1972). Use of the Hough transformation to detect lines and curves in pictures. *Communications of the ACM*, *15*(1), 11-15.

[122] Wang, C. H., Wang, S. J., & Lee, W. D. (2006). Automatic identification of spatial defect patterns for semiconductor manufacturing. *International journal of production research*, *44*(23), 5169-5185

[123] Wang, C. H. (2008). Recognition of semiconductor defect patterns using spatial filtering and spectral clustering. *Expert Systems with Applications*, *34*(3), 1914-1923.

[124] Wang, C. H. (2009). Separation of composite defect patterns on wafer bin map using support vector clustering. *Expert Systems with Applications*, *36*(2), 2554-2561.

[125] Yuan, T., & Kuo, W. (2007). A model-based clustering approach to the recognition of the spatial defect patterns produced during semiconductor fabrication. *IIE Transactions*, *40*(2), 93-101

[126] Yuan, T., & Kuo, W. (2008). Spatial defect pattern recognition on semiconductor wafers using model-based clustering and Bayesian inference.*European Journal of Operational Research*, *190*(1), 228-240.

[127] Zhou, Q., Zeng, L., & Zhou, S. (2010). Statistical detection of defect patterns using Hough transform. *Semiconductor Manufacturing, IEEE Transactions on*,*23*(3), 370-380.

[128] DeNicolao, G., Pasquinetti, E., Miraglia, G., & Piccinini, F. (2003, September). Unsupervised spatial pattern classification of electrical failures in semiconductor manufacturing. In *Artificial Neural Nets. Pattern Recognit. Workshop* (pp. 125-131).

[129] Yuen, S. Y., & Ma, C. H. (1996, August). An investigation of the nature of parametrization for the Hough transform. In *Pattern Recognition, 1996., Proceedings of the 13th International Conference on* (Vol. 2, pp. 537-541). IEEE

[130] Ballard, D. H. (1981). Generalizing the Hough transform to detect arbitrary shapes. *Pattern recognition*, *13*(2), 111-122

[131] Choi, H., Cho, W.-h., Konishi, H., Kou, S., and Li, X., 2013, "Nanoparticle-Induced Superior Hot Tearing Resistance of A206 Alloy," Metallurgical and Materials Transactions A, pp. 1-11.

[132] Wu, J., Zhou, S., and Li, X., 2013, "Acoustic Emission Monitoring for Ultrasonic Cavitation Based Dispersion Process," Journal of Manufacturing Science and Engineering, 135(3), pp. 031015-031015.

[133] Wu, J., Zhou, S., and Li, X., 2015, "Ultrasonic Attenuation Based Inspection Method for Scale-up Production of A206–Al2O3 Metal Matrix Nanocomposites," Journal of Manufacturing Science and Engineering, 137(1), p. 011013.

[134] Sun, Y., 2012, "Microstructure modification by nanoparticles in aluminum and magnesium matrix nanocomposites," Master Master's thesis, University of Wisconsin--Madison.

[135] Yang, Y., and Li, X., 2007, "Ultrasonic cavitation-based nanomanufacturing of bulk aluminum matrix nanocomposites," Journal of Manufacturing Science and Engineering, 129(2), pp. 252-255.

[136] Li, X., Yang, Y., and Weiss, D., 2008, "Theoretical and experimental study on ultrasonic dispersion of nanoparticles for strengthening cast Aluminum Alloy A356," Met. Sci. Technol, 26(2), pp. 12-20.

[137] Drury, J. C., 2004, Ultrasonic flaw detection for technicians, Silverwing Limited.

[138] Ying, Y., 2012, "A Data-Driven Framework for Ultrasonic Structural Health Monitoring of Pipes."

[139] Schmerr, L. W., 1998, Fundamentals of ultrasonic nondestructive evaluation: a modeling approach, Plenum Press New York.

[140] Krautkrämer, J., and Krautkrämer, H., 1990, "Ultrasonic testing of materials."

[141] Szilard, J., 1982, "Ultrasonic testing: Non-conventional testing techniques," JOHN WILEY & SONS, INC., 605 THIRD AVE., NEW YORK, NY 10158, 1982, 640.

[142] Lowet, G., and Van der Perre, G., 1996, "Ultrasound velocity measurement in long bones: measurement method and simulation of ultrasound wave propagation," Journal of biomechanics, 29(10), pp. 1255-1262.

[143] Mathieu, V., Anagnostou, F., Soffer, E., and Haiat, G., 2011, "Numerical simulation of ultrasonic wave propagation for the evaluation of dental implant biomechanical stability," The Journal of the Acoustical Society of America, 129(6), pp. 4062-4072.

[144] Sears, F. M., and Bonner, B. P., 1981, "Ultrasonic attenuation measurement by spectral ratios utilizing signal processing techniques," Geoscience and Remote Sensing, IEEE Transactions on(2), pp. 95-99.

[145] Virieux, J., 1986, "P-SV wave propagation in heterogeneous media: Velocity-stress finite-difference method," Geophysics, 51(4), pp. 889-901.

[146] Kampanis, N. A., Dougalis, V., and Ekaterinaris, J. A., 2008, Effective computational methods for wave propagation, CRC Press.

[147] Bossy, E., and Grimal, Q., 2011, "Numerical methods for ultrasonic bone characterization," Bone Quantitative Ultrasound, Springer, pp. 181-228.

[148] Fellinger, P., Marklein, R., Langenberg, K., and Klaholz, S., 1995, "Numerical modeling of elastic wave propagation and scattering with EFIT—elastodynamic finite integration technique," Wave motion, 21(1), pp. 47-66.

[149] Haïat, G., Naili, S., Grimal, Q., Talmant, M., Desceliers, C., and Soize, C., 2009, "Influence of a gradient of material properties on ultrasonic wave propagation in cortical bone: Application to axial transmission," The Journal of the Acoustical Society of America, 125(6), pp. 4043-4052.

[150] Protopappas, V. C., Kourtis, I. C., Kourtis, L. C., Malizos, K. N., Massalas, C. V., and Fotiadis, D. I., 2007, "Three-dimensional finite element modeling of guided ultrasound wave propagation in intact and healing long bones," The Journal of the Acoustical Society of America, 121(6), pp. 3907-3921.

[151] Gopalakrishnan, S., Chakraborty, A., and Mahapatra, D. R., 2007, Spectral finite element method: wave propagation, diagnostics and control in anisotropic and inhomogeneous structures, Springer.

[152] Bossy, E., Laugier, P., Peyrin, F., and Padilla, F., 2007, "Attenuation in trabecular bone: A comparison between numerical simulation and experimental results in human femur," The Journal of the Acoustical Society of America, 122(4), pp. 2469-2475.

[153] LECKEY, C. A., MILLER, C. A., and Hinders, M. K., 2011, "3D Ultrasonic Wave Simulations for Structural Health Monitoring."

[154] Guz, I. A., and Rushchitsky, J., 2007, "Computational simulation of harmonic wave propagation in fibrous micro-and nanocomposites," Composites science and technology, 67(5), pp. 861-866.

[155] Maio, L., Memmolo, V., Ricci, F., Boffa, N., Monaco, E., and Pecora, R., 2015, "Ultrasonic wave propagation in composite laminates by numerical simulation," Composite Structures,

121, pp. 64-74.

[156] Yang, Y., Lan, J., and Li, X., 2004, "Study on bulk aluminum matrix nano-composite fabricated by ultrasonic dispersion of nano-sized SiC particles in molten aluminum alloy," Materials Science and Engineering: A, 380(1), pp. 378-383.

[157] Nave, M., Dahle, A., and St John, D., "The role of zinc in the eutectic solidification of magnesium-aluminium-zinc alloys," Proc. Magnesium Technology 2000, The Minerals, Metals & Materials Society, pp. 243-250.

[158] Ghosh, S., Nowak, Z., and Lee, K., 1997, "Quantitative characterization and modeling of composite microstructures by Voronoi cells," Acta Materialia, 45(6), pp. 2215-2234.

[159] Fan, Z., Wu, Y., Zhao, X., and Lu, Y., 2004, "Simulation of polycrystalline structure with Voronoi diagram in Laguerre geometry based on random closed packing of spheres," Computational materials science, 29(3), pp. 301-308.

[160] Du, Q., Faber, V., and Gunzburger, M., 1999, "Centroidal Voronoi tessellations: applications and algorithms," SIAM review, 41(4), pp. 637-676.

[161] Suzudo, T., and Kaburaki, H., 2009, "An evolutional approach to the numerical construction of polycrystalline structures using the Voronoi tessellation," Physics Letters A, 373(48), pp. 4484-4488.

[162] Krautkrämer, J., and Krautkrämer, H., 1983, Ultrasonic testing of materials, springer.

[163] Chassignole, B., El Guerjouma, R., Ploix, M.-A., and Fouquet, T., 2010, "Ultrasonic and structural characterization of anisotropic austenitic stainless steel welds: Towards a higher reliability in ultrasonic non-destructive testing," NDT & E International, 43(4), pp. 273-282.

[164] CHINTA, P. K., and KLEINERT, W., "Elastic Wave Modeling in Complex Geometries using Elastodynamic Finite Integration Technique."

[165] Villagomez, C., Medina, L., and Pereira, W., "Open source acoustic wave solver of elastodynamic equations for heterogeneous isotropic media," Proc. Ultrasonics Symposium (IUS), 2012 IEEE International, IEEE, pp. 1521-1524.

[166] Zheng, R., Le, L. H., Sacchi, M. D., Ta, D., and Lou, E., 2007, "Spectral ratio method to estimate broadband ultrasound attenuation of cortical bones in vitro using multiple reflections," Physics in medicine and biology, 52(19), p. 5855.

[167] Gałecki, A., and Burzykowski, T., 2013, Linear mixed-effects models using R: A step-by-step approach, Springer.

[168] Pinheiro, J. C., and Bates, D. M., 2000, Mixed-effects models in S and S-PLUS, Springer Science & Business Media.

[169] Anderson, T. W., 2003, "An introduction to multivariate statistical analysis."

[170] Good, P., 2000, Permutation tests, Springer.

[171] Benjamini, Y., and Hochberg, Y., 1995, "Controlling the false discovery rate: a practical and

powerful approach to multiple testing," Journal of the Royal Statistical Society. Series B (Methodological), pp. 289-300.

[172] Virieux, J., 1984, "SH-wave propagation in heterogeneous media: velocity-stress finite-difference method," Geophysics, 49(11), pp. 1933-1942.

[173] Grin, Yuri, et al. "CuAl 2 revisited: Composition, crystal structure, chemical bonding, compressibility and Raman spectroscopy." Journal of Solid State Chemistry 179.6 (2006): 1707-1719.

[174] Zhou, Wei, et al. "Structural, Elastic, and Electronic Properties of Al-Cu Intermetallic from First-Principles Calculations." Journal of electronic materials 38.2 (2009): 356-364.

[175] Wang, Ying, and Hong Hao. "Damage identification scheme based on compressive sensing." Journal of Computing in Civil Engineering 29.2 (2013): 04014037.

[176] Cha, P. D., and W. Gu. "Model updating using an incomplete set of experimental modes." Journal of sound and vibration 233.4 (2000): 583-596.

[177] Penny, J. E. T., M. I. Friswell, and Noel Gerald Nalitolela. "A mass or stiffness addition technique for structural parameter updating." (1992).

[178] Jiang, L. J., J. Tang, and K. W. Wang. "An enhanced frequency-shift-based damage identification method using tunable piezoelectric transducer circuitry." Smart Materials and Structures 15.3 (2006): 799.

[179] Bao, Zhongping, et al. "The role of beam flexibility and ground contact model in the clattering of deformable beams." TRANSACTIONS-AMERICAN SOCIETY OF MECHANICAL ENGINEERS JOURNAL OF DYNAMIC SYSTEMS MEASUREMENT AND CONTROL 126.2 (2004): 421-425.

[180] Jiang, L. J., J. Tang, and K. W. Wang. "On the tuning of variable piezoelectric transducer circuitry network for structural damage identification." Journal of Sound and Vibration 309.3 (2008): 695-717.

[181] Wong, C. N., W. D. Zhu, and G. Y. Xu. "On an iterative general-order perturbation method for multiple structural damage detection." Journal of Sound and Vibration 273.1 (2004): 363-386.

[182] Q Shuai, K Zhou, S Zhou and J Tang. " Fault identification using piezoelectric impedance measurement and model-based intelligent inference with pre-screening." Smart Materials and Structures, Volume 26, Number 4, 2017

[183] Adams, R. D., et al. "A vibration technique for non-destructively assessing the integrity of structures." Journal of Mechanical Engineering Science 20.2 (1978): 93-100.

[184] Padil, Khairul H., Norhisham Bakhary, and Hong Hao. "The use of a non-probabilistic artificial neural network to consider uncertainties in vibration-based-damage detection." Mechanical Systems and Signal Processing 83 (2017): 194-209.

[185] Jinji, Sun, Bai Guochang, and Yang Lei. "Stiffness measurement of permanent magnet biased radial magnetic bearing in MSFW." Journal of Dynamic Systems, Measurement, and Control 137.9 (2015): 094505.

[186] Koh, Kwangmoo, Seung-Jean Kim, and Stephen Boyd. "An interior-point method for large-scale l1-regularized logistic regression." Journal of Machine learning research 8.Jul (2007): 1519-1555.

[187] Sprent, P. "A generalized least-squares approach to linear functional relationships." Journal of the Royal Statistical Society. Series B (Methodological) (1966): 278-297.

[188] Tibshirani, Ryan J. "The lasso problem and uniqueness." Electronic Journal of Statistics 7 (2013): 1456-1490.
[189] Candes, Emmanuel J., Michael B. Wakin, and Stephen P. Boyd. "Enhancing sparsity by reweighted ℓ 1 minimization." Journal of Fourier analysis and applications 14.5 (2008): 877-905.
[190] Kariya, Takeaki, and Hiroshi Kurata. Generalized least squares. John Wiley & Sons, 2004.
[191] Westfall, Peter H., and S. Stanley Young. Resampling-based multiple testing: Examples and methods for p-value adjustment. Vol. 279. John Wiley & Sons, 1993.
[192] Mei, T. X., and H. Li. "Control design for the active stabilization of rail wheelsets." Journal of Dynamic Systems, Measurement, and Control 130.1 (2008): 011002.
[193] Melbourne, Clive, ed. Arch Bridges: Proceedings of the First International Conference on Arch Bridges, Held at Bolton, UK on 3-6 September 1995. Thomas Telford, 1995.